PULSED BREAKDOWN PHENOMENA IN PARTIAL VACUUM

by

Zhenhong Li

A thesis submitted to the Graduate Faculty of
Auburn University
in partial fulfillment of the
requirements for the Degree of
Master of Science

Auburn, Alabama
December 8, 2012

Approved by

Hulya Kirkici, Chair, Professor of Electrical and Computer Engineering
Thaddeus Roppel, Associate Professor of Electrical and Computer Engineering
Michael Baginski, Associate Professor of Electrical and Computer Engineering

Abstract

In this thesis, the pulse generation and pulsed breakdown phenomena have been studied in detail. Pulsed power is widely used in food processing, biotechnology, military defense, and industrial applications. The first part of this work covers the simulation and analysis of common high voltage DC and pulse generator circuits. Then high power switching techniques which are essential to the generation of pulsed power are also explored. Due to the rapid development of high energy laser and accelerator, high power switches capable of handling powers up to terawatts are in great demand in industry. Pseudospark switch using the hollow cathode effect is an example for these applications. Pseudospark discharge is triggered by many means and is challenging. Carbon Nanotubes (CNTs) triggering is achieved in pseudospark switches operated in helium and tested in the laboratory. The delay time of the triggered breakdown with several CNTs samples under different trigger voltages is summarized.

As the second part of this research, the pulsed breakdown phenomena in partial vacuum are investigated thoroughly. Solid insulators are widely employed in power systems operating in atmospheric pressure and partial vacuum. However, the hold-off capability of an insulator in vacuum is limited by the surface flashover problem due to the cathode 'triple-junction' effect. This is a common problem for space power and aerospace power systems. In this work, the surface flashover characteristics of nanodielectric materials composed of cast epoxy resin mixed with nano-dielectric particles in partial vacuum are studied. The samples except the control samples are made by adding nanoscale Al_2O_3 or TiO_2 powder with predetermined ratios into the

epoxy resin with known properties. The samples are cylindrical in shape (2.5 cm in diameter and 1 cm in thickness) and varying electrode configurations and spacing are used in this study. The surface flashover characteristics of the samples are investigated using both DC and 20 kHz pulsed-unipolar signals separately. The frequency and duty cycle of the pulsed signal are also varied in the experiments in order to obtain a clearer understanding of pulsed surface flashover in partial vacuum. Initially the cylindrical samples are sandwiched between two parallel plate electrodes, and the voltage, current, and light emission waveforms during the flashover events are recorded and analyzed. As a second test set, the electrodes laterally placed on the samples' flat surface and surface breakdown experiments conducted and comparisons to the parallel plate case are made.

Acknowledgments

The author would like to thank his advisor Dr. Hulya Kirkici for her patience and guidance on this research work during the past two years. Without her support this work would be impossible to achieve. The author would like to thank Dr. Baginski and Dr. Roppel for serving as the committee members. The author also would like to express appreciation to Ms. Linda Barresi and Mr. Calvin Cutshaw for their material assistance during this work. Thanks are also due to his group members, especially Rujun Bai, Haitao Zhao and Huirong Li who help him run the experiments over and over again. Finally, the author wishes to thank his mother and sisters, for their unfailing support and understanding.

[ξ] Work partially sponsored by AFOSR grant # AF-FA9550-08-10051

Style manual or journal used Graduate School's Thesis and Dissertation Guide

Computer software used Microsoft Office 2007

Table of Contents

List of Tables

List of Figures

CHAPTER I

INTRODUCTION & BACKGROUND

1.1 Introduction

Pulsed power technology is widely employed in biotechnology, food processing and preservation, military defense, and other industrial applications [1-5]. Pulsed power is a scheme where energy is stored for a long time, and then discharged into a load as electrical energy in a single short pulse or as short pulses with a controllable repetition rate [6]. Generally the pulsed power generation system consists of high voltage power supply, energy storage component, pulse compression stages, impedance matching network, switches, and discharge load [4]. Pulsed power generators are classified as either inductive or capacitive where energy is stored respectively. Although lacking of stored energy density, high voltage energy storage capacitors are still used in most pulsed power systems, because it is much easier to build reliable system, and can be made repetitive. Power switches are essential to the pulsed power generation system. Also fast closing switches for capacitive storage systems are more developed than the counter partners of opening switches for induction storage systems [6]. Gas switches and solid-state switches are two types of commonly used closing switches. Because of the compactness, light weight, high operation speed, low cost, and high frequency, in recent years semiconductor switches are extensively used to generate high voltage pulses [5]. However, their performance on power capability is usually limited because of the relatively low mobility and density of

charge carriers and low operating temperature [6]. Conventional gas switches such as spark gap, vacuum gap, and pseudospark switch are more powerful and can handle very large currents and charges. Pseudospark switch taking advantage of the hollow cathode effect stands out because of its high power capability, less electrode erosion, and higher lifetime. In this thesis, as a preliminary study of pseudospark switch, the helium hollow cathode discharge initiated by carbon nanotubes (CNTs) cold cathodes is tested in the lab. With the properties of low turn-on voltage and excellent field emission, CNTs are promising cold cathode emitters as innovative trigger methods for pseudospark switches. In this work, a pulse generator used as the power source to trigger CNTs cold cathode as trigger electrode is also analyzed, simulated, and built.

In the second part of this thesis, the pulsed breakdown phenomena of nanodielectrics are investigated. The insulation of space power system has been a serious issue since the beginning of the space exploration program. Continual advances in space systems have increased the demand for higher power requirements and the operation voltage has changed from traditional 28 V standards to much higher levels. For the International Space Station requiring 100 kW level electric power, operation voltage at 160 V is used. But for the solar power satellite (SPS), in which gigawatt power is generated by large solar arrays, it is typically operated at 1000 V in the power generation and transmission system [7]. However, this adds severe weight constraint on space power systems. It has been shown that two methods can be employed to fulfill the critical demand on weight reduction [8-9]. One method is to operate the magnetic circuitry at much higher frequencies; the other is to use more compact components. Thus the working frequency of modern high voltage switching mode power supplies in space system is increased from low frequency range of 60 Hz ~ 400 Hz to radio frequency range of 100 kHz ~ 1 MHz or even higher [7]. More compact systems means, spacing between the differently biased components is

drastically reduced. Thus stringent electrical insulation of these components and sub-systems are required. Meanwhile, in order to satisfy the increasing power demand in spacecraft, power generation at higher voltage and lower current is a commonly employed method from the point of view of reducing power loss in the transmission lines [10]. However, the reduced spacing between the components (effective electrode gap), the operation at higher frequency than traditional 400 Hz, and higher voltage than 28 V in space power systems increase the stress on electrical insulation. It has been shown that many compact designs have failed because of insulation design overstress, incompatible coordination, and improper insulation testing during and following final packaging [7].

Partial discharges and coronas enhanced by high frequency and high voltage is more likely to occur in these systems, resulting in power loss and leading to degradation, aging or thermal breakdown of the insulation and components. They also generate undesirable noise as electromagnetic interference (EMI) which can disturb the signal transmitted in the space power systems. As in the case of ground based systems, insulation already experienced short circuiting, power losses, and spurious signals in communication systems and sensitive sensors [11] due to arcing discharge. In space and aerospace systems, other environmental factors such as electrical degradation and decrease in breakdown strength are due to molecular particulate contaminants [12]. Consequently studies on electrical breakdown of dielectrics in space environment are still meaningful.

Although significant work has been made on gas breakdown in partial vacuum [13-14], most of the data on maintenance and protection in literature only deals with ground based power systems operating at 50/60 Hz at atmospheric pressure. Furthermore, there are only a few reports available on high frequency breakdown in partial vacuum [13], and breakdown

characteristics of dielectrics in partial vacuum under kHz range pulses still need more investigation.

Nanodielectrics are a group of filled-polymers where sub-micrometer or nanometer sized ceramic or metal-oxide insulating particles are added to polymeric dielectric materials. They are widely used in the photonics and electronics areas currently and are also promising materials in electrical insulation (high power density and high voltage) [15]. In general, the hold-off capability of an insulator in vacuum is limited by the surface flashover problem due to the cathode 'triple-junction' effect [16]. This is also true for nanodielectrics. This thesis focuses on the study of nanodielectrics surface flashover under DC and kHz range pulses in partial vacuum.

1.2 Electrical Breakdown of Gases

Air is commonly used as insulating medium in electrical installation because of its abundance and excellent self-restoring capability after breakdown. On the other hand, solids and liquids usually contain gas voids and contamination leading more frequent breakdown and partial discharges. Therefore the gaseous breakdown research is significant for designers and operators who are working on electrical and electronic equipment insulation.

1.2.1 Townsend Mechanism

A simple gas breakdown test system is illustrated in Figure 1.1. It consists of a pair of parallel plates enclosed in a gas chamber and separated by a distance *d*. The electric field between the electrodes is assumed to be uniformly distributed when a high voltage is applied between the electrodes. When electrons are emitted from the cathode by any means, they are accelerated toward the anode under the strong applied electric field. If the electrons acquire

enough energy, they can ionize the gas molecules through collisions. The generated new electrons propagate along the field as the primary ones, and then ionize other gas molecules. The primary avalanche ends after the ions enter the cathode region. If the amplification and electron avalanche is increased, more electrons are liberated in the gap by secondary ionization from positive ions, excited atoms, photons, and metastables. These secondary electrons initiate new avalanches, resulting in a space charge formation in the gap. The space charge formation enhances the electric field somewhere between the electrodes, with a subsequent fast current increase, leading to the breakdown of the gas ultimately. This is the classical Townsend mechanism.

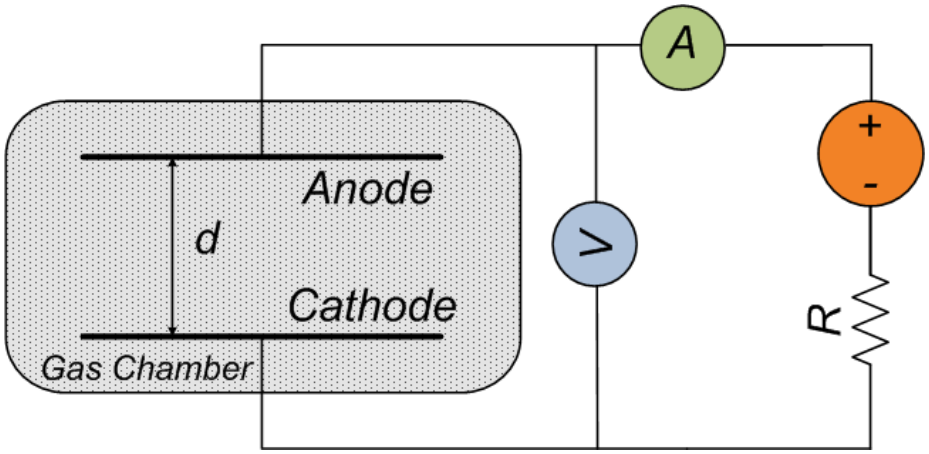

Figure 1.1 Schematic of simple gas breakdown test

The relationship between the current and applied voltage was explained by Townsend as shown in Figure 1.2 [18]. He determined that the current at first increases proportionally as the voltage increases, and then reaches a saturation current I_0 and remains steady for a while. The current I_0 results through photoelectric effect produced at the cathode by external irradiation. If the voltage is increased further, current increases exponentially. This reveals the eventual spark breakdown of the gap.

In the steady state, the circuit current is given by

$$I = \frac{I_0 e^{\alpha d}}{1-\gamma(e^{\alpha d}-1)} \qquad (1.1)$$

where α is Townsend first ionization coefficient, γ is Townsend secondary ionization coefficient, d is distance between electrodes, I_0 is saturation current, I is current flowing in the circuit.

Neglecting the power supply internal resistance, the current becomes infinite if

$$\gamma(e^{\alpha d} - 1) = 1 \qquad (1.2)$$

Normally, $e^{\alpha d} >> 1$, and Equation 1.2 is simply expressed as

$$\gamma e^{\alpha d} = 1 \qquad (1.3)$$

Equation 1.2 defines the onset condition of spark and is known as the Townsend criterion for spark breakdown.

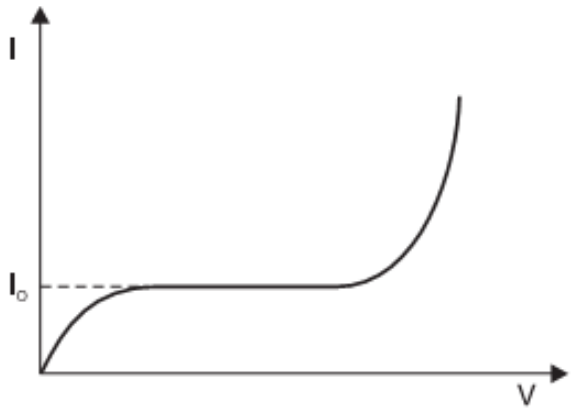

Figure 1.2 Variation of current as a function of applied voltage [12]

1.2.2 Paschen's Law

Paschen's law is a fundamental but most important principle in gas breakdown phenomena. It describes the relationship between the breakdown voltage V and the product of pressure p and electrode distance d in a gaseous environment. By investigating the ionization

process by electron impact, we can determine the coefficients of α and γ both functions of the gas pressure and the electric field. Namely, $\alpha = p * F_1(\frac{E}{p})$ and $\gamma = p * F_2(\frac{E}{p})$. Since $E = \frac{V}{d}$ for parallel plate electrodes, Equation 1.2 can be revised as

$$F_2\left(\frac{V}{p*d}\right)\left[e^{p*dF_1\left(\frac{V}{p*d}\right)} - 1\right] = 1 \qquad (1.4)$$

or $V = F(pd)$.

This is the well-known Paschen's law [19]. The experimental data of Paschen curves for different gases under uniform dc field are shown in Figure 1.3 [20]. The 'V' shape Paschen curve has a minimum breakdown voltage at a specific product of *pd*. If we assume the electrode spacing *d* is fixed, then there are two regions namely high pressure and low pressure in this plot. As the pressure reduces from atmospheric pressure on the right-hand side to the paschen minimum, the electron free path increases as the gas density decreases. Therefore, when the electrons travel toward the anode, they have fewer collisions with the gas molecules and gain more energy from the electric field with less collision loss. Thus a lower electric field is strong enough to provide electrons with sufficient energy for ionization collision and electrons are accelerated further leading breakdown at lower voltage. When the minimum point of the curve is reached, the density is even lower and fewer collisions occur. If the pressure is further lowered, then the breakdown takes place at a higher level. This region is called the left-hand side of Paschen curve, and electron mean free path is relatively large with less density of background gas. Because there are a few molecules, fewer collisions take place, and this is the reason for higher breakdown voltage.

Empirical formula has been proposed to calculate the dc breakdown voltage of uniform-field gaps at atmospheric pressure air as following:

$$V = 2440d + 61\sqrt{d} \text{ kV} \qquad (1.5)$$

where *d* is the gap length in meters. However, for the space power systems, this may not be used because of the operation in low pressure. Also traditionally space power systems operate at low frequency AC, however, recently they have operated at kHz frequency. The breakdown curves in this case are still similar to the Paschen curve as shown in Figure 1.4 [21] and Figure 1.5 [22].

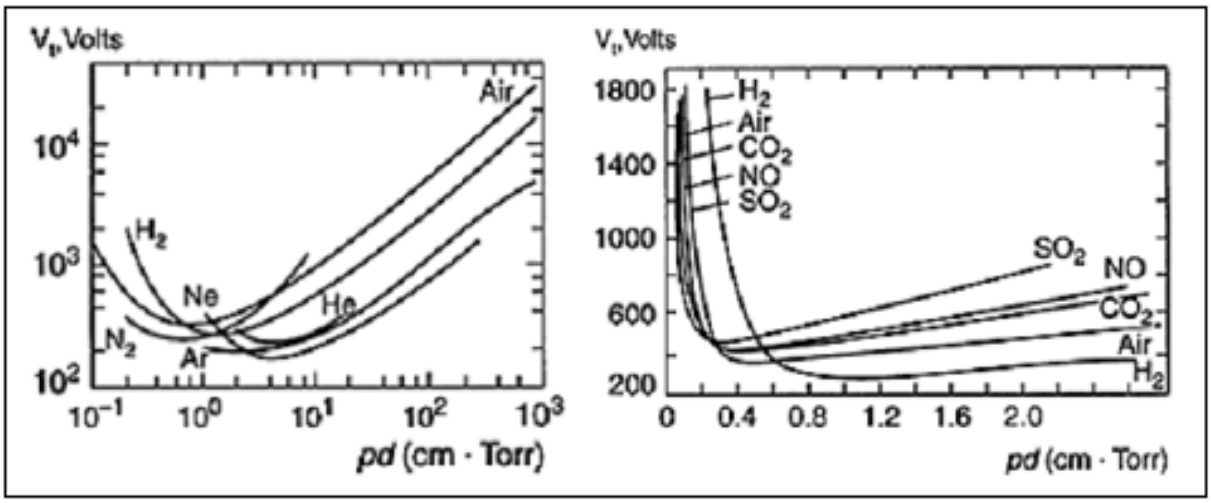

Figure 1.3 Paschen curves for different gases under DC [20]

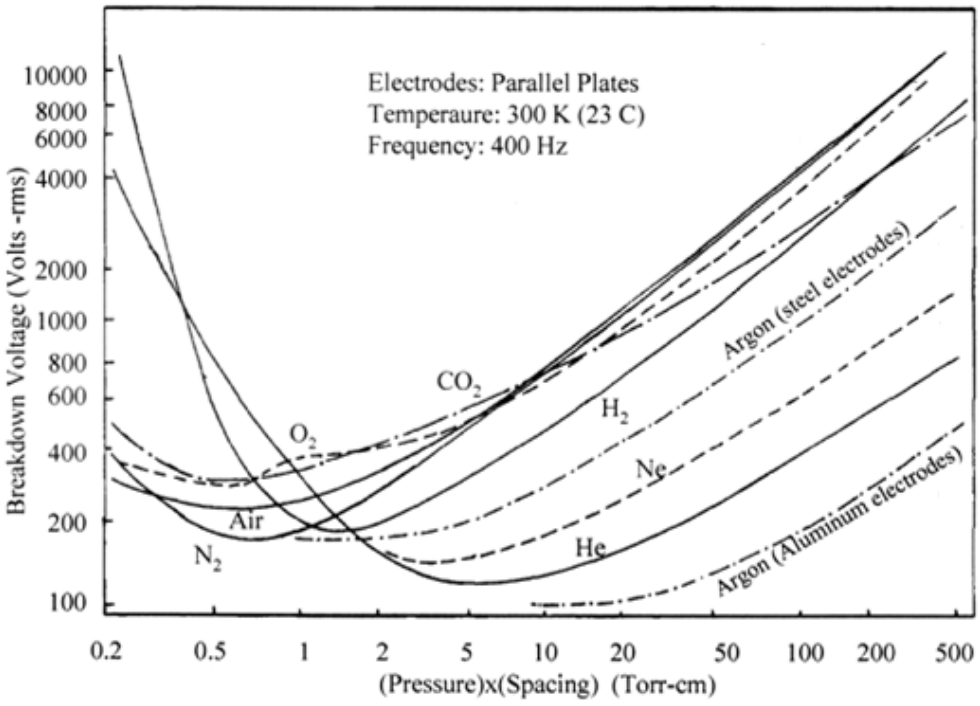

Figure 1.4 Paschen curves for various gases under 400 Hz AC [21]

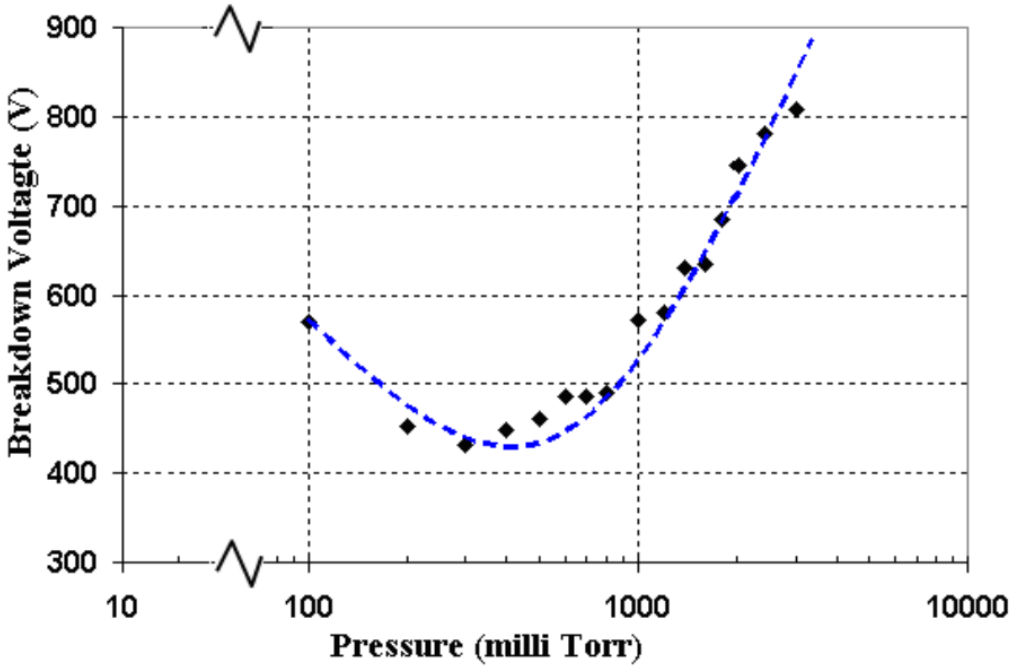

Figure 1.5 Paschen curves for various gases under 20 kHz unipolar sinusoid signal [22]

1.2.3 High Frequency Breakdown

In uniform-field gaps, electrical breakdown starts with the avalanche process as described above for DC and low-frequency AC cases. If the frequency of the applied field is increased to kHz and beyond, the discharge behavior begins to change. For a given electrodes spacing *d*, there is a critical frequency f_c at which positive ions can just be cleared from the gap during one half-cycle of the AC applied voltage,

$$f_c = \frac{k_+}{\pi d^2} V \qquad (1.6)$$

where k_+ is the mobility of positive ions and *V* is the applied voltage.

If the applied AC frequency is smaller than f_c, the breakdown conditions are similar to those of static fields. If the AC frequency is larger than f_c, the cloud of positive ions will oscillate between the electrodes. As the continuous generation of new avalanches, the density and size of the positive cloud will keep increasing until stability and breakdown occur. The

electric field distribution in the gap is distorted by the accumulating positive space charges, leading to the AC breakdown with voltages lower than that under DC case. The high frequency voltage breakdown behavior is illustrated in Figure 1.5 [19].

Likewise, there is a critical frequency f_{ce} above which electrons cannot reach the opposite electrode in one half-cycle,

$$f_{ce} = \frac{k_e}{\pi d^2} V \qquad (1.7)$$

where k_e is the mobility of electrons and V is the applied voltage.

If the applied AC frequency is between f_c and f_{ce}, the oscillating positive ion space charges in the gap still dominate the electrical breakdown behavior. At even higher frequencies, electrons in the gap begin to oscillate between the electrodes. If some of them cannot reach the anode during one half-cycle, they will neutralize the positive-ion space charges, reduce the distortion of electric field in the gap, and lead to higher breakdown voltages ultimately. If the AC frequency keeps increasing to a certain frequency f_{co} at which the breakdown mechanism is controlled by diffusion, the electrodes will not play any role and make any contribution to the ionization process. The breakdown voltage under this condition usually drops sharply since the breakdown is mainly controlled by diffusion.

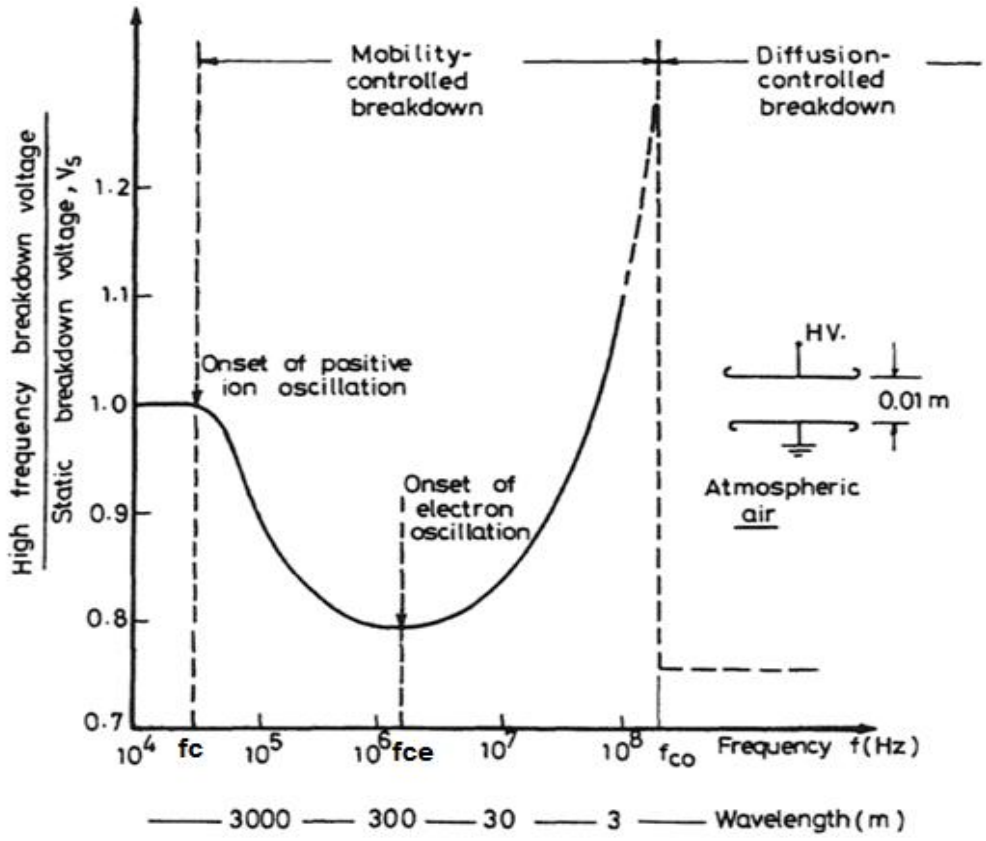

Figure 1.6 Ratio of high-frequency breakdown voltage to static breakdown voltage as a function of frequency for a uniform air gap [19]

1.2.4 Pulsed Breakdown

Pulsed breakdown is another consideration in electrical and electronic equipment insulation design. In power systems and electrical components, impulse overvoltages leading to breakdowns are frequently imposed due to lightning and switching surges. Under pulsed applied fields, a time lag is observed between the moment the voltage is applied and the breakdown occurs. In detail, the time lags involved in the pulsed breakdown process are shown in Figure 1.6. The symbols in this figure are described as:

t_0 — the time until the applied voltage exceeds the static breakdown voltage U_b;

t_s — the statistical delay time until a seed electron able to create an avalanche occurs;

t_a — the avalanche build-up time until the critical charge density is reached;

t_{arc} — the time required to establish a low resistance arc across the gap.

The statistical delay time t_s results from the statistics of electron appearance in the gap. Not every electron emitted into the gap is able to initiate an avalanche even though the applied voltage is higher than the static breakdown value. Nevertheless, after the first seed electron avalanche is initiated, pulsed breakdown is well developed in two different ways, namely, Townsend breakdown and streamer mechanism [6]. In the Townsend breakdown mechanism, several generations of avalanches can be developed till a glow-to-spark transition or a quasi-stable glow discharge occurs. During the streamer breakdown, a single avalanche is strong enough to produce a critical number of electrons before the anode is reached. Electrons that escape from the avalanche head can cause a field distortion, which drives the self-propagation of the avalanche ultimately. Therefore, the build-up time t_a is very different for these two cases.

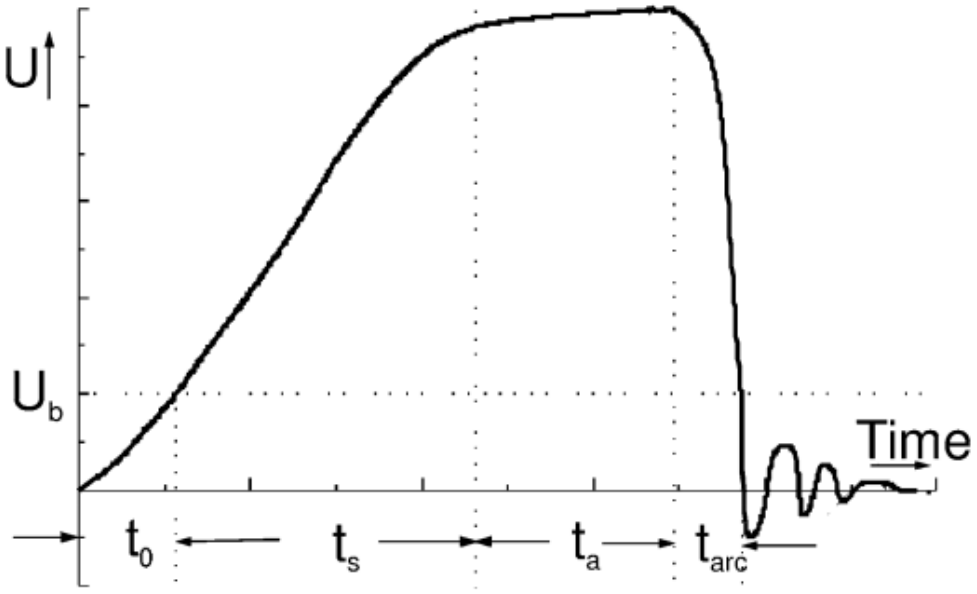

Figure 1.7 Time lags determining the dynamics of breakdown in a gas-insulated gap [6]

1.2.5 Glow Discharge

Glow discharge is a kind of luminous low pressure discharge which has widespread industrial applications such as analytical chemistry, micro-electronics fabrication, and lasers [23]. Glow discharge is the self-sustained continuous DC discharge consisting of a cold cathode, which emits electrons as a result of secondary emission mostly induced by positive ions [20]. Figure 1.7 is the schematic of typical normal glow discharge. Immediately next to the cathode is a dark layer known as the Aston dark space and then a relatively thin layer of the cathode glow. It is a bright region close to the cathode with high ion number density. Adjacent to cathode glow zone is the cathode dark space followed by the negative glow which is the brightest region with intense excitation and ionization of atoms. Electrons accelerated in the cathode region collide with the background gas and cause light emitting processes. The negative glow gradually decreases in brightness toward the anode, becoming the Faraday dark space. The positive column emerging after that is uniform, bright (though not as bright as the negative glow), and relatively long if the length of the discharge tube is sufficiently large. At constant pressure, if the length of the discharge tube is increased, the positive column will lengthen while the cathode region will remain constant. In the area of the anode layer, the positive column is evolved first into the anode dark space and then into the narrow anode glow zone and finally the anode dark space area. A special feature of a glow discharge is the cathode layer with dense positive space charges and the strong electric field with a large voltage drop almost equal to the applied voltage level.

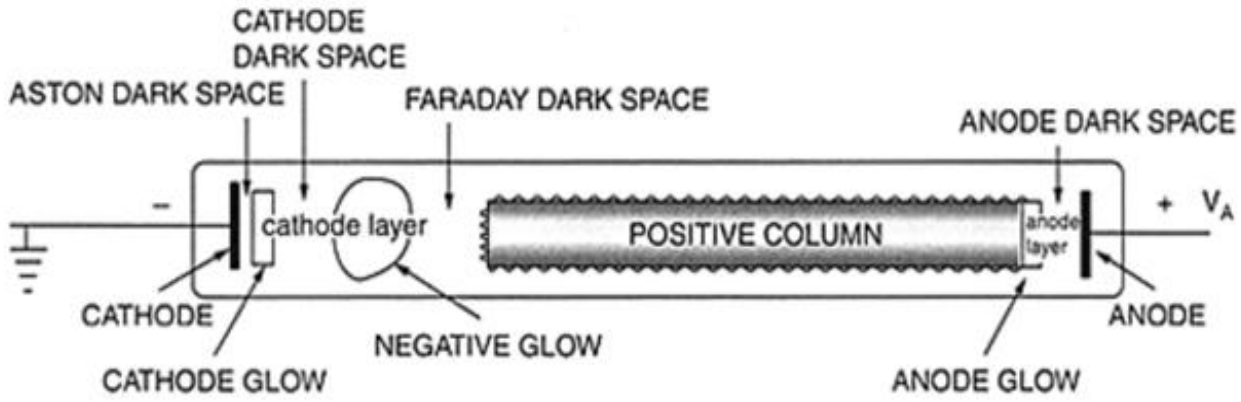

Figure 1.8 General structure of a glow discharge [20]

1.2.6 Hollow Cathode Discharge

If a single planar cathode in glow discharge is replaced by a cathode with hollow structure, the current will be orders of magnitude larger than that in the plannar structures. The negative glow region of the discharge moves into the hollow structure of the cathode, leading to higher ionization and excitation processes. This effect is called the hollow cathode effect which is mainly caused by pendulum electrons [24-25]. Electrons emitted from the internal hollow cathode surface are found to be reflected on the opposite cathode surface when they go through the negative glow without significant energy loss. These reflected electrons regarded as pendulum electrons and they greatly increase the ionization collisions in the hollow cathode. Because of the larger weight of positive ions compared to the electrons, the cloud of ions remains in the cathode cavity after collisions and form a virtual anode. The electric field in the cathode is enhanced by this virtual anode and more electrons are emitted which further strengthen the ionization collisions with the background gas and contribute to the increase of the positive ion density. The cathode fall, referred as the distance between the virtual anode and the cathode sheaths, can be significantly thinner in hollow cathode configurations, resulting in an

extremely high electric field and the succeeding higher secondary electrons emission rate. In this way, the hollow cathode structure increases the probabilities of multiple processes and collisions for all particles and is able to generate very high density plasma inside the hollow cathode.

In general, the hollow cathode discharge range for rare gases is given as 1 torr·cm < pD < 10 torr·cm, where p is pressure and D is the diameter of the hollow cavity [26]. Due to this pD restriction, most of the hollow cathode discharge devices are operated at low pressure and on the left-hand side of the well-known Paschen curve.

1.3 PULSED POWER

Pulsed power engineering is the technology of storing energy in capacitive or inductive form over a relatively long period of time (usually seconds to minutes) and then discharging it into a load over a much shorter time period (usually nanoseconds to microseconds) as electrical energy by closing or opening power switches. Power generation, power switches, pulse forming network, and the load are the major components of a pulsed power system.

1.3.1 Pulsed Power Generation

Many types of high voltage and nanosecond pulse generators are commercially available currently. However, the performance of these generators varies broadly and they should be chosen according to load requirements, such as output voltage, pulse width, rise time, repetition rate, and peak power.

The fundamental purpose of all pulsed power system is to convert a low-power, long-time input into a high-power short-time output. A general pulsed power system diagram is shown as Figure 1.8 [4]. The high voltage power supply fed from wall power by full-wave

rectifiers is the power source to the pulsed power system. It determines the charging time of the energy storage section, which normally ranges from microseconds to minutes. The pulse energy is stored in the energy storage section for an amount of time which depends upon the output requirements. When the energy in the storage section is transferred into the first pulse compression or pulse forming stage, pulse compression section starts to run. The number of pulse compression stages can vary from one to many, which depends on the application. Each of these stages usually requires a switch. The impedance match section, for instance, a transformer or transmission line, is necessary to discharge the maximum power to load with the minimum reflections. The final section before the discharge load, the primary power switch, delivers all of the pulsed power into the load.

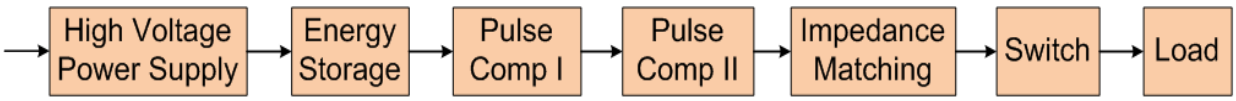

Figure 1.9 Pulsed power train diagram [4]

Generally all pulse generation circuits are classified as either capacitive or inductive storage. The simple capacitive storage discharge circuit and pulse forming line (PFL) are two elemental methods to generate short pulses. Other pulse generators such as Marx generator and Blumlein PFL are mostly adapted from them.

An *RC* circuit shown in Figure 1.9 can be easily used to generate double-exponential high voltage pulses by charging the capacitor C and then discharging its energy into the load by simply closing the switch S_1. Transmission line or PFL in Figure 1.10 is another good alternative to generate high voltage rectangular pulses. When the switch S_1 is closed at $t = t_0$, a

pulse of amplitude ($-V_0/2$) propagates down the line toward line length d. It then reflects at d and returns to the switch and the load at

$$t = t_0 + \frac{2d\sqrt{\varepsilon_r}}{c} \text{ (sec)} \qquad (1.8)$$

where ε_r is the relative permittivity of the transmission line, d is the length of the transmission line in meters, c is the speed of light.

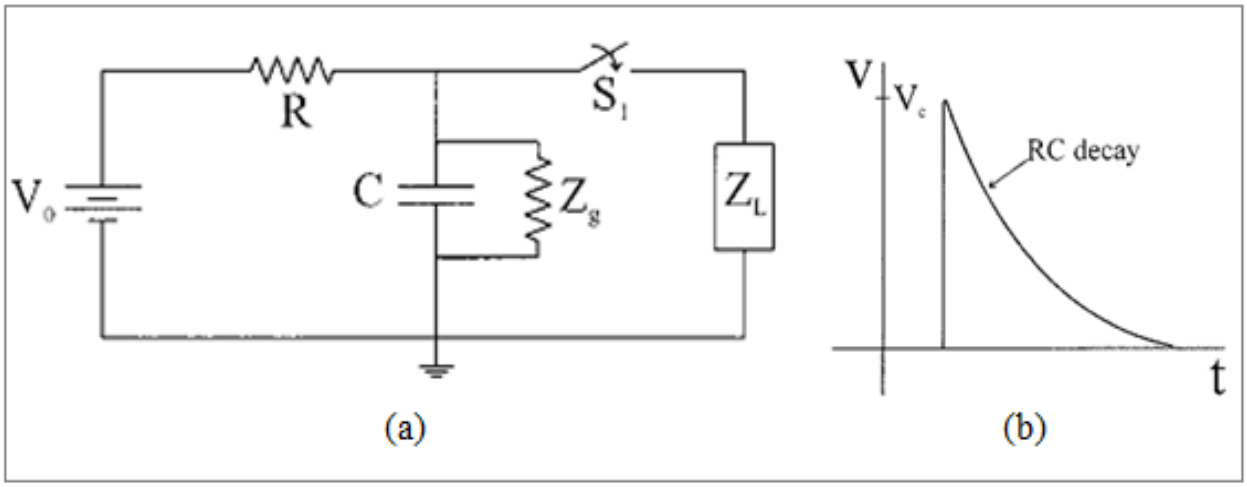

Figure 1.10 (a) Simple capacitive storage discharge circuit (b) output voltage with RC decay [4]

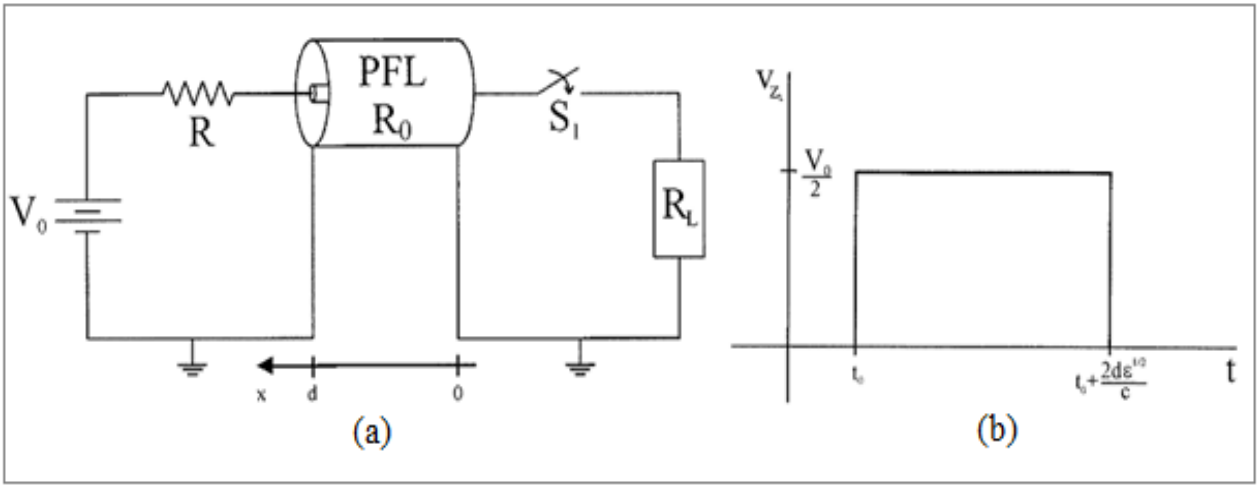

Figure 1.11 (a) PFL circuit (b) square output pulse voltage [4]

1.3.2 Power Switches

Power switches, between the storage devices and the loads, play an indispensable role in the generation of pulsed power. The shape, rise time, and magnitude of the generator output pulse depend strongly on the properties of the power switches. Moreover, the maximum power capacity and power density that the power switches could handle also limit the performance of pulse generators. Switches are generally categorized into closing switches for capacitive storage devices and opening switches for discharging inductive storage devices.

Gas switches and semiconductor switches are two common types of closing switches. Gas switches are highly employed in high power pulse generators. They are easy to use, can handle relatively large currents, and can be also triggered accurately. Several kinds of gas switches such as ignitron, krytron, thyratron, pseudospark switch, and spark gap are reported in literature [6]. Their operating gas pressure and hold-off voltage ranges are shown in Figure 1.11.

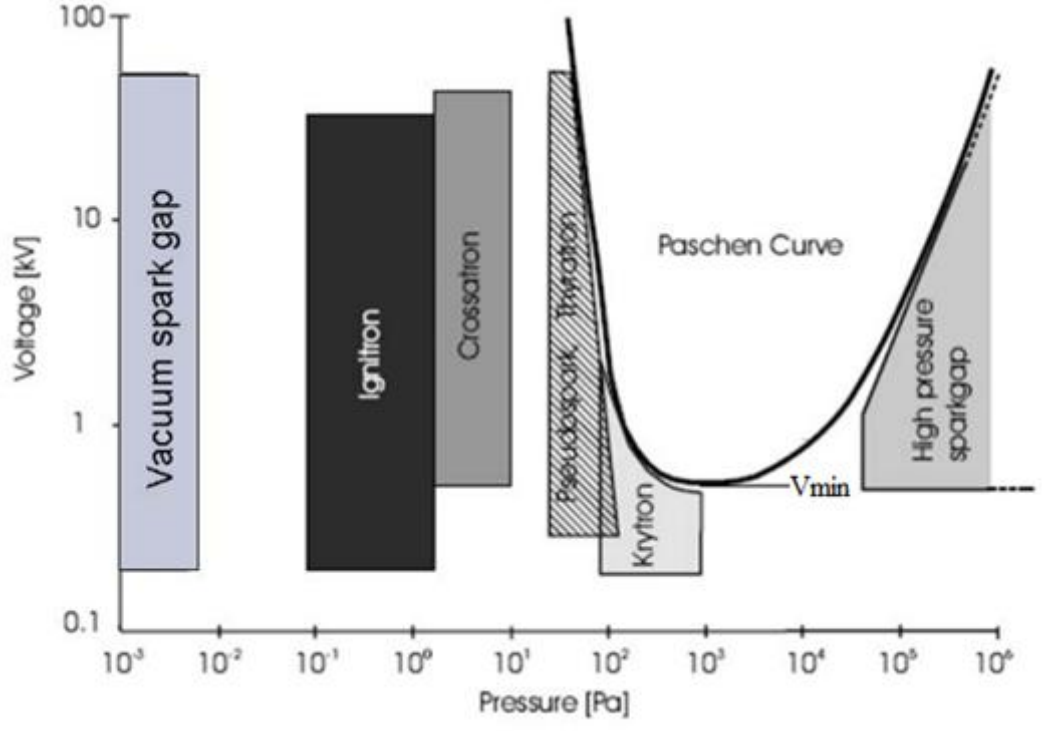

Figure 1.12 Range of gas pressure and operating voltages for different types of gas switches [6]

Among these, pseudospark switch taking advantage of hollow cathode effect, stands out because of its reduced electrode erosion, high power capability, and long lifetime. Figure 1.12 shows the typical schematic and electric field configuration in a two-electrode pseudospark switch. Generally the operation of pseudospark switch is described in four different periods: pre-discharge, hollow cathode discharge, high current super-emissive discharge, and the decay of the discharge plasma [27]. In order to make use of the pseudospark discharge, a precise triggering system is required for the switch. For reliable triggering, about 10^9 to 10^{10} electrons are needed inside the hollow cathode [28]. A lower number of electrons results in higher delay and jitter time values, or cannot initiate the discharge at all. Several triggering methods have been researched, such as surface flashover, low current glow discharge, optical triggering, and electrons injection. Each of the methods has its pros and cons [27] with regard to the lifetime, operating frequency, construction complexity, and delay time. As a preliminary study of pseudospark switch, the helium hollow cathode discharge initiated by carbon nanotubes (CNTs) cold cathode is tested [27]. With the properties of low turn-on voltage and excellent field emission, CNTs are highly potential to be employed as an innovative trigger method. In this thesis the pulse generator used to trigger CNTs is developed and constructed.

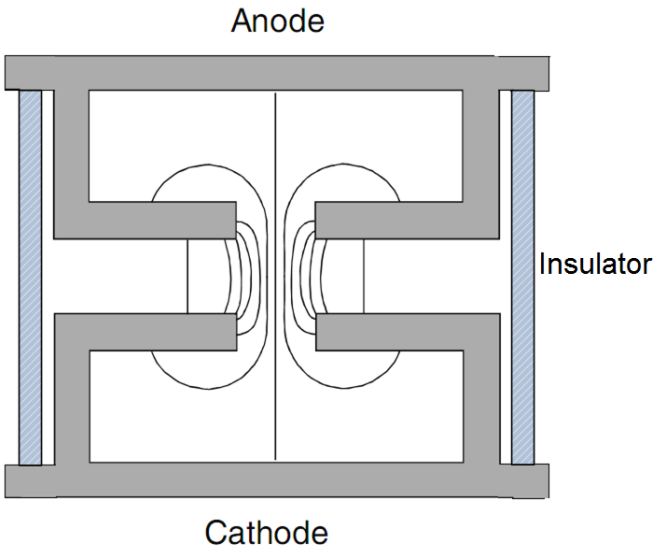

Figure 1.13 Typical schematic and electric field configuration in pseudospark system

1.4 SURFACE FLASHOVER

Surface flashover is a very common phenomenon in atmosphere pressure. When the insulator surface is wetted by fog or rain, the pollution layer becomes conductive and final flashover occurs after a serial of events such as conduction layer build-up, dry band formation, partial arcing, arc elongation, and eventual arc spanning the whole insulator [32]. In vacuum, the surface flashover is caused by another mechanism called 'triple-junction' effect [16], where the electrons are emitted from the cathode at the cathode-vacuum-insulator intersection where field is enhanced, and propagate along the insulator surface causing breakdown. However, for aerospace power system operating in partial vacuum environment, the surface flashover has not been fully explained and is expected to be similar to the one in the case of surface flashover in vacuum [33].

1.4.1 Space Environment & Spacecraft

Space is often mistakenly considered as a vast, empty vacuum. In reality, space is a dynamic place filled with energetic particles, radiation, and trillions of objects. Specifically, space environment is a low-pressure gas consisted of a small quantity of weakly ionized gas from solar interactions, abundant neutral atoms and molecules, and other charged particles as electrons [12].

Spacecraft orbiting in the space suffers from the radiation, space debris and meteoroid impact, and electrostatic charging. Space debris and meteoroids can cause serious mechanical or electrical damage to the spacecraft if they collide at very high speeds. The average speed of space debris is 10 km/s while the meteoroids move at even higher speeds. Tragedy occurred from the electrical malfunction related to this kind of collision. ESA's (European Space Agency) Olympus -1 satellite lost altitude control and was severely damaged during the 1993 Perseid meteor shower. Spacecraft also suffers from electrostatic differential charging by the hot plasma environment around the Earth. This high potential, resulted from the continuous accumulation of static charges, can be of the order of several kilovolts. If discharged improperly, this differential discharging may cause direct or indirect damages to semiconductor devices and electronic systems on the spacecraft.

Furthermore, the space environment is influenced by the presence of spacecraft also. The local pressure around the spacecraft is altered by a few orders of magnitude due to outgassing, gas leaks, or exhausts. Data from several early STS flights are presented in [17] with regard to the gaseous envelope surrounding the shuttle, the particle population orbiting with the shuttle, and the optical interference from the local sources. Neutral species are tested in the bay area of the spacecraft, such as H_2O, NO, He, Freon, Ar, O_2, CO_2, N_2/CO and other heavy molecules.

The major contaminants were water and helium. This is reasonable because the materials used in the mechanical and electrical equipments rang from liquids to solids. The continuous outgassing processes contaminate the space environment and change the space pressure to some extent. The wide range of pressure and temperature variations during the spacecraft orbiting process will enhance the chance of spacecraft anomalies. From Paschen's law, when the electrode distance is fixed, electrical breakdown property is very sensitive to the local pressure in the spacecraft. At the pressures of 1 to 2 Torr, the breakdown of helium for 1 cm electrode gap is in the range of 200 Volts, which is relatively high compared with the operating voltage level in the space power systems [12]. Therefore, electrical insulation in the spacecraft should be carefully considered and never be overstressed.

1.4.2 Surface Flashover in Vacuum & Partial Vacuum

Different from the case in atmospheric pressure, the voltage hold-off capability of solid insulator in vacuum is limited by its surface breakdown voltage and is lower than that of a vacuum gap with the same dimensions [16]. Several reviews concerning the electrical behavior of insulators in vacuum have been published [16, 29-31]. In general, surface flashover of an insulator may be divided into three stages: the initiation stage, the development stage, and the final stage.

The initiation of a surface flashover is widely assumed to start with the emission of electrons from the triple junction since the equipotential lines normally concentrate in the interface among insulator, metal cathode and vacuum where small voids are unavoidable. However, there are considerable disagreements on the development stage of the discharge. Probably the most generally accepted mechanism for this stage is an electron cascade along the

surface of the insulator as illustrated in Figure 1.13. Some of the electrons emitted from the triple junction bombard the surface of the insulator, producing additional electrons by secondary emission. Some of these secondary electrons will again impact upon the insulator surface, generating tertiary electrons. Continuous development of this process leads to an electron cascade along the insulator surface and later evolves into a secondary electron emission avalanche (SEEA). This SEEA, in turn, can finally result in a complete surface breakdown. For the final stages of surface flashover, it is generally considered to occur in the desorbed surface gas or the vaporized insulator materials.

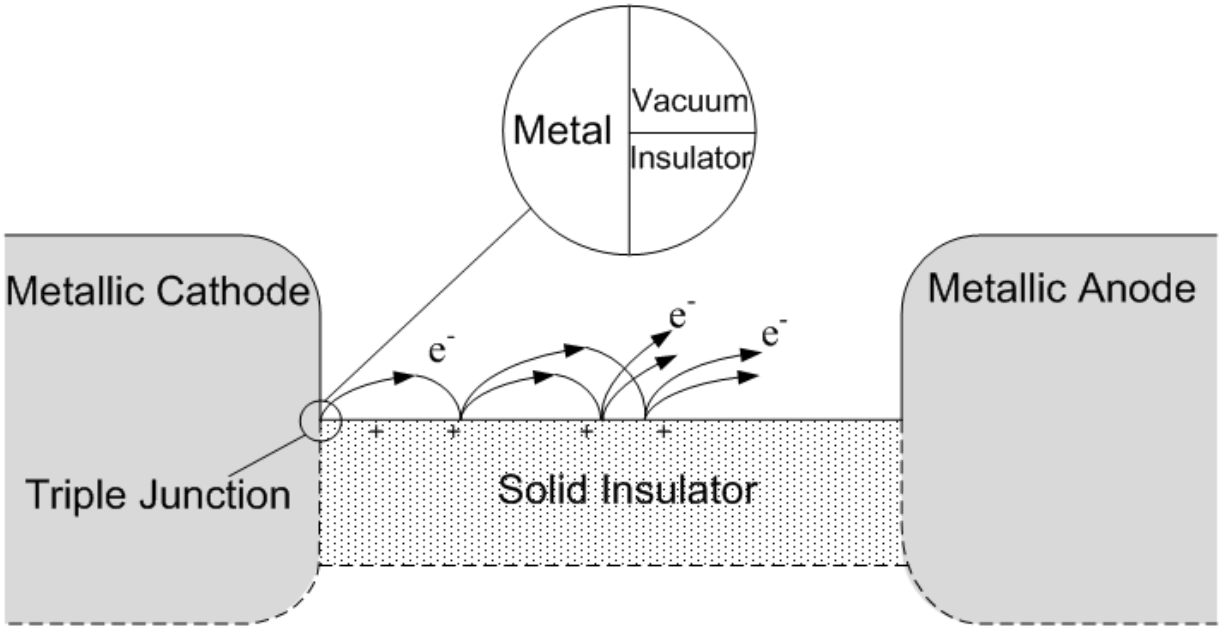

Figure 1.14 Schematic of vacuum flashover initiation from triple junction

In partial vacuum, significant work has been done on the research of surface flashover [13-14]. Based on a large amount of experiments, surface breakdown curves in partial vacuum are very similar to the well-known Paschen curve. However, more theoretical research should be conducted in this area in order to clearly explain its breakdown mechanism. This thesis focuses on surface flashover of nanodielectrics under high frequency pulsed electric fields.

CHAPTER II

HIGH VOLTAGE GENERATOR SIMULATION & APPLICATION

2.1 High Voltage DC Power Supply

High voltage DC power supply is widely employed in research work and in industry, such as electron microscope, particles accelerator, and dielectric testing. In dielectric test, the voltages are increased up to several million volts while currents are decreased to several milliamps. In our experiments, DC power supplies are necessary for the gas breakdown tests and capacitive storage charging. Therefore a 10 kV 0.1 μA DC power supply is designed for lab use.

The design employs the classic Cockroft-Walton voltage multiplier circuit, which is probably the most popular method of generating high voltages at low currents at low cost. It is highly reliable, portable and simple while useful for the research. Similar to Marx generator, a set of capacitors are charged to $2V_{s(max)}$ separately, and then provide ($2n* V_{s(max)}$) at the output when they are connected in series. All of the capacitors and diodes only need to stand a voltage of $2V_{s(max)}$, which greatly decreases the costs on components and insulation. In addition, the different voltage levels can be taken out through tapping at every stage of the multiplier circuit. However, this circuit has the disadvantage of having very poor voltage regulation, that is, the voltage drops rapidly as a function the output current. Therefore voltage multipliers are usually used in special applications where load is constant and has high impedance or where input voltage stability is not very critical, such as dielectric strength test, particle acceleration, and X-

Rays machines. Figure 2.1 is the circuit of a 3-stage 10 kV voltage multiplier. The operating principle is as follows: on the negative half-cycle of V_s, C1 charges through rectifier D1 to $V_{s(max)}$. On the positive half-cycle of V_s, rectifier D2 conducts and the peak voltage is $V_{s(max)}$ from the source and $V_{s(max)}$ from C1; that is, the capacitor C2 is charged to $2V_{s(max)}$. During the next negative half-cycle, rectifier D3 conducts and voltage which is applied to C2 is the sum of $V_{s(max)}$ from the source and $2V_{s(max)}$ from C2 less the voltage on C1; namely, C3 is charged to $2V_{s(max)}$. For higher output voltages of C4 and C6, the circuit is repeated with a cascade connection. Therefore the total output voltage reaches $2n*V_{s(max)}$ above the earth potential. But the voltage across any individual capacitor or rectifier is $2V_{s(max)}$, except for C1, which is only charged to $V_{s(max)}$. In the circuit, the AC wall power (120 V RMS, 60 Hz) is used as the input and it is boosted to 1200 V RMS by a step-up transformer. So the output voltage in this circuit is $2n*V_{s(max)}$ = 2*3*1697 = 10.18 kV.

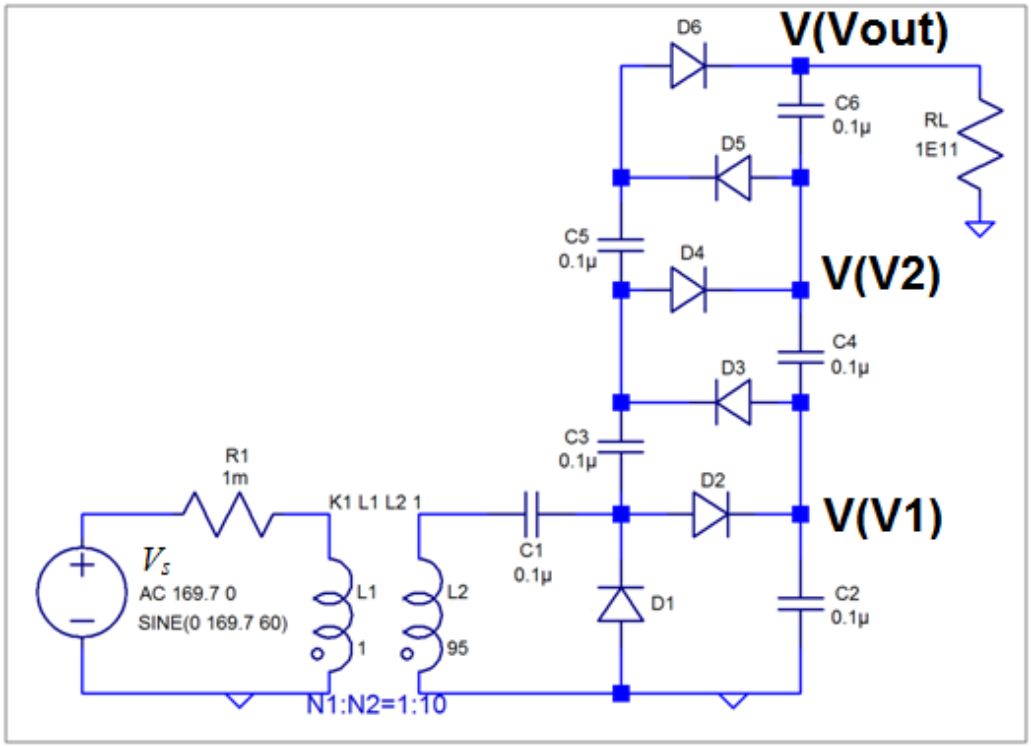

Figure 2.1 3-stage 10 kV voltage multiplier circuit

Figure 2.2 is the Spice simulation of the output voltage from different tapping points of this circuit. Figure 2.3 is the output current at full load. From the simulation, we see that the output voltage is 9.92 kV and output current is 99.2 nA at full load, both of which are consistent with the calculation. The voltage ripple, around 136 mV, is also very small.

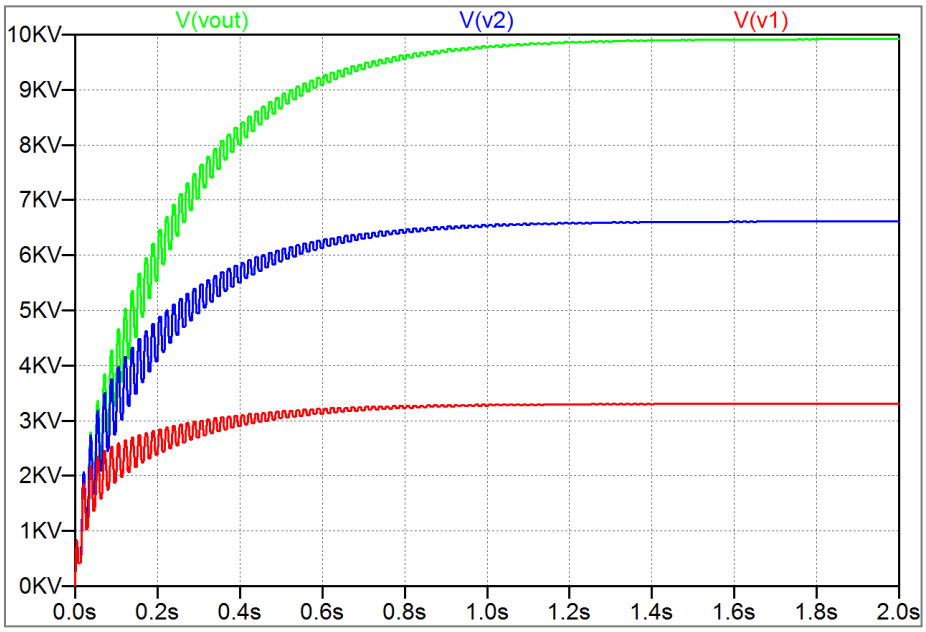

Figure 2.2 Spice simulation of output voltage from different tapping points

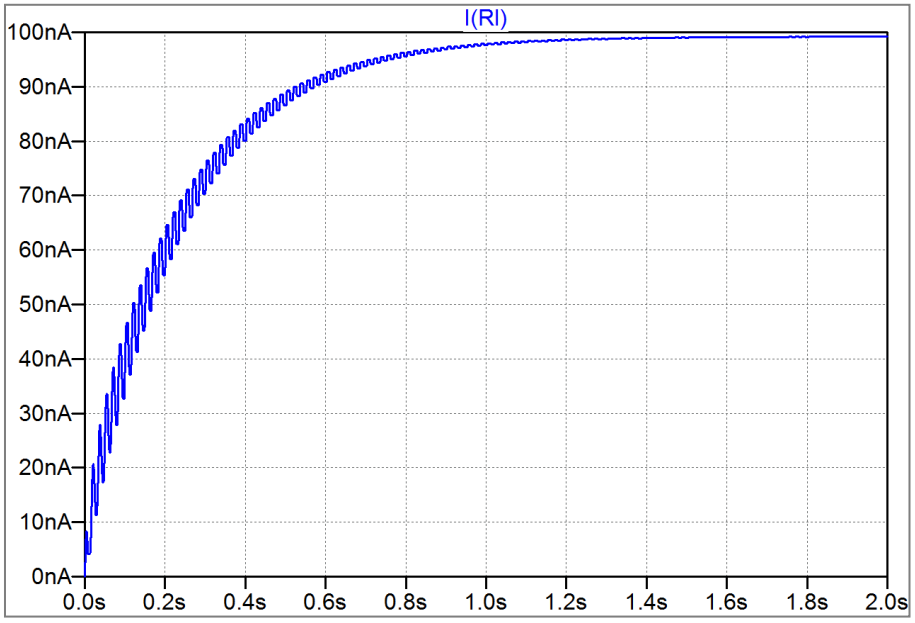

Figure 2.3 Spice simulation of output current at full load

2.2 High Voltage Pulse Generator

In our experiments, a negative pulse voltage is needed to trigger the CNT samples to emit electrons. Therefore a voltage-regulated 1 kV pulse generator is developed and constructed in the lab as shown in Figure 2.4a. Figure 2.4b is the typical waveform of its output pulse voltage, in which the magnitude of the pulse is 400 V and the delay time is approximately 1 ms. The internal circuit of this generator is adapted from [34] as illustrated in Figure 2.5.

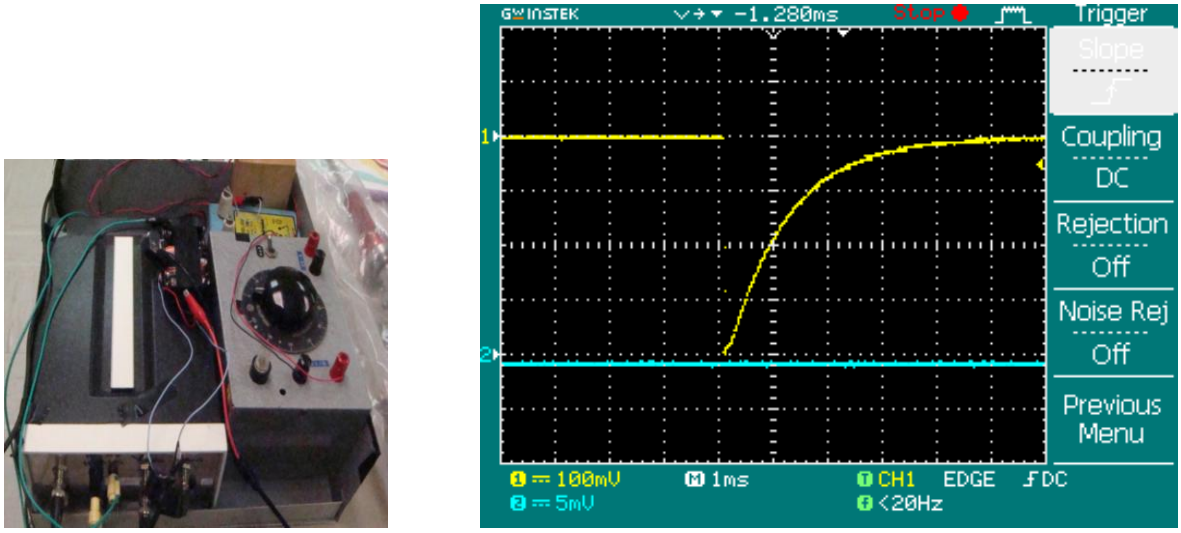

(a) (b)

Figure 2.4 In-house made voltage-regulated 1 kV pulse generator (a) prototype (b) output pulse

This circuit consists of two parts, pulse generator circuit and control circuit. For the pulse generation part, when the PowerFET Q1 is in the off state, C1 is charged to a voltage +HV via R8, R9, R10, and D1. If the PowerFET Q1 is turned on, the output of the circuit becomes −HV volts as the positive terminal of C1 is now grounded. Then the capacitor C1 discharge to the output load through Q1 and R1 immediately. For the control part, a 0/+5V signal on the input port operates the driver IC2 MAX 626, from which a 0/+12V signal is presented on the

gate of the PowerFET Q1, turning it off or bringing it into conductance. In the circuit, C2, R5, R6, R7 form a snubber network to protect the PowerFET against voltage spikes and consume the remaining current when the PowerFET is turned off. R11, R12, R13, and R14 consist of a resistor divider for the output voltage measuring, which is 1 mV/V. The short circuit and overload protection is achieved based on R1. When the output current increases, the gate-source voltage of the PowerFET decreases because of the increase of voltage drop on R2, increasing the on-resistance of the PowerFET. In this circuit, the output peak current is limited to around 40 A. IC2 TC4426 is the PowerFET driver designed to convert TTL inputs (0/+5V) to higher voltage outputs (0/+12V) to drive the gate of the PowerFET. IC1 4N25 is an optocoupler used to isolate the control circuit from the high voltage pulse circuit. The TTL signal 0/+5V is achieved by common 555 Timer circuits. The duty cycle and period of the timer circuits are determined by the time constants of the capacitor charging and discharging circuit. In our design, two timer circuits are employed to generate continuous or single TTL pulse signals. In continuous operation mode, we set the signal period of 7 s and duty cycle of 50% in order to let the capacitor fully charged to the desired high voltage level. Figure 2.6, 2.7 and 2.8 are the results from LTSpice simulation. The detailed list of the circuit file is described in Appendix A. The spice models of IC2 TC4426 and MOSFET are downloaded from the manufactures' website. Figure 2.6 is the voltage waveform of control signal from Nodes 17, 22, and 27. Figure 2.7 is the waveform of the output voltage when the output is open-circuited and the HV DC power supply is 400 V. The simulation result, -400 V pulse and 1 ms delay time, is very consistent with our in-house made pulse generator as illustrated in Figure 2.3b. Figure 2.8 is the output current waveform when the output is short-circuited. With the protection from resistor R1, the current is clapped around 38 A.

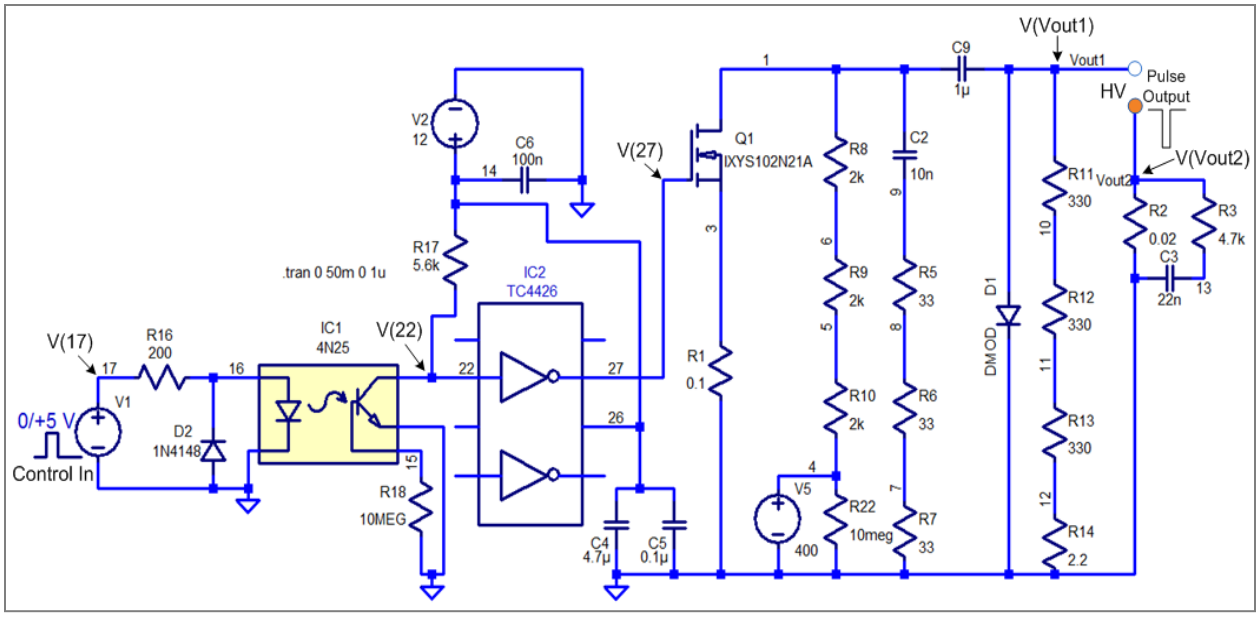

Figure 2.5 High voltage pulse circuit [34]

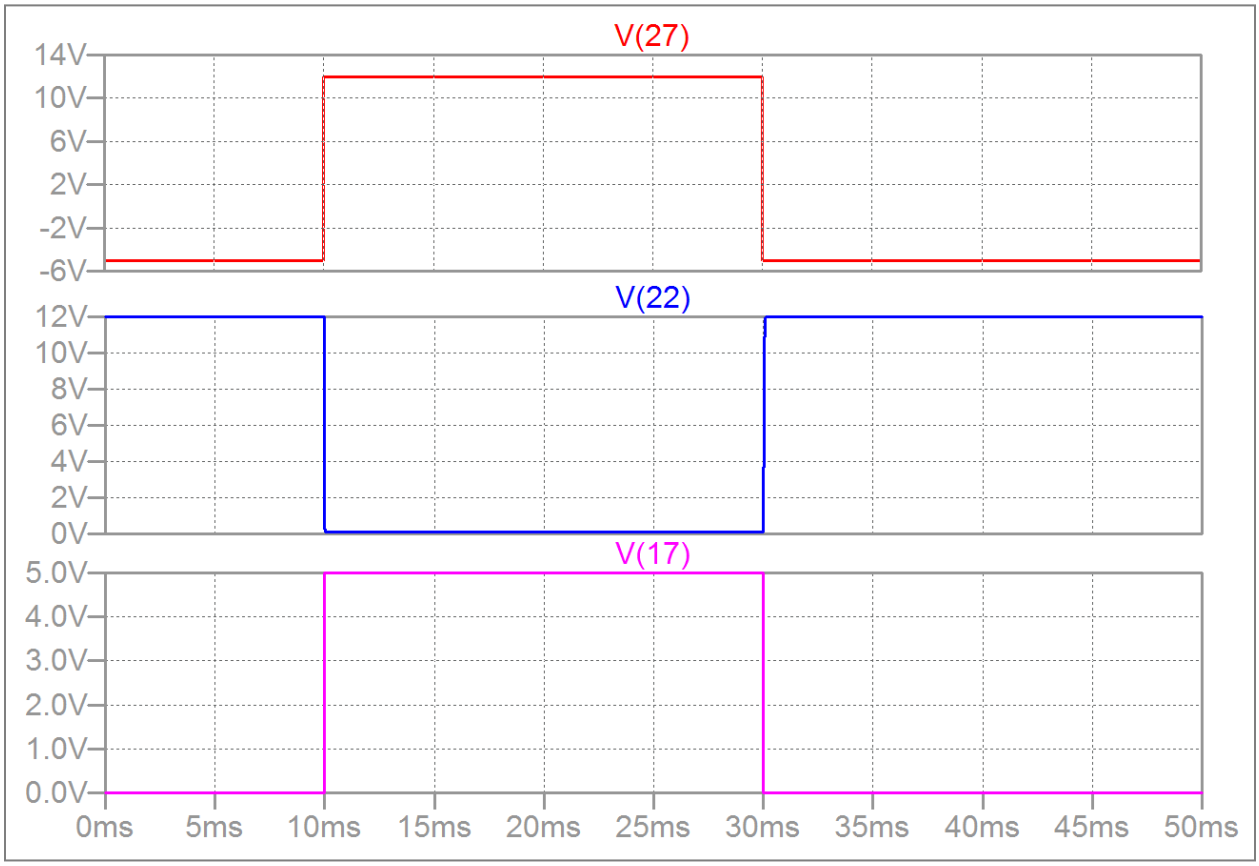

Figure 2.6 Waveform of control signal from Nodes 17, 22, and 27

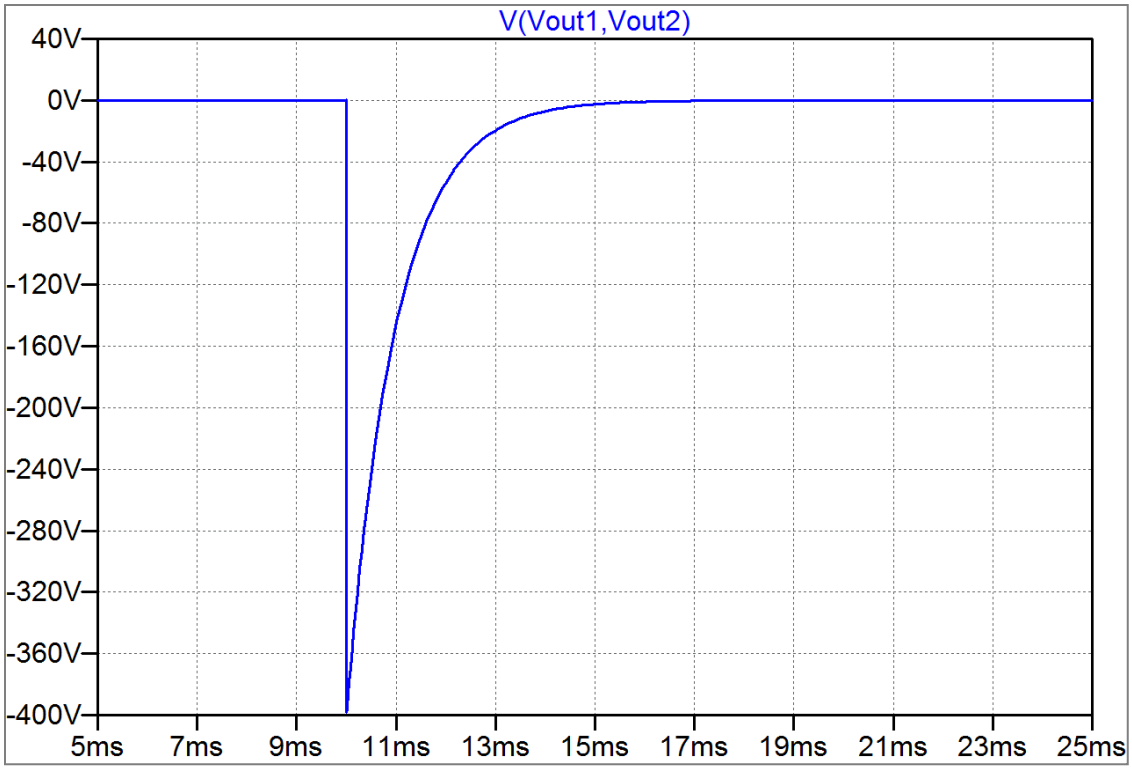

Figure 2.7 Output voltage waveform from Spice simulation

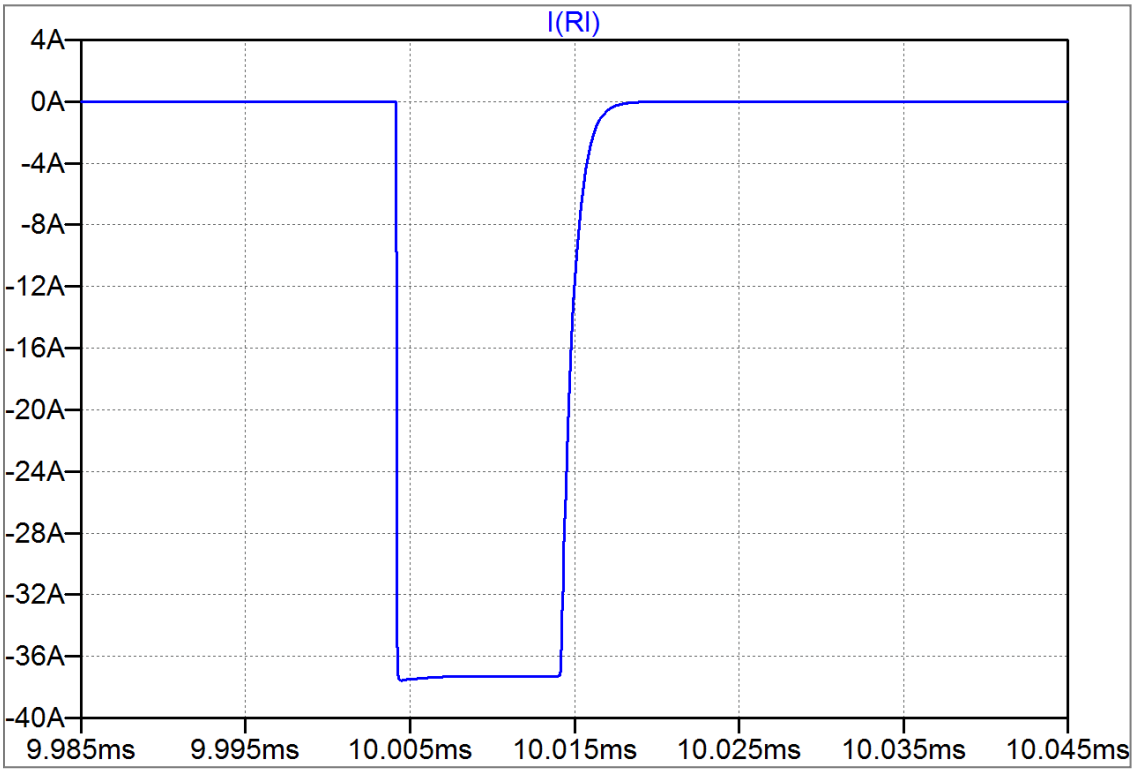

Figure 2.8 Short-circuited output current waveform from Spice simulation

2.3 Application: CNTs Initiated Hollow Cathode Discharge

This voltage-regulated 1 kV pulse generator is employed to trigger the field emission of CNTs cold cathode, which can initiate hollow cathode discharge in helium. It is a promising and practical trigger method for pseudospark switches. Hollow cathode discharge is operating on the left-hand side of the well-know Paschen curve and the hold-off voltage is significantly high, which is suitable for the high voltage and high power switching applications.

2.3.1 Experiments Setup

The CNTs initiated hollow cathode discharge setup consists of four main parts, a plane anode, a hollow cathode, a trigger electrode, and the external circuit as illustrated in Figure 2.9. Figure 2.10 is a schematic of the experimental setup. The anode is a circular plate with a diameter of 1.8 cm while the cathode is in cylindrical shape with a hollow cavity. A hole with a diameter of 2 cm machined on the cathode front surface which is placed opposite to the plate anode with a spacing of 3 mm. Both of the cathode and anode electrodes are made from copper and well polished. The trigger electrode holder is aluminum with CNTs attached on the top and is inserted into the hollow cathode cavity. The whole electrodes setup is enclosed in an 8 cm long and 2 cm diameter quartz tube, serving as the vacuum chamber sustaining 10^{-6} Torr for several days. In addition, the anode is connected to an adjustable 35 kV DC power supply and the hollow cathode is grounded. The trigger electrode is connected to a voltage-regulated negative pulse generator described in the previous section (see Figure 2.4a). The maximum magnitude of the output pulse voltage is 1 kV. In the experiment, helium is fed into the well-sealed chamber and the operating pressure is kept from a few mTorr to 150 mTorr.

The acquisition system is consisted with oscilloscope, current probe, high voltage probe, and high speed camera. The voltage between anode and hollow cathode and the pulse voltage between the trigger electrode and ground are monitored. The first voltage is attenuated by 2000 and the second one is attenuated by 1000 for oscilloscope measurements. The current waveform is also recorded from a current probe. The high-speed camera on the top of the chamber is installed to capture the plasma formation process of helium hollow cathode breakdown. Comprehensive discussion of this work is given in [26], and only a summary of the work outlined in the following section.

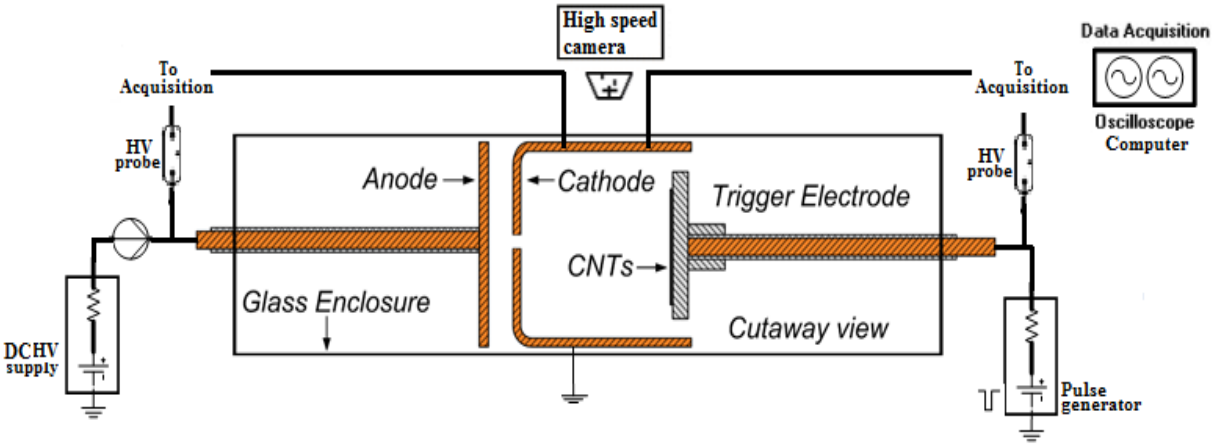

Figure 2.9 Electrodes setup in CNTs initiated hollow cathode discharge [26]

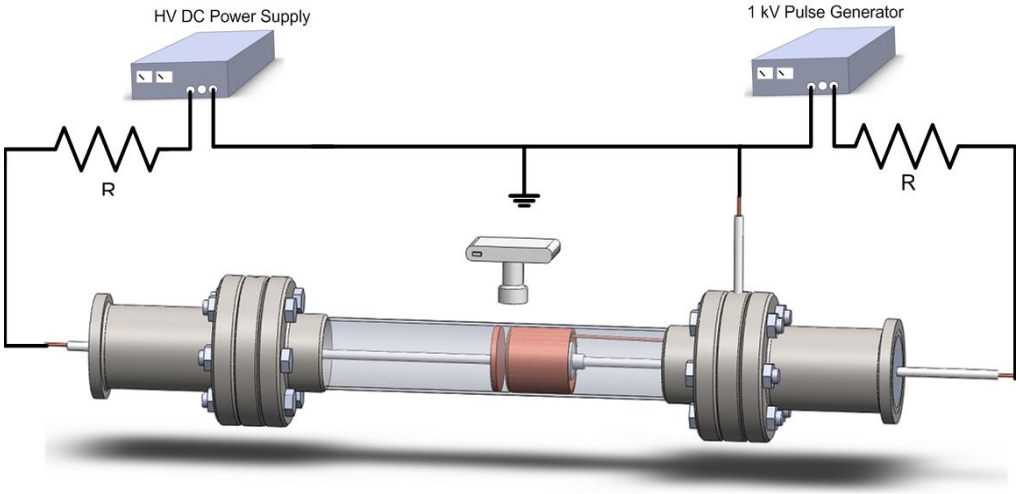

Figure 2.10 Schematic of the experimental setup

2.3.2 Experiment Results & Discussions

Delay time is one of the most important parameters in terms of how efficiently the energy is transferred to the load by the high voltage and high power switches. In this work, we will concentrate on the study of time delay under different trigger voltages and different CNTs samples. From the static self-breakdown (hold-off voltage) test in [26], 100 mTorr is selected as the operating pressure and 12 kV is set as the hold-off voltage between the anode and hollow cathode in our delay time test. At the fixed chamber pressure and hold-off voltage, several randomly oriented CNTs samples with different growth time are employed to initiate the hollow cathode breakdown. The waveforms of the negative trigger pulse and hold-off voltage are recorded when the breakdown events occur. Table 2.1 is a list of samples studied in our experiments. Figure 2.11 is the image of CNTs initiated helium hollow cathode discharge with sample R-40. Similar to the hold-off test, the plasma filled out the hollow cathode cavity and went through the cathode towards the anode immediately. Figure 2.12 is the typical waveforms of hold-off voltage (top) and trigger pulse voltage (bottom) when breakdown event occurs. The hold-off voltage drops in a few microseconds when the trigger pulse is applied. The delay time is defined as the time difference between the initial drop points between the trigger and hold-off voltage.

In our experiments, for a particular CNTs sample, five trigger pulse voltages, 200V, 400 V, 600 V, 700 V, and 800V, are used to initiate the hollow cathode breakdown. However, only the sample R-120 can initiate the breakdown at trigger pulse voltage of 200V. Figure 2.13 shows the delay time as a function of trigger pulse voltage for different CNTs samples [26]. The delay time of different samples ranges from 2 to 10 microseconds. It is clearly shown that the delay time decreases with the increasing trigger voltage for each sample. It may be because as the

applied trigger pulse voltage becomes higher, more intense electron emission from the CNTs samples takes place which is able to initiate the hollow cathode discharge much faster. From the figure, we could also see that the delay time becomes smaller when the growth time of the CNTs samples increases. This is expected since compared to the CNTs samples with shorter growth time, the samples with longer growth time are much denser and longer and have much lower turn-on electric field, which is much easier for these CNTs samples to emit enough electrons in relatively shorter time and initiate the final breakdown.

Table 2.1 CNTs sample list

Samples Name	Grow Time
R-20	Randomly oriented CNTs with 20 min growth time
R-40	Randomly oriented CNTs with 40 min growth time
R-80	Randomly oriented CNTs with 80 min growth time
R-120	Randomly oriented CNTs with 120 min growth time

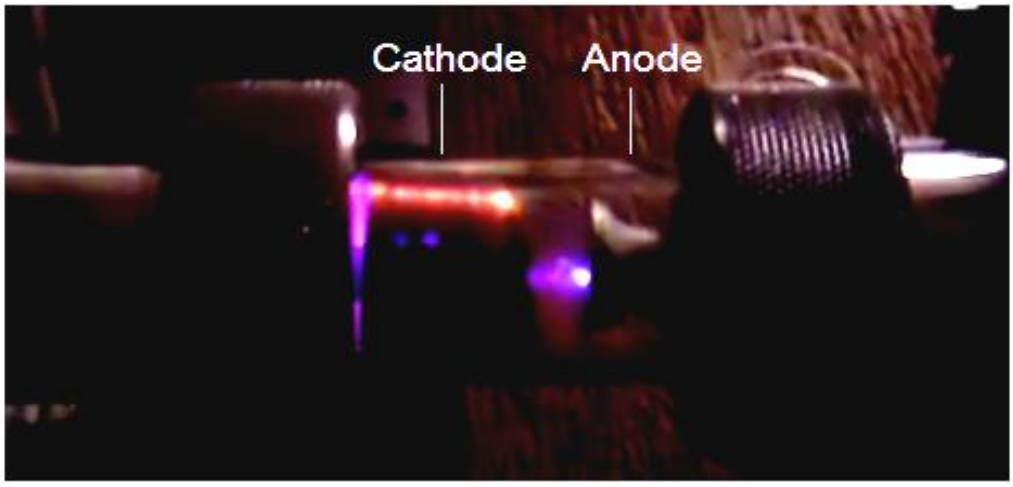

Figure 2.11 Image of CNTs initiated hollow cathode discharge with sample R-40 [26]

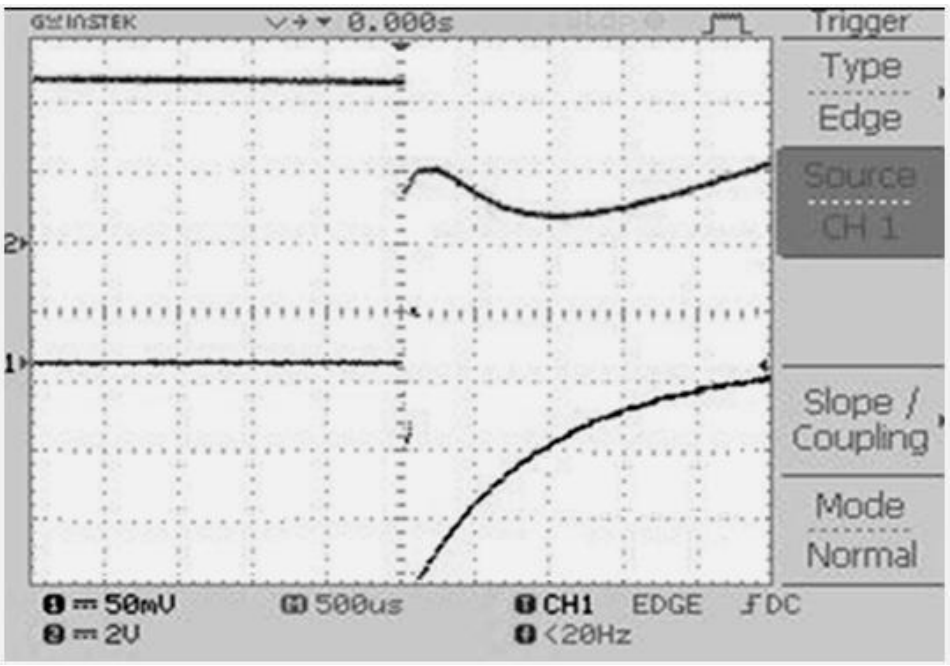

Figure 2.12 Typical hold-off voltage and trigger pulse waveforms when breakdown event occurs

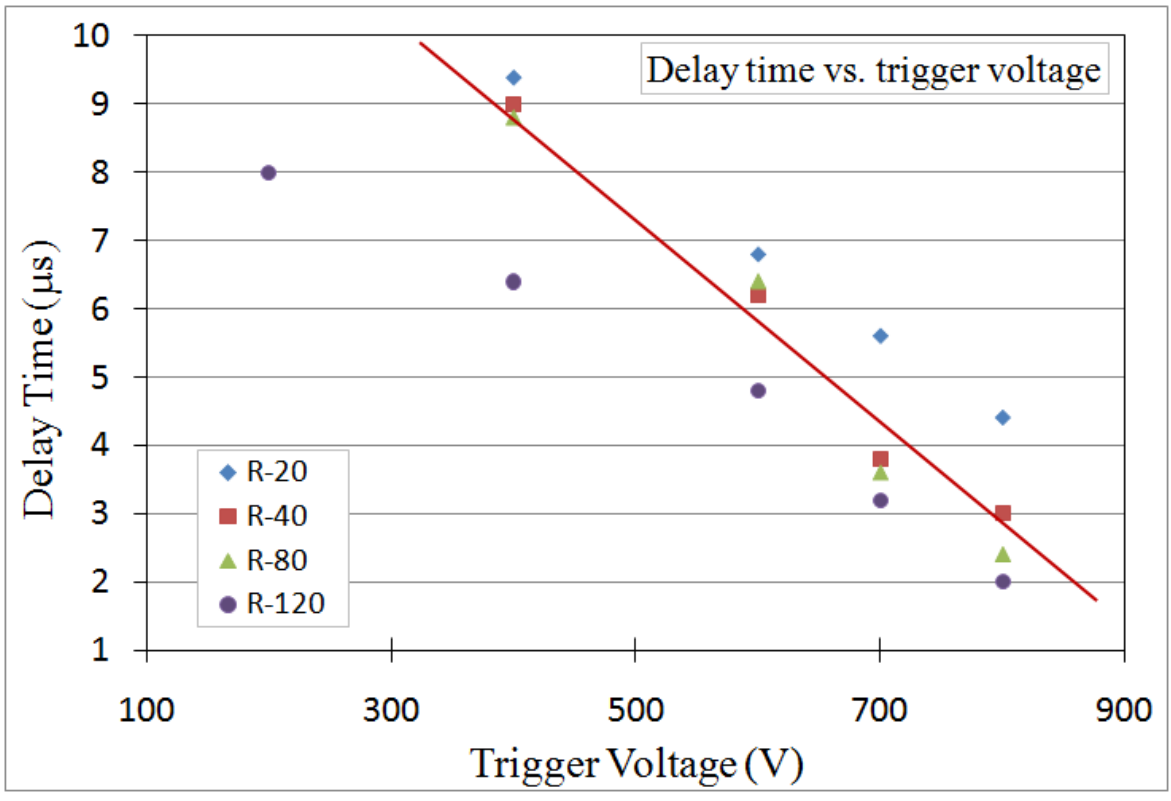

Figure 2.13 Delay time as a function of trigger voltage for different samples [26]

CHAPTER III

SURFACE FLASHOVER IN PARTIAL VACUUM

This chapter mainly describes the experiments on surface flashover in partial vacuum. The chapter is organized from the samples and electrodes preparation and experimental setup to experiment results and discussions. Several experimental conditions influencing surface flashover are taken into consideration in this work.

3.1 Samples Preparation & Electrode Geometries

The samples except the control samples are produced by adding nanoscale Al_2O_3 or TiO_2 powder into the epoxy resin with specific weight ratios. The epoxy resin is prepared by mixing the EPO-THIN resin (20-8140-032) and EPO-THIN hardener (20-8140-016) with 5:2 ratio first, then either Al_2O_3 or TiO_2 dielectric particles (powder from Alfa Aesar) are added to the mixture and set to cure according to the manufacturers specification. The aluminum-oxide (Al_2O_3) is 99.98% pure with 850 to 1000 nm sized particles and the titanium dioxide (TiO_2) is 99.9% pure with 32 nm sized particles. The weight ratios between the powder and epoxy are 1:50 (2%) and 1:16.6 (6%) separately. For the control sample, no nano-particles are added into the epoxy resin. All of the mixtures are kept in the small cylindrical containers and cured at room temperature for 24 hours. The final samples are cut into 1-cm length and surfaces are machined. Figure 3.1 shows the preparation procedures of the nanodielectric samples. The final samples are cylindrical shaped with the diameter of 3 cm and thickness of 1 cm. In addition, in order to

study the surface effect on the surface flashover, the top surfaces of those samples used in the lateral electrode configuration test are machined as shown in Figure 3.2. Table 3.1 is a list of all the samples prepared in our experiments.

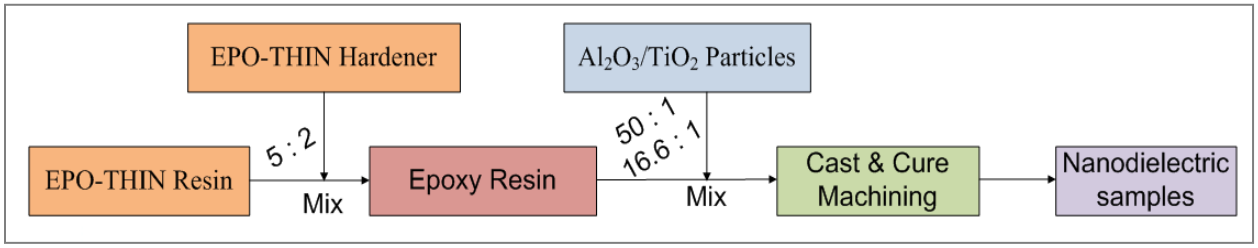

Figure 3.1 Nanodielectric samples preparation processes

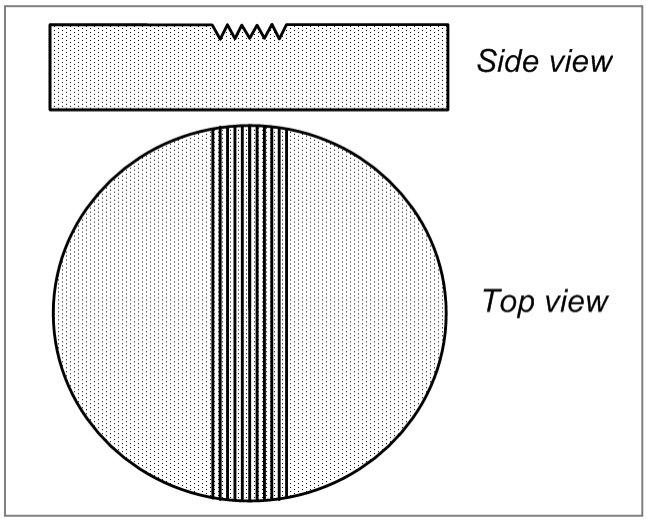

Figure 3.2 Schematic of surface machined samples

Table 3.1 Nanodielectric samples list in the experiment

Sample Name	Nano-particle additives	Weight ratio between additives and epoxy resin	
CS (Control Sample)	N/A	N/A	* Total two samples for each (flat surface and textured surface)
S-A2	Al_2O_3	1:50 (2%)	
S-A6		1:16.6 (6%)	
S-T2	TiO_2	1:50 (2%)	
S-T6		1:16.6 (6%)	

Two different kinds of electrode architectures are studied in this research; the sandwiched and the lateral as shown in Figure 3.3. The sandwiched configuration is achieved by holding the samples firmly between two parallel plate electrodes and the lateral configuration is realized by placing a pair of electrodes on the surface of the samples. For the sandwiched setup, although the sample thickness is 1 cm, the path across the two electrodes on the surface of the sample is 1.6 cm. Therefore, the electrode spacing for this configuration is 1.6 cm while the electrode spacing for the lateral configuration is 0.7 cm. The electrodes for the sandwiched configuration are made of aluminum and for the lateral configuration they are copper.

3.2 Experimental Setup

The test fixture (the electrodes and the sample) is placed in a high vacuum chamber and the electrodes are connected to an adjustable high voltage power supply (either DC or pulse generator). For each sample, a DC applied field is used initially, and then a high frequency pulsed field is applied. A pulsed high voltage source which can generate a unipolar square pulse train with frequencies from 15 kHz to 220 kHz with varying duty cycle is used for the high frequency tests. The pulse generator is fed from a function generator and a high voltage DC power supply. The magnitude, frequency, and duty cycle of the output pulses are adjusted according to the test sequence. Nitrogen is selected as the working gas and the pressure in the chamber is varied from 100 mTorr to 900 mTorr or 3000 mTorr throughout the experiments. The current probe, oscilloscope, photomultiplier (PMT) and pico-ampere-meter are used as part of the data acquisition system as shown in Figure 3.4. The high-speed camera on the top of the chamber is employed to capture the plasma formation process of surface flashover events.

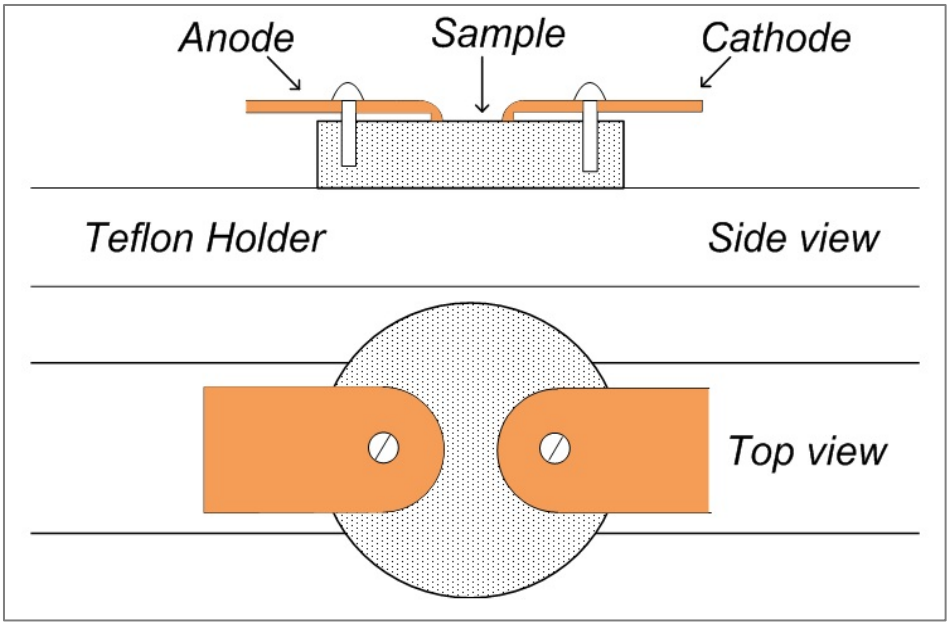

(a)

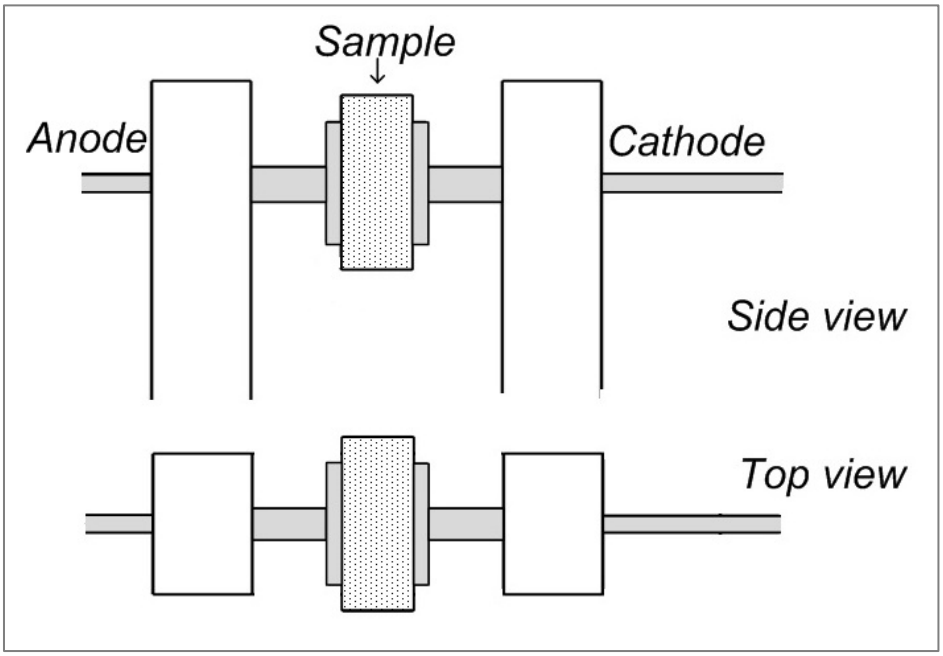

(b)

Figure 3.3 Schematics of the electrodes setups (a) sandwiched; (b) lateral

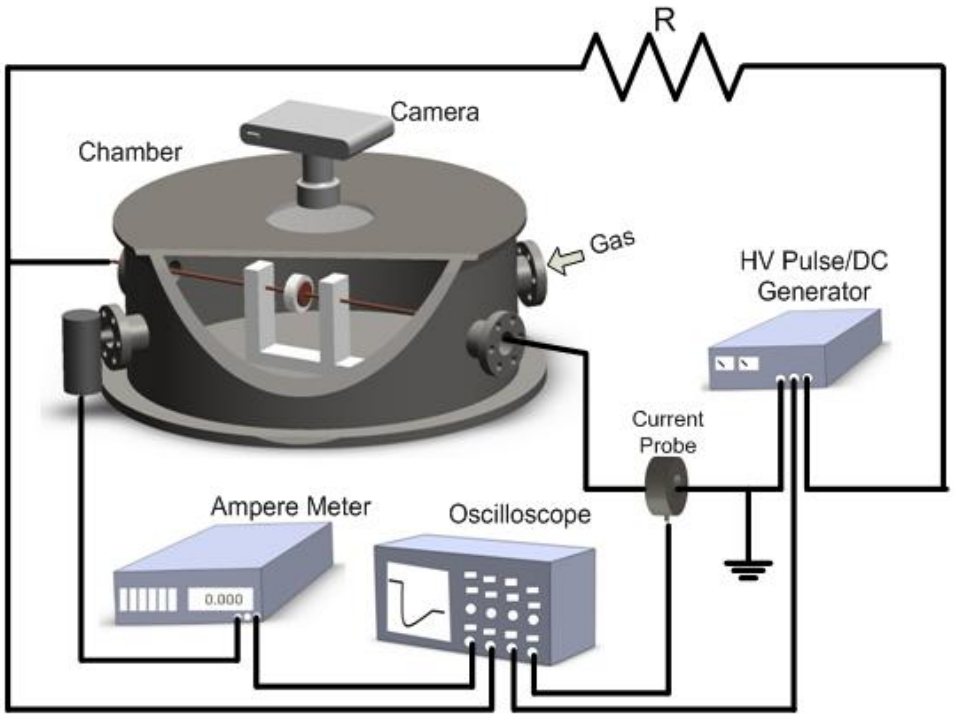

Figure 3.4 The experimental setup employed in the surface flashover study

3.3 Experimental Procedure

Surface flashover voltage as a function of pressure (pressure sweep), as a function of frequency (frequency sweep), and as a function of duty cycle (duty cycle sweep) are recorded and plotted in sequence. In the pressure sweep experiment, for each pressure data point a constant pressure value is set and a DC or 20 kHz unipolar square pulse voltage is applied by gradually increasing the voltage (approximate rate of 100 V/s) until a breakdown event occurred and the light emission from the breakdown triggered the data acquisition system with the assistance of the PMT. For the pressure sweep experiments with the high frequency pulsed field, the frequency of the field is set to 20 kHz with 50% duty cycle, then the voltage is increased until a breakdown event occurred. The waveforms of voltage, current and light intensity during the surface flashover are recorded. Between three to five breakdown voltages are recorded for each

fixed pressure and then averaged to generate a data point for this particular pressure. In this way, the surface breakdown voltage is obtained for the pressure range specified in the study. For the frequency sweep experiments, the pressure value at which the breakdown voltage has a minimum is determined first then this value is set as the constant pressure. Based on the pressure sweep data, we selected the fixed pressure to be 300 mTorr in the sandwiched configuration and 900 mTorr in the lateral one. In the frequency sweep experiment, we keep the pulse duty cycle to be 50%, but changed the frequency from 20 kHz to 220 kHz. The same experimental procedures are used in this case also and the breakdown events are recorded for each particular frequency at this fixed pressure then plotted as a function of frequency. For the duty cycle sweep test, all procedures are the same as frequency test except the frequency is fixed at 20 kHz and the duty cycle is varied from 10% to 90%. The breakdown events are recorded for each particular pulse duty cycle at the predetermined fixed pressure then plotted as a function of duty cycle. Table 3.2 is a detailed list of the test conditions specified in different experiments.

Table 3.2 Test conditions in surface flashover experiments

Tests	Configurations	Pressure (mTorr)	Frequency (kHz)	Duty Cycle (%)
Pressure Sweep	Lateral	100 ~ 3,000	DC	DC
			20	50
	Sandwiched	100 ~ 900	DC	DC
			20	50
Frequency Sweep	Lateral	900	15 ~ 220	50
	Sandwiched	300	15 ~ 220	50
Duty cycle Sweep	Lateral	900	20	10 ~ 90
	Sandwiched	300	20	10 ~ 90

3.4 Breakdown Voltage versus Pressure

Figure 3.5 shows a representative voltage, current and light emission waveforms for a DC surface flashover event. From this figure we clearly see the voltage drops with a sudden increase

of light intensity and current increases when the surface flashover occurs across the sample. The surface breakdown voltage is defined as the point at which the voltage across the sample collapses as marked on the figure. Figure 3.6 are the images of the fully developed plasma after a surface breakdown event for both the lateral and sandwiched electrode configurations. The plasma bridges the anode and cathode across the surface of the sample. Figure 3.7 shows the voltage, current and light emission data for pulsed applied field at 20 kHz frequency with 50% duty cycle.

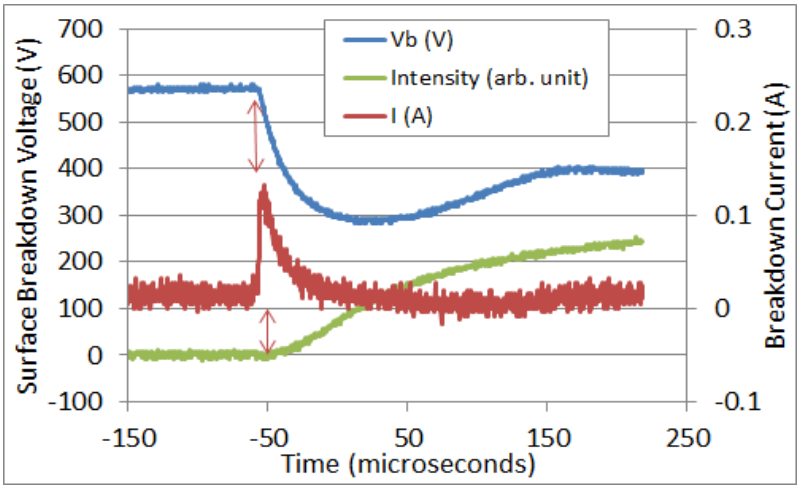

Figure 3.5 Voltage, light intensity and current waveforms of control sample with sandwiched electrode configuration during flashover at 500 mTorr under DC voltage

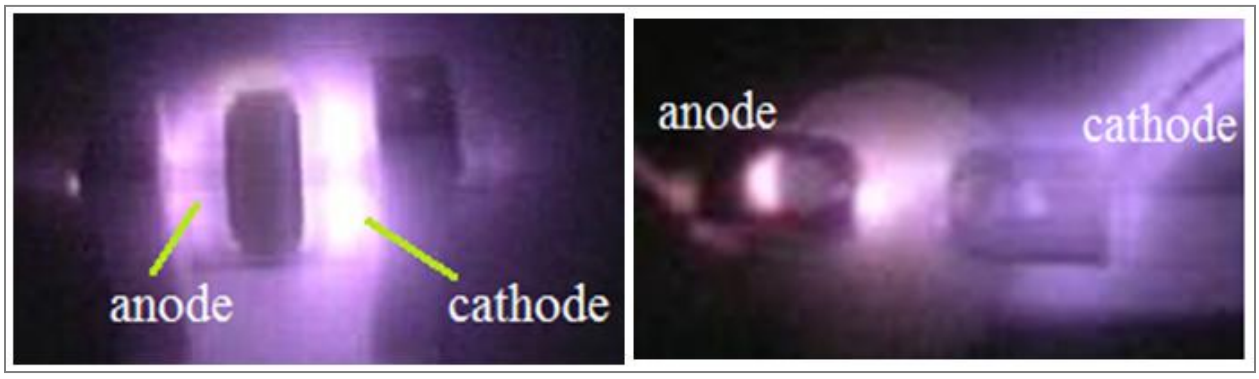

Figure 3.6 Images of the fully developed plasma after a surface breakdown event

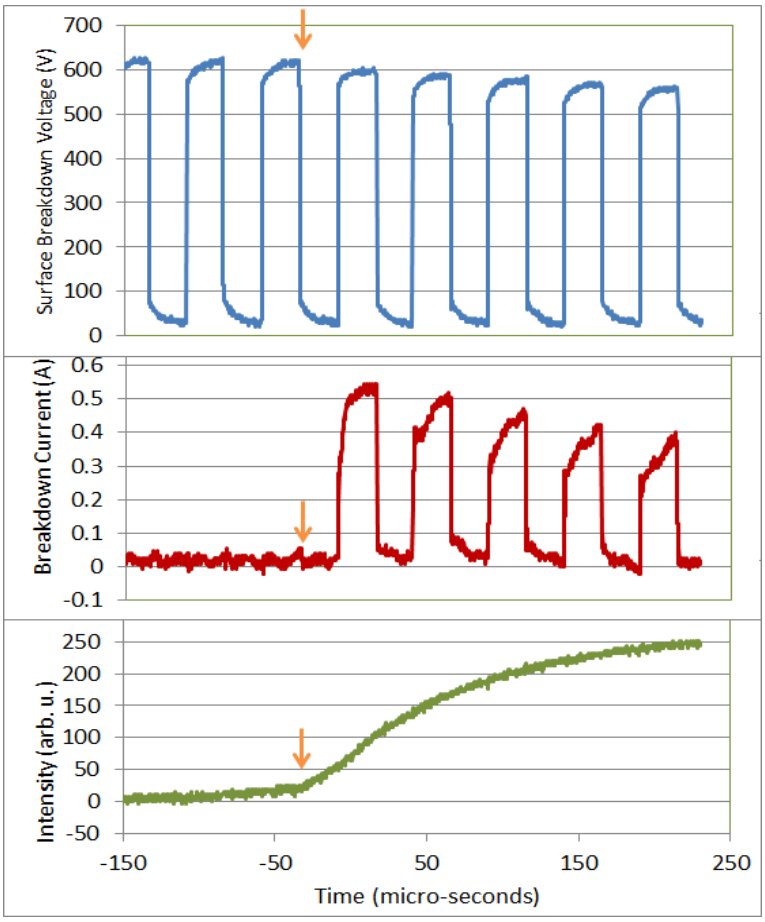

Figure 3.7 Voltage, light intensity and current waveforms of control sample with sandwiched electrode configuration during flashover at 500 mTorr under pulsed voltage

3.4.1 DC Breakdown Voltage versus Pressure

The breakdown voltages of different samples under varying pressure are collected and analyzed. In the experiment of sandwiched setup, the pressure in the chamber was changed from 100 mTorr to 900 mTorr with steps of 50 mTorr and several breakdown data for each pressure are recorded as described in Chapter 3.3. For the lateral configuration, the pressure range was from 100 mTorr to 3,000 mTorr.

Figure 3.8 shows the DC surface breakdown voltages of different samples as a function of the product of pressure and electrodes gap distance (*pd*). As expected for all samples, the

breakdown curve resembles the well-known Paschen curve. There is always a minimum surface breakdown voltage occurring in our tested pressure range. This corresponds to an approximate *pd* value of 700-800 mTorr cm for the sandwiched electrode configuration as shown in Figure 3.8a. The minimum DC surface breakdown voltage is approximately 525 V for the sandwiched configuration. A representative curve showing the trend is included in the plot.

It was observed that in the sandwiched electrode configuration, in some cases the breakdown occurred between the wires instead of across the electrodes over the sample. Although these data points are not included in the plot, there is little correlation between the surface breakdown data of loaded samples. On the other hand it is clear that the surface breakdown of the control sample (with no loading) has the lowest value among all other samples.

For the lateral electrode configuration, the surface breakdown voltage has the same trend as the sandwiched electrode configuration as shown in Figure 3.8b. The minimum breakdown voltage corresponds to a *pd* value of approximately 600 to 700 mTorr cm in this case. This is about 100 mTorr-cm shift to the lower pressure range compared to the sandwiched electrode configuration. The minimum DC surface breakdown voltage is approximately 535 V for the lateral configuration.

In the lateral case, the breakdown voltage is more predictable in the lower pressure range than the sandwiched case. Contrary to the sandwiched electrode configuration, the sample S-T6 (the 6% TiO_2 filled) has the lowest surface breakdown data. Closer examination shows that at lower pressures, the breakdown data does not follow the expected shape. Therefore, we speculate that there may be an experimental or instrumental irregularity with the data collection set. Furthermore, the sample S-A6 (the 6% Al_2O_3 filled) has the highest surface breakdown characteristics only under sandwiched electrode configuration as seen in Figure 3.8a.

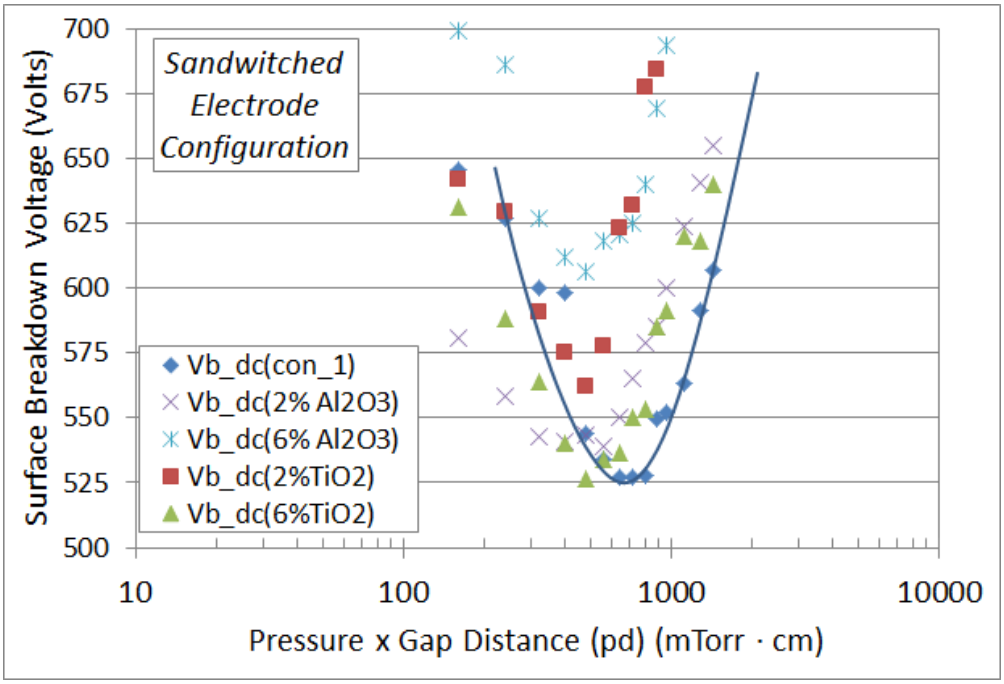

(a)

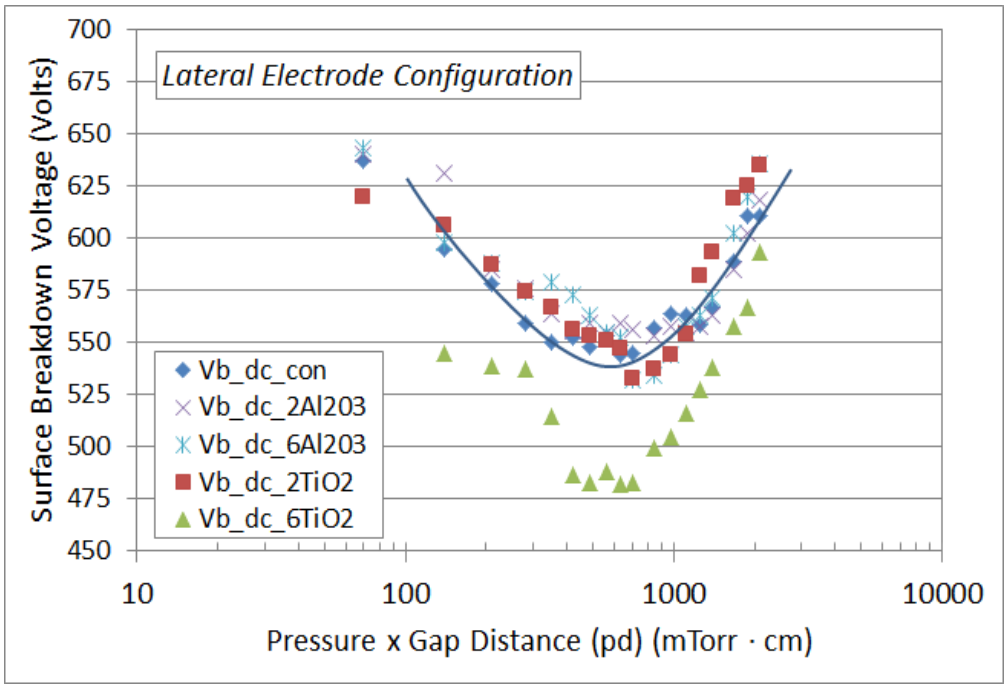

(b)

Figure 3.8 DC surface breakdown voltage vs. (*pd*) for different samples (a) for the sandwiched electrode configuration (b) for the lateral electrode configuration

3.4.2 Pulsed Breakdown Voltage versus Pressure

Similar to the dc experiments, the breakdown voltages of different samples under varying pressure and 20 kHz 50% duty cycle applied pulsed field are collected and analyzed. Figure 3.9 shows the pulsed surface breakdown voltages of different samples as a function of *pd*. Similar to the dc data, the breakdown curves have a minimum breakdown voltage at a certain *pd* range occurring at around 450 mTorr cm for sandwiched electrode configuration and 700 mTorr cm for the lateral configuration.

Furthermore, although the difference is small, the dc surface breakdown seems to be slightly higher than the pulsed case. Figure 3.10 shows the surface breakdown curves of the control sample and S-T2 (the 2% TiO_2 filled) sample under dc and pulsed applied fields. It is clear that high frequency surface breakdown is relatively lower than the dc case for these samples. This is in agreement with the literature data where the breakdown strength of dielectrics decrease as frequency of applied field is increased. Similar observation is made for the other filled samples also; however, in general, the current data is relatively scattered and no a clear observation can be made at this time.

In addition, with the limited data, the trend does not seem to be proportional to the loading percentage. We expect that different loading ratios of nano-particles play a role on the electrical properties of these samples. Specifically, there may be a different critical loading ratio for different nano-particles in improving the insulation properties of dielectric materials. In our experiments, the samples S-T6 (the 6% TiO_2 filled) performed better, with higher surface breakdown voltage compared to non-filled samples, whereas for the Al_2O_3 loaded samples, 2% seems to be an optimum loading ratio. However, further studies are needed for explaining this critical loading ratio.

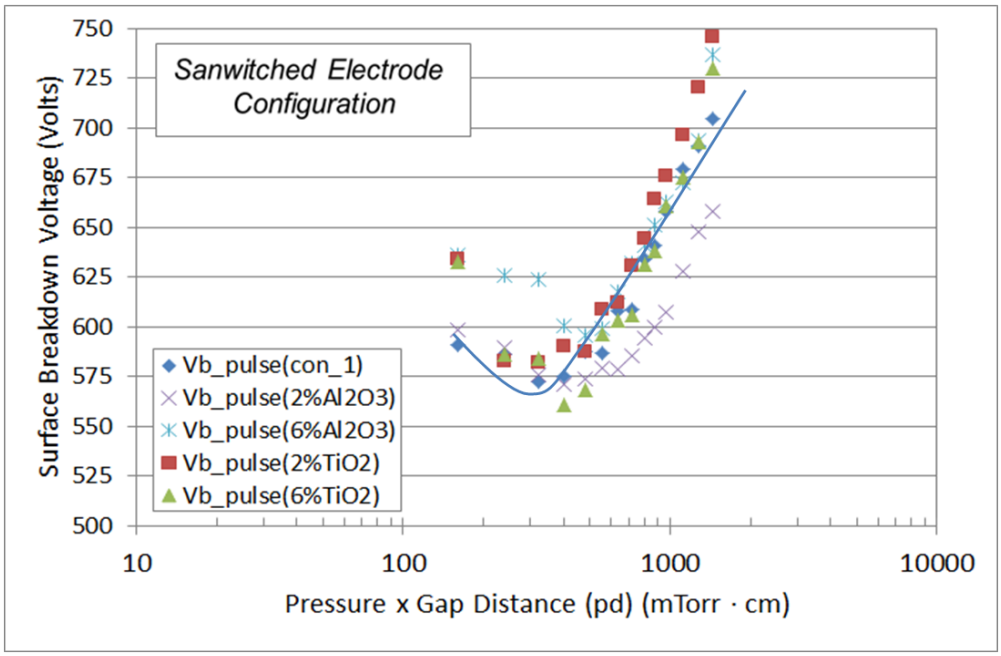

(a)

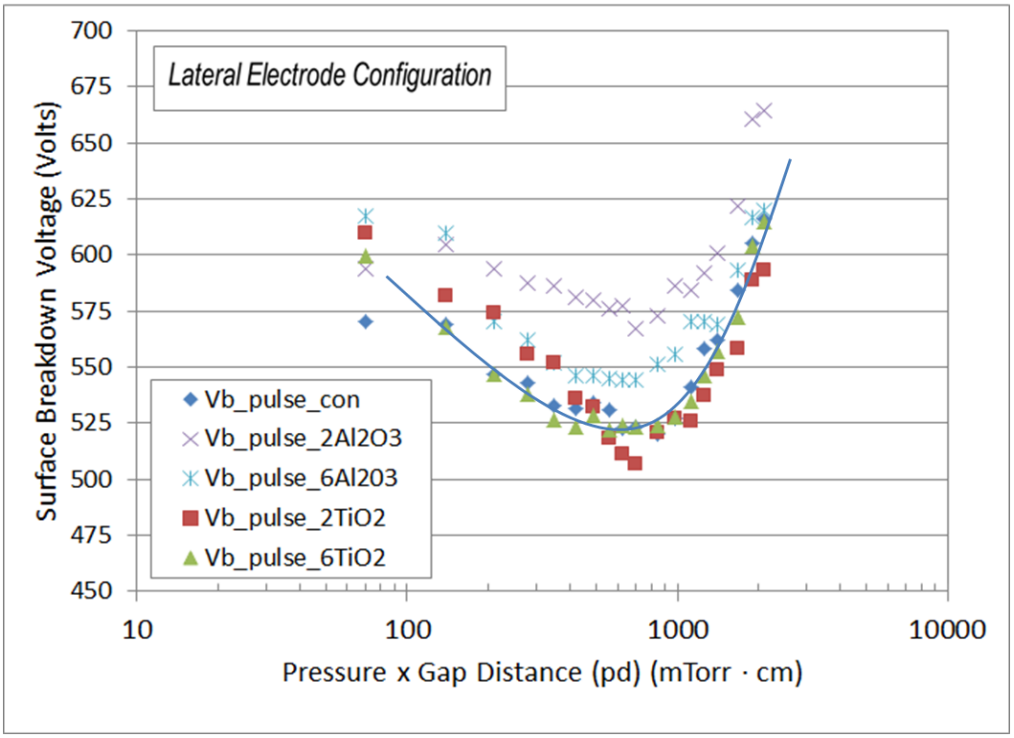

(b)

Figure 3.9 Pulsed surface breakdown voltage vs. (*pd*) for different samples (a) for the sandwiched electrode configuration (b) for the lateral electrode configuration

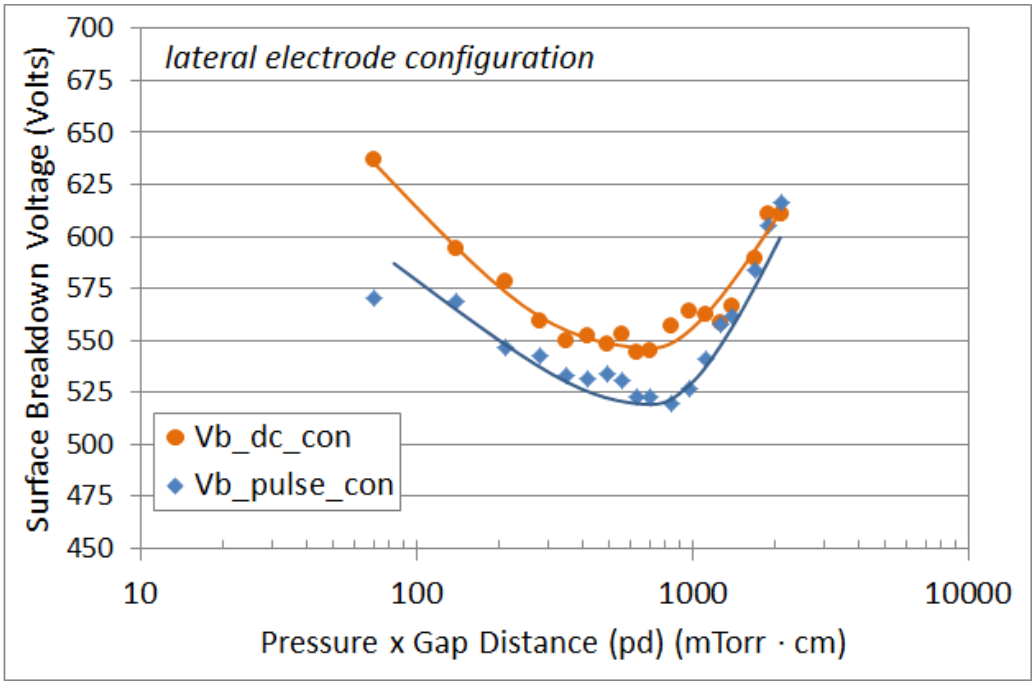

(a)

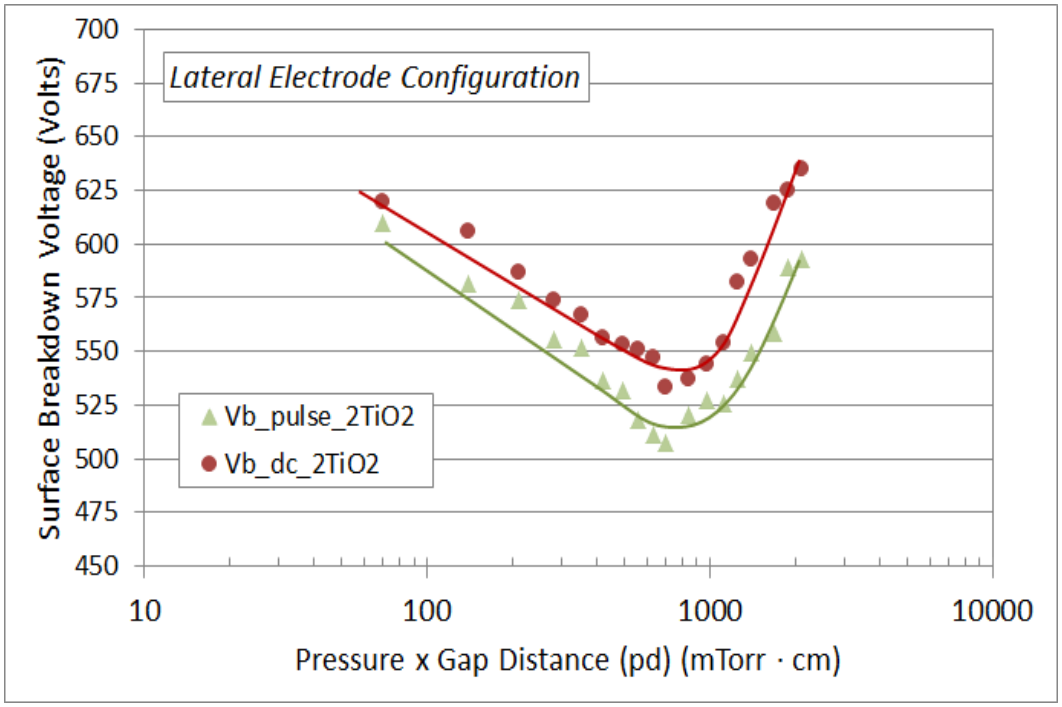

(b)

Figure 3.10 Surface breakdown curves of the control sample and S-T2 sample under dc and pulsed applied fields

3.5 Electrode Configurations Effect on Breakdown Voltage

We also observed some differences in surface breakdown voltages between the sandwiched and lateral electrode configuration. As stated earlier, the electrode gaps are different for these two configurations. Therefore, we plotted the surface breakdown voltages as a function of the product of the pressure and the gap distance (*pd*) to allow better understanding of the data. Figure 3.11 shows the comparison of the pulsed surface breakdown curves of the control and S-T2 (the 2% TiO_2 filled) samples for both the sandwiched and lateral configuration. From Figure 3.11a, we see that the minimum breakdown voltage corresponds to a *pd* value of 400 mTorr·cm and 800 mTorr·cm respectively. The corresponding minimum surface breakdown value is 570 V for sandwiched configuration and 520 V for the lateral case. On the other hand, we see relatively different behaviors for the pulsed surface breakdown voltage. In this case, the surface breakdown voltage is substantially lower than sandwiched electrode configuration with *pd* minimum shift to higher values for the control sample. Table 3.3 shows the differences of $((pd),V_{min})$ between the sandwiched and lateral electrode configurations. Normally a shift around 100-300 mTorr·cm between two different configurations could be found. Table 3.4 is a detailed surface breakdown voltage comparison between sandwiched & lateral electrode configurations at *pd* of 1200 and 300 mTorr·cm. It clearly shows that at higher *pd*, the surface breakdown voltage in sandwiched configuration, whether DC or pulsed electric field, is significantly greater than that in lateral configuration. The difference could even reach a couple of hundred volts. With the *pd* decreasing, the difference between the surface breakdown voltages under two configurations becomes smaller, which is normally less than 50 V. However, there is an exception for the sample S-A2 (the 2% Al_2O_3 filled) whose DC breakdown voltage under the sandwiched configuration is 30 V lower than the lateral case.

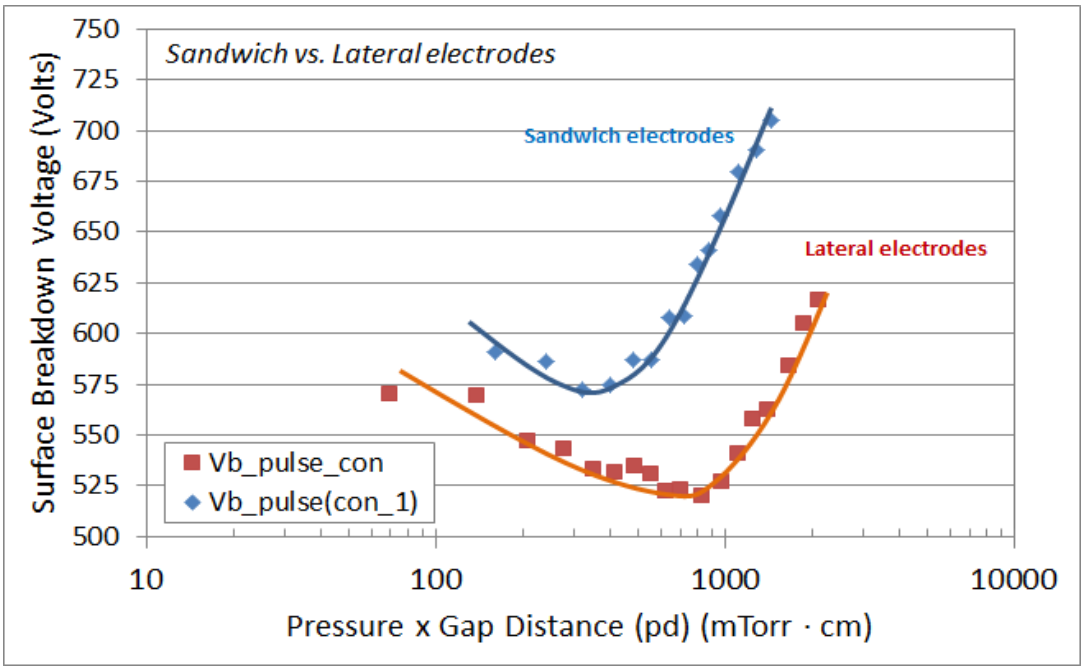

(a)

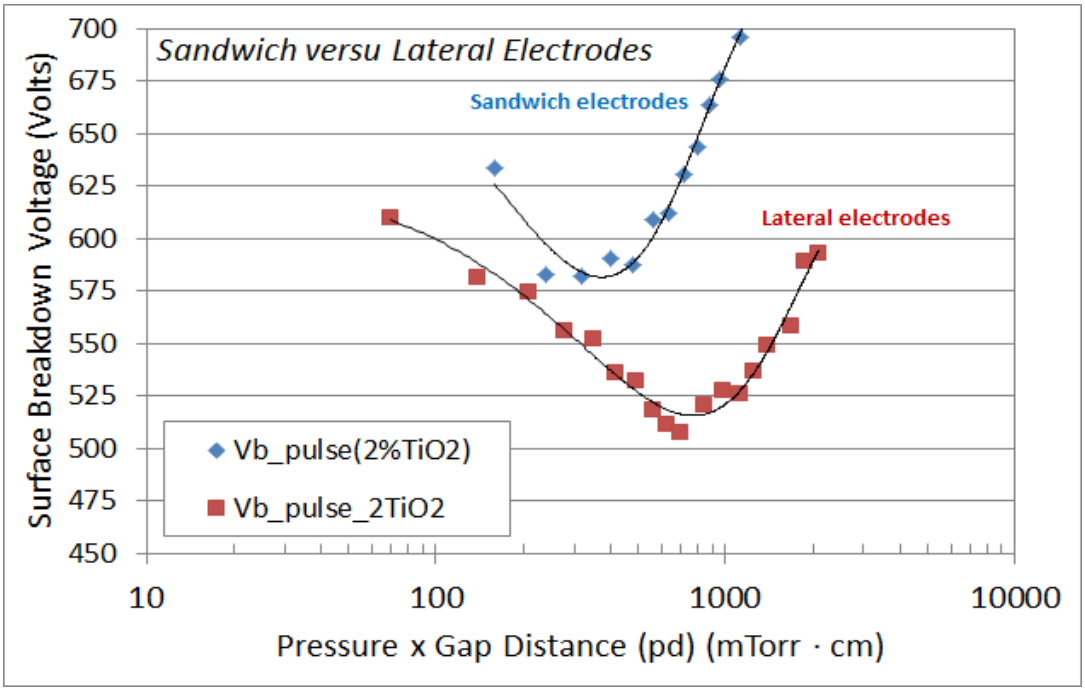

(b)

Fig 3.11 Pulsed surface breakdown curves for both the sandwiched and lateral configuration of (a) control sample (b) S-T2 sample

Table 3.3 *((pd),V_{min})* comparison between sandwiched & lateral electrode configurations

Samples	dc		pulse	
	Sandwiched	Lateral	Sandwiched	Lateral
CS	(650,525 V)	(500, 540 V)	(350, 570 V)	(550, 514 V)
S-A2	(400,535 V)	(650, 550 V)	(400, 570 V)	(700, 565 V)
S-A6	(450, 605 V)	(650, 525 V)	(500, 595 V)	(500, 540 V)
S-T2	(500, 555 V)	(600, 525 V)	(350, 580 V)	(650, 500 V)
S-T6	(470, 526 V)	(550, 480 V)	(400, 560 V)	(500, 520 V)

(Unit: *pd* - mTorr cm)

Table 3.4 Breakdown voltages comparison between sandwiched & lateral electrode configurations at *pd* of 1200 and 300 mTorr cm

Voltage Types	Samples	*pd*=1200 mTorr cm			*pd*=300 mTorr cm		
		Sandwiched	Lateral	ΔV_b	Sandwiched	Lateral	ΔV_b
dc	CS	580 V	560 V	20 V	610 V	570 V	40 V
	S-A2	640 V	560 V	80 V	540 V	570 V	**-30** V
	S-A6	725 V	550 V	175 V	640 V	590 V	50 V
	S-T2	800 V	555 V	245 V	590 V	580 V	10 V
	S-T6	630 V	515 V	115 V	560 V	520 V	40 V
pulse	CS	700 V	540 V	160 V	570 V	540 V	30 V
	S-A2	635 V	590 V	45 V	585 V	575 V	10 V
	S-A6	705 V	565 V	140 V	605 V	560 V	45 V
	S-T2	740 V	525 V	215 V	580 V	555 V	25 V
	S-T6	720 V	540 V	180 V	570 V	530 V	40 V

3.6 Breakdown Voltage versus Varying Pulse Parameters

The pulsed surface breakdown is affected by the pulse parameters, such as pulse frequency and duty cycle. In our experiment, unipolar pulsed electric field is employed, that is, the electric field between the electrodes varies between 'on' and 'off' state. Therefore the electrical charges around the dielectrics and electrodes will be accelerated and drifting alternatively till the surface breakdown events occurred. The period and duty cycle are two major parameters of pulses, determining the movements of the electrical charges in the

electrodes gap. Therefore we also conducted experiments with varying frequency at fixed pressure and duty cycle and varying duty cycle at fixed pressure and frequency.

3.6.1 Breakdown Voltage versus Frequency

The surface breakdown voltages of the samples under varying pulse frequency are investigated in the experiment. In order to see the frequency effects on breakdown voltages, we fixed the pressure in the chamber at 300 mTorr for sandwiched electrode configuration and 900 mTorr for lateral configuration which are both approximately where the minimum breakdown occurs, and the pulse duty cycle to be 50%. Then the pulse frequency is varied from 15 kHz to 220 kHz and data is recorded as outlined in Chapter 3.3. Appendix E are the plots for the surface flashover voltages of all samples as a function of pulse frequency. Figure 3.12 is the typical surface breakdown voltage as a function of frequency for the sandwiched and lateral electrode configurations. As seen, the surface breakdown voltage decreases at first and then maintains in a stable value as the frequency increases. The voltage drop is around 100 V in the sandwiched electrode configuration and about 50 V in the lateral case. This data is in agreement with the literature data where breakdown voltage of solids and gaseous media decrease as frequency increases [13]. We can speculate that for the surface flashover case under unipolar pulsed voltages, the relationship between breakdown voltage and pulse frequency is the same. Generally in high frequency ranges, more ionization collisions are caused by electrons, leading to the lower surface breakdown voltage.

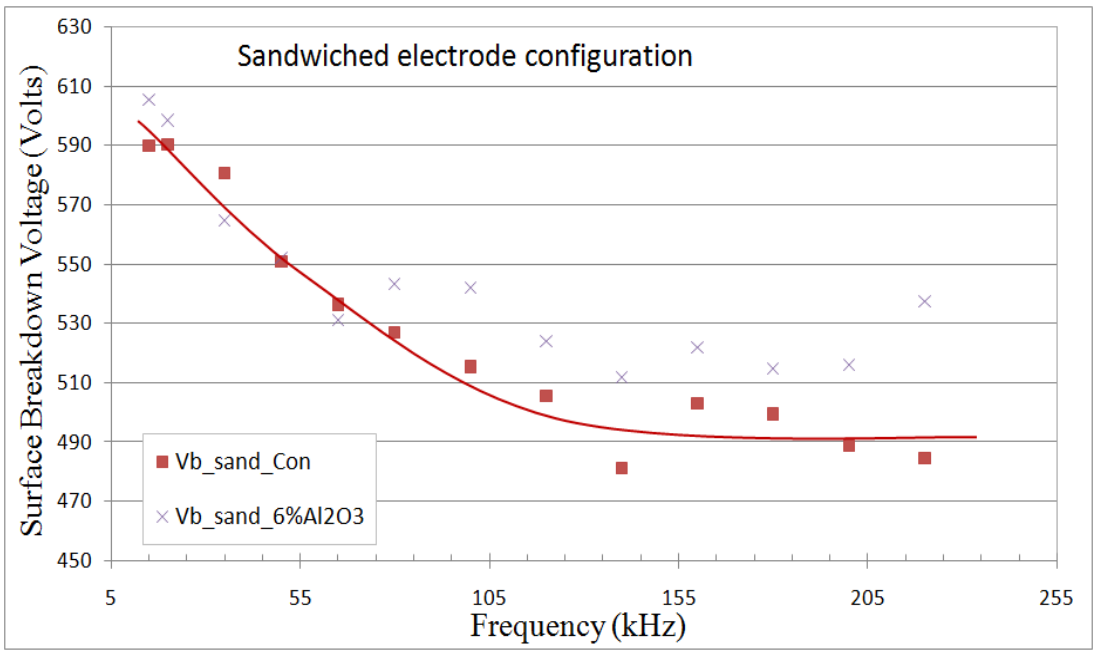

(a)

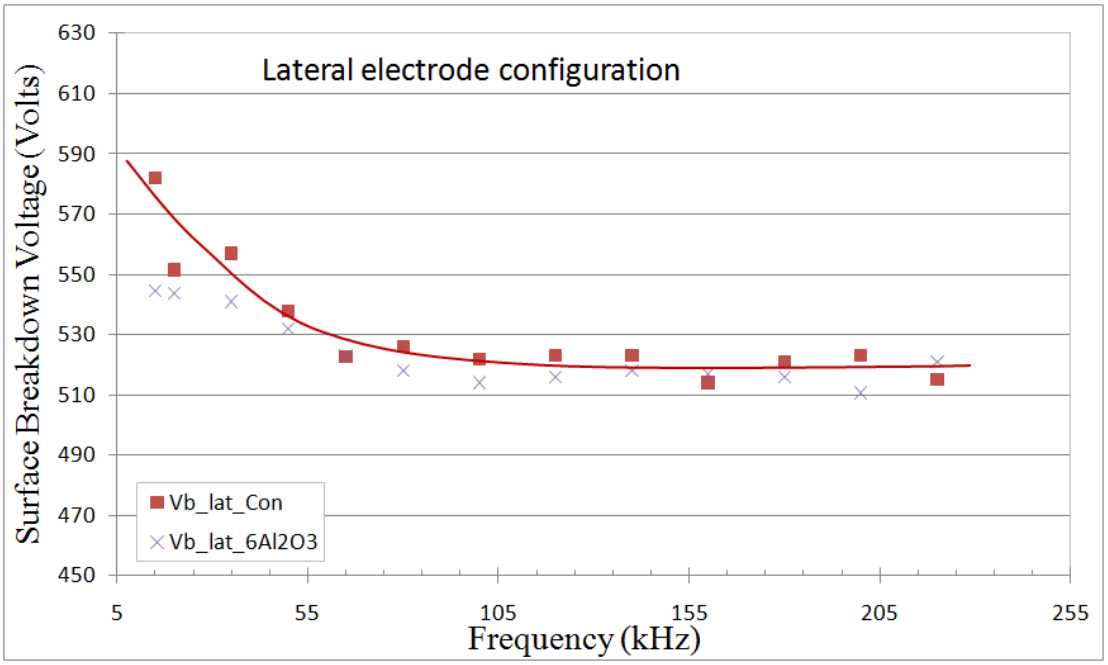

(b)

Figure 3.12 Typical schematics of surface breakdown voltage as a function of frequency for (a) sandwiched (b) lateral configuration

3.6.2 Breakdown Voltage versus Duty Cycle

The breakdown voltages of the samples under varying duty cycle are also measured. In order to see the duty cycle effects on breakdown voltages, we fixed the pressure in the chamber at 300 mTorr for sandwiched electrode configuration and 900 mTorr for lateral configuration and pulse frequency of 20 kHz. Then the pulse duty cycle is varied from 10% to 90% in a step of 10% and data is recorded as illustrated in Chapter 3.3. Appendix F is the plots for the surface flashover voltages of the samples as a function of pulse duty cycle. As seen, the variation of duty cycle plays a greater effect in the surface breakdown voltages for sandwiched configuration compared with lateral setup. Meanwhile, the surface breakdown voltage for sandwiched configuration is generally higher than the lateral one. However, it is hard to get a consistent conclusion on the effects of duty cycle played on the surface breakdown voltage because of the limited data points at this time.

3.7 Surface Effect on Breakdown Voltage

The surface effects on surface breakdown voltage are investigated. The top surface of the samples are machined as describe in Chapter 3.1. Lateral electrode configuration as shown in Figure 3.2a is employed in this study. All of the experiment sets including the pressure sweep, frequency sweep, and duty cycle sweep are conducted. The experimental procedure is the same as stated in Chapter 3.3. Although the electrodes spacing is 0.7 cm, the discharge path across the surface of the sample in this case is approximately 0.9 cm because of the saw-shaped surface. In order to observe the surface effect on the breakdown voltage, the surface breakdown voltage as a function of the product of the pressure and the gap distance (*pd*) is plotted.

Figure 3.13 shows the comparison of the surface breakdown curves for the untreated and machined surface under lateral electrode configuration. It is clearly that the *pd* value at which the breakdown voltage reaches the minimum is about 500-600 mTorr cm, demonstrating that the surface flashover occurred across the sample surface. The minimum surface breakdown voltage for untreated surface is 540 V and 520 V for the machined surface in Figure 3.12 (a). Table 3.5 gives the specific differences of $((pd), V_{min})$ for the untreated surface samples and machined surface samples. There is only a minor shift between the breakdown curves for the samples with different surface conditions, which is very consistent with the Paschen's law.

Furthermore, we also observed that the surface breakdown voltage for the untreated surface, whether DC or pulsed field, is generally higher than the machined surface except for the sample S-T6 (the 6% TiO_2 filled). Table 3.6 is the comparison of the breakdown voltages between the untreated and machined surface samples at *pd* of 1000 mTorr cm and 400 mTorr cm. The difference of the breakdown voltages ranges from 0 to 80 V. However, it is expected since the machined surface is very coarse compared with the untreated surface and the electric field and ionization will be enhanced around the protrusions and voids, and the space charges may accumulate in the machined channels beyond the sample surface between the electrodes, both of which lead to the surface breakdown at lower voltage.

Finally, as shown in Appendix F, the behavior of surface breakdown voltage as a function of frequency for untreated and machined surface samples is very similar. The breakdown voltage decreases first and then maintains at a stable value in the higher frequency range.

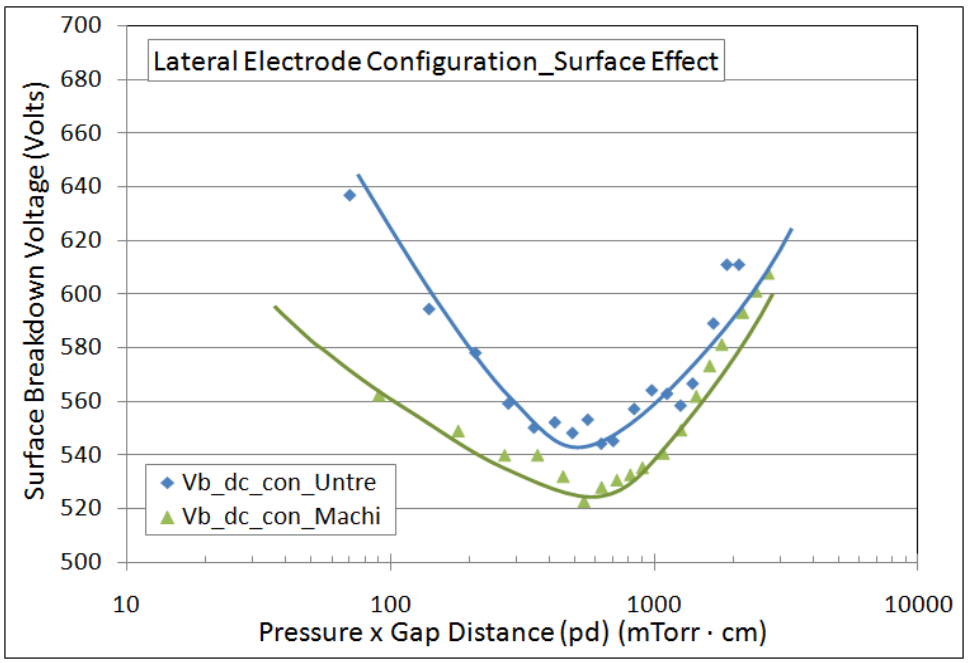

(a)

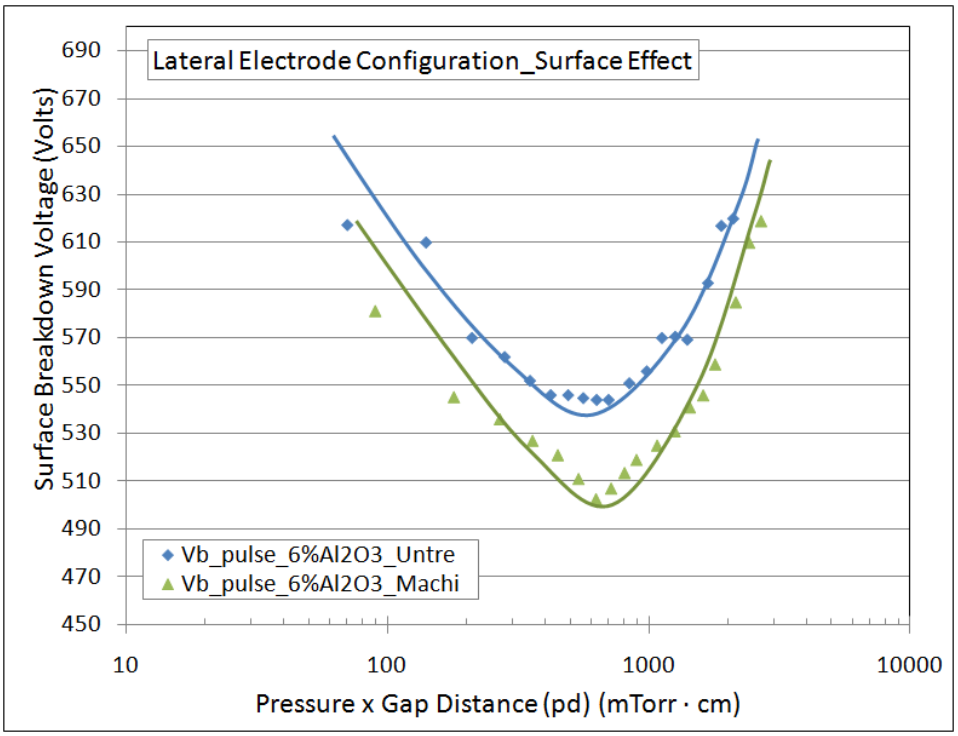

(b)

Figure 3.13 Typical surface breakdown curves for untreated and machined surface of (a) control sample (b) S-A6 sample

Table 3.5 *((pd),V_{min})* comparison between untreated and machined surface samples

Samples	dc		pulse	
	Untreated	Machined	Untreated	Machined
CS	(500, 540 V)	(600, 524 V)	(550, 514 V)	(650, 520 V)
S-A2	(650, 550 V)	(700, 532 V)	(700, 565 V)	(700, 464 V)
S-A6	(650, 525 V)	(700, 524 V)	(500, 540 V)	(600, 500 V)
S-T2	(600, 525 V)	(650, 530 V)	(650, 500 V)	(650, 504 V)
S-T6	(550, 480 V)	(650, 520 V)	(500, 520 V)	(600, 504 V)

(Unit: *pd* - mTorr ·cm)

Table 3.6 Breakdown voltages comparison between untreated and machined surface samples at *pd* of 1000 and 400 mTorr ·cm

Voltage Types	Samples	*pd*=1000 mTorr ·cm			*pd*=400 mTorr ·cm		
		Untreated	Machined	ΔV_b	Untreated	Machined	ΔV_b
dc	CS	560 V	540 V	20 V	547 V	528 V	19 V
	S-A2	554 V	515 V	39 V	564 V	528 V	36 V
	S-A6	540 V	526 V	14 V	562 V	544 V	18 V
	S-T2	555 V	540 V	15 V	556 V	540 V	16 V
	S-T6	505 V	525 V	**-20** V	492 V	540 V	**-48** V
pulse	CS	536 V	528 V	8 V	530 V	530 V	0 V
	S-A2	575 V	495 V	80 V	575 V	505 V	70 V
	S-A6	556 V	514 V	42 V	546 V	516 V	30 V
	S-T2	520 V	516 V	4 V	535 V	520 V	15 V
	S-T6	530 V	512 V	18 V	526 V	514 V	12 V

3.8 Conclusions

This study experimentally confirms that nanoscale powder additives play an effect on the surface flashover of the dielectrics in the partial vacuum of nitrogen gas under either DC or pulsed electric field. For different samples, the DC and pulsed surface breakdown curves under different electrode architectures resemble the well-known Paschen curve. Although the difference is small, the dc surface breakdown generally seems to be slightly higher than the pulsed case. For different nano-particles, there might be a different critical loading ratio in improving the insulation properties of dielectric materials.

The surface breakdown voltage depends on the test electrode configurations. In most cases, sandwiched electrode configuration exhibits better surface flashover characteristics than the lateral electrode configuration. In the normalized surface flashover breakdown curves, there is usually a *pd* shift under sandwiched and lateral electrode architectures.

Furthermore, the breakdown voltage is a function of the pulse frequency. In all of the samples, the surface breakdown voltages decrease first and then are maintained in a stable value as the frequency increases. For duty cycle sweep test, the variations in breakdown voltage for sandwiched configuration are greater than that for the lateral case.

In addition, the surface condition of the dielectric samples also affects both the discharge path of surface flashover and the surface breakdown voltage. The surface flashover always bridges the electrodes across the surface of the samples in partial vacuum environment. Meanwhile, as expected, because of the roughness of the machined surface, the breakdown voltage for theses samples is relatively lower than that for untreated surface samples. All of the discoveries in this work shed light on the further understanding of the surface flashover phenomena in partial vacuum.

CHAPTER IV

CONCLUSIONS

In this theis, two major parts related to pulsed breakdown phenomena have been studied and presented, namely, pulse generators including an application, and surface flashover in partial vacuum under pulsed applied field.

The voltage-regulated 1 kV pulse generator based on a simple RC circuit is designed and developed in the lab in order to trigger the CNTs cold cathode. The pulse generator is capable of providing a maximum output of a negative 1kV pulse. The simulation results including output voltage and delay time are a good match with those of in-house constructed pulse generator. The CNTs initiated hollow cathode discharge is achieved with this pulse generator. The negative pulse from the pulse generator applied to CNTs generated sufficient field emitted electrons to trigger a breakdown in plasma chamber. Finally the hollow cathode discharge in helium is initiated. As it is a promising and practical trigger method for pseudospark switches, the delay time of the switch is investigated in our work. Randomly oriented CNTs samples are proven to be a very good trigger material to initiate the hollow cathode breakdown in helium. It has a very small delay time of several microseconds with relatively low trigger voltage levels of several hundred volts. The delay time of the CNTs samples decreases with the trigger voltage increasing. CNTs samples with longer growth time have relatively lower delay time in the experiments compared with samples with shorter growth time. The excellent field emission

property and low turn-on electric field enable the CNTs samples to be an effective and efficient cold cathode trigger material.

As the second part of this thesis work, an attempt was also made to better understand the surface flashover phenomena of nanodielctrics in partial vacuum. Most of the experimental conditions including samples, electrode configurations, surface conditions, and applied pulse parameters are taken into consideration in our work. This study confirms that nanoscale powder additives influence the surface flashover phenomena of the dielectrics in the partial vacuum of nitrogen gas under either DC or pulsed electric field. The DC and pulsed surface breakdown curves under different electrode architectures for different samples resemble the well-known Paschen curve. Although the difference is small, the dc surface breakdown normally seems to be slightly higher than the pulsed case. Furthermore, the surface breakdown voltage greatly depends on the test electrode configurations. In most cases, sandwiched electrode configuration exhibits better surface flashover characteristics than the lateral electrode configuration. In the normalized surface flashover breakdown curves, there is usually a *pd* shift under sandwiched and lateral electrode architectures. Moreover, the breakdown voltage is a function of the pulse frequency and pulse duty cycle. Finally, it is also observed that the surface condition of the dielectric samples affects both the discharge path of surface flashover and the surface breakdown voltage. The surface flashover always bridges the electrodes across the surface of the samples in partial vacuum environment. All of the discoveries in this work provide useful information on the further understanding of the surface flashover phenomena in partial vacuum.

References

[1] Abbas Pourzaki, Hossein Mirzaee, "New High Voltage Pulse Generators," Recent Patents on Electrical Engineering, Bentham Science Publishers Ltd, Volume 2, Issue 1, pp.65-76, 2009.

[2] R. Sundararajan, Jin Shao, E. Soundarajan, J. Gonzales, A. Chaney, "Performance of solid-state high-voltage pulsers for biological applications-a preliminary study," Plasma Science, IEEE Transactions on , vol.32, no.5, pp. 2017- 2025, Oct. 2004.

[3] H. Akiyama, T. Sakugawa, T. Namihira, K. Takaki, Y. Minamitani, N. Shimomura, "Industrial Applications of Pulsed Power Technology," Dielectrics and Electrical Insulation, IEEE Transactions on , vol.14, no.5, pp.1051-1064, October 2007.

[4] J. Mankowski, M. Kristiansen, "A review of short pulse generator technology," Plasma Science, IEEE Transactions on , vol.28, no.1, pp.102-108, Feb 2000.

[5] Weihua Jiang, K. Yatsui, K. Takayama, M. Akemoto, E. Nakamura, N. Shimizu, A. Tokuchi, S. Rukin, V. Tarasenko, A. Panchenko, "Compact solid-State switched pulsed power and its applications," Proceedings of the IEEE , vol.92, no.7, pp. 1180- 1196, July 2004.

[6] Hansjoachim Bluhm, Pulsed Power Systems: Principles and Applications, Springer, 2006.

[7] T. M. Bilodeau, W. G. Dunbar, W. J. Sarjeant, "High-voltage and partial discharge testing techniques for space power systems," Electrical Insulation Magazine, IEEE, vol.5, no.2, pp.12-21, March-April 1989.

[8] W. G. Dunbar and J. W. Seabrook, High Voltage Design Guide for Airborne Equipment, U.S. Government Printing Office, 1980.

[9] M. Iwasa, K. Tanaka, S. Sasaki, O. Odawara, "Study of the Plasma Interference With High-Voltage Electrode Array for Space Power Application," Plasma Science, IEEE Transactions on , vol.34, no.5, pp.1997-2003, Oct. 2006.

[10] N. T. Grier, “Plasma interaction experiment II: Laboratory and flight results,” Spacecraft Environmental Interaction Technology—NASACP-2336, pp. 333–347, 1983.

[11] P. Rustan, H. Garrett, M.J. Schor, "High voltages in space: innovation in space insulation," Electrical Insulation, IEEE Transactions on, vol.28, no.5, pp.855-865, Oct 1993.

[12] H. Kirkici, "High Voltage Insulation Space Environment and Design Guideline," Power Modulator Symposium, 2006. Conference Record of the 2006 Twenty-Seventh International, vol., no., pp.33-37, 14-18 May 2006

[13] K. Koppisetty, “Breakdown Studies of Helium and Nitrogen in Partial Vacuum Subject to Non-Uniform, Unipolar Fields in the 20-220 KHz Range”, Ph.D. dissertation, Auburn University, pp. 116-118, 2008.

[14] M. Lipham, “Electrical Breakdown Studies of Partial Pressure Argon Under kHz Range Pulse Voltages”, Master thesis, Auburn University, pp.53-54, 2010.

[15] Y. Cao, P.C. Irwin, K. Younsi, "The future of nanodielectrics in the electrical power industry," Dielectrics and Electrical Insulation, IEEE Transactions on , vol.11, no.5, pp. 797- 807, Oct. 2004

[16] H. C. Miller, "Flashover of insulators in vacuum: review of the phenomena and techniques to improved holdoff voltage," IEEE Transactions on Electrical Insulation, vol.28, no.4, pp.512-527, Aug 1993.

[17] B. D. Green, G. Caledonia, D. Wilkerson, "The Shuttle Environment: Gases, Particulates, and Glow," Journal of Spacecraft and Rockets, Vol. 22, pp.500-511, 1985.

[18] C. L. Wadhwa, *High Voltage Engineering*, New Age International (P) Limited, Publishers, 2007.

[19] M. Abdel-Salam, High-Voltage Engineering: Theory and Practice, Second Edition, Revised and Expanded, Marcel Dekker, 2000.

[20] A. A. Fridman, L. A. Kennedy, *Plasma physics and engineering*, Taylor & Francis, pp 453, 2004.

[21] E. Hastings, G. Weyl, Guy, D. Kaufman, "Threshold voltage for arcing on negatively biased solar arrays", Journal of Spacecraft and Rockets, vol. 27, pp 539-544, 1990.

[22] K. Koppisetty, H. Kirkici, D. L. Schweickart, "Breakdown Characteristics of Nitrogen under Unipolar Applied Voltages for Non-Uniform Field Configuration," IEEE International Power Modulators and High Voltage Conference, Proceedings of the 2008 , vol., no., pp.544-547, 27-31 May 2008

[23] A. Bogaerts, "The glow dischrage: an exciting plasma," Journal of Analytical Atomic Spectrometry, vol. 14, pp. 1375-1384, 1999.

[24] G. Stockhausen and M. Kock, "Proof and analysis of the pendulum motion of beam electrons in a hollow cathode discharge," Journal of Physics D: Applied Physics, vol. 34, pp. 1683-1689, 2001.

[25] G. Schaefer and K. H. Schoenbach, "Basic Mechanisms Contributing to the Hollow Cathode Effect," in Physics and Applications of Pseudosparks. vol. 219, M. A. Gundersen and G. Schaefer, Eds. New York: PlenumPress, 1990.

[26] H. Kirkici and D. Bruno, "Operating characteristics of a segmented hollow cathode over a wide pressure range," Plasma Science, IEEE Transactions on, vol. 23, pp. 229-234, 1995.

[27] Haitao Zhao, “Design and Construction of Carbon NanoTubes (CNTs) Triggered Pseudospark Switch”, Ph.D. dissertation, Auburn University, 2012.

[28] T. Mehr, H. Arenz, P. Bickel, J. Christiansen, K. Frank, A. Gortler, F. Heine, D. Hofmann, R. Kowalewicz,; M. Schlaug, R. Tkotz, "Trigger devices for pseudospark switches," Plasma Science, IEEE Transactions on , vol.23, no.3, pp.324-329, Jun 1995

[29] R. Hawley, “Solid Insulators in Vacuum, A Review”, Vacuum, Vol. 18, pp. 383-90,1968.

[30] J. D. Cross, “The Mechanism of Flashover across Solid Insulators in Vacuum”, Proc. VII Int. Symp. Disch. Elect. Insul. Vac., pp. 24-37, Novosibirsk, 1976.

[31] R. Latham, *High voltage vacuum insulation: Basic concepts and technological practice*, Academic Press, pp8-11, pp 300-306, 1995.

[32] E. Kuffel, W. S. Zaengl, and J. Kuffel, High Voltage Engineering: Fundamentals, Second edition, Newnes, 2000.

[33] M. Serkan, H. Kirkici, K. Koppisetty, "Surface Flashover Characteristics of Nano-Composite Dielectric Materials Under DC and Pulsed Signals in Partial Vacuum," Power Modulator Symposium, 2006. Conference Record of the 2006 Twenty-Seventh International, vol., no., pp.90-92, 14-18 May 2006

[34] R. N. Schouten, High-Voltage Power Pulse Circuit, Electronic Design, pp. 147, December 1, 1997.

Appendix A SPICE Listing for Pulse Generator Circuit

The list of circuit file of the pulse generator for LTSpice simulation is attached as following.

Netlist:

```
* 1 kV Pulse Generator Design
XIC1 16 0 22 0 15 4N25
R16 16 17 200
D2 0 16 1N4148
R18 0 15 10MEG
R17 26 22 5.6k
C6 26 0 100n
V1 17 0 PULSE(0 5 10m 1n 1n 20m)
C4 26 0 4.7µ
C5 26 0 0.1µ
V2 26 0 12
V3 0 24 5
R8 1 6 2k
R9 6 5 2k
R10 5 4 2k
R22 4 0 10meg
V5 4 0 400
R1 0 3 0.1
C2 1 9 10n
R5 9 8 33
R6 8 7 33
R7 7 0 33
C9 1 Vout1 1µ
D1 Vout1 0 DMOD
.MODEL DMOD D (IS=2.2E-15 BV=1000V TT=0)
R2 Vout2 0 0.02
R11 Vout1 10 330
R12 10 11 330
R13 11 12 330
R14 12 0 2.2
R3 Vout2 13 4.7k
C3 13 0 22n
RL Vout1 Vout2 1e11
.model D D
.lib C:\PROGRA~2\LTC\LTSPIC~1\lib\cmp\standard.dio
XIC2 22 27 26 24 TC4426_I2D_B
.SUBCKT TC4426_I2D_B 1 2 3 4
* Input Impedance/Clamp
```

```
R1  4    1    100MEG
C1  4    1    12.0P
G3  3    1    TABLE { V(3, 1) } ((-770M,-1.00)(-700M,-10.0M)(-630M,-
1.00N)(0,0)(20.0,1.00N))
G4  1    4    TABLE { V(1, 4) } ((-5.94,-1.00)(-5.4,-10.0M)(-4.86,-
1.00N)(0,0)(20.0,1.00N))
* Threshold
G11 0    30   TABLE { V(1, 11) } ( (-1m,10n)(0,0)(0.78,-.1)(1.25,-1)(2,-1) )
G12 0    30   TABLE {V(1,12)} ( (-2,1)(-1.2,1)(-0.6,.1)(0,0)(1,-10n))
G21 0    11   TABLE { V(3, 4) }
((0,1.35)(4.00,1.35)(6.00,1.5)(10.0,1.48)(13.0,1.49)(16.0,1.5))
G22 0    12   TABLE { V(3, 4) }
((0,1.35)(4.00,1.16)(6.00,1.25)(10.0,1.24)(13.0,1.24)(16.0,1.25))
R21 0    11   1 TC 504U  2.33U
R22 0    12   1 TC 231U  -103N
C30 30   0    1n
* HL Circuit
G31 0    31   TABLE { V(3, 4) }
((0,146)(4.0,63.3)(6.00,43.4)(10.0,34.8)(14.0,32.6)(18.0,28.4))
R31 31   0    1 TC 1.93M  -1.89U
G33 0    30   TABLE { V(31, 30) } ( (-1M,-10)(0,0)(1,10N) )
S31 31   30 31 30 SS31
* LH Circuit
G32 32   0    TABLE { V(3, 4) }
((0,104)(4.0,36.8)(6.00,19.7)(10.0,12.1)(14.0,10.2)(18.0,9.5))
R32 0    32   1 TC 2.26M  2.88U
G34 30   0    TABLE { V(30, 32) } ( (-1M,-10)(0,0)(1,10N) )
R30 32   30   1MEG
* DRIVE
G51 0    50   TABLE { V(30, 0) } ( (-5,-1U)(-3,-1U)(0,0)(6,1.00)(18,1.020) )
G52 50   0    TABLE { V(0, 30) } ( (-5,-1U)(-3,-1U)(0,0)(6,1.20)(18,1.220) )
R53 0    50   1
G50 51   60   VALUE {V(50,0)*300M/(-700M+18/(V(3,4) + 1M))}
R51 51    0   1
G53  3    0   TABLE {V(51,0)} ((-100,100)(0,0)(1,1n))
G54  0    4   TABLE {V(0,51)} ((-100,100)(0,0)(1,1n))
R60 0    60   100MEG
H67 0    69   V67 1
V67 60   59   0V
C60 561  60   200P
R59 59   2    8.19
L59 59   2    10.0N
* Shoot-through adjustment
VC60 56 0 0V
RC60 56 561 1m
H60 58 0 VC60 56
G60P 0 3 TABLE { V(58, 0) } ((-1,-1u)(0,0)(25,10.0m)(40,0))
G60N 4 0 TABLE { V(0, 58) } ((-1,-1u)(0,0)(25,10.0m)(40,0))
* Source Output
E67 67   0    TABLE { V(69, 0) } ( (-1.3,-1.3)(0,0)(1,2.00) )
G63 0    63   POLY(1) 3 4 22.9 -1.86 54.4M
R63 0    63   1 TC 4.29M 11.7U
E61 61   65   VALUE {V(67,0)*V(63,0)}
V63 65   3    100U
G61 61   60   TABLE { V(61, 60) } (-20.0M,-130)(-15.0M,-65.0)(-10.0M,-
13.0)(0,0)(10,1N))
* Sink Output
```

```
E68 68   0    TABLE { V(69, 0) }  ( (-1,-2.00)(0,0)(1.5,1.5) )
G64 0    64   POLY(1) 3 4 22.9 -1.86 54.4M
R64 0    64   1 TC 4.29M 11.7U
E62 62   66   VALUE {V(68,0)*V(64,0)}
V64 66   4    100U
G62 60   62   TABLE { V(60, 62) } (-20.0M,-150)(-15.0M,-75.0)(-10.0M,-
15.0)(0,0)(10,1N))
* Bias Current
G55 0    55   TABLE { V(3, 4) }
((0,0)(4.5,530U)(10.0,770U)(14.0,910U)(18.0,1.38M))
G56 3    4    55 0 1
R55 55   0    1 TC  -1.53M -407N
G57 0    57   TABLE { V(3, 4) }
((0,0)(4.5,70.0U)(10.0,80.0U)(14.0,90.0U)(18.0,120U))
G58 3    4    57 0 1
R57 57   0    1 TC  -1.53M -407N
S59 55   0    1 0 SS59
* Models
.MODEL SS59 VSWITCH Roff=1m Ron=100Meg Voff=1.2V Von=1.5V
.MODEL SS31 VSWITCH Roff=100MEG Ron=800 Voff=0.2V Von=0.1V
.ENDS TC4426_I2D_B
XMOS 1 27 3 102N21A
.SUBCKT 102N21A   10 20 30
*  TERMINALS:  D  G  S
*  1000 Volt  21 Amp  0.52 ohm  N-Channel Power MOSFET
*  REV.A  01-09-02
M1   1  2  3  3  DMOS L=1U W=1U
RON   5  6  0.3
DON   6  2  D1
ROF   5  7 .1
DOF   2  7  D1
D1CRS 2  8  D2
D2CRS 1  8  D2
CGS   2  3  5.5N
RD    4  1  0.5
DCOS  3  1  D3
RDS   1  3  5.0MEG
LS    3  30 .5N
LD   10  4  1N
LG   20  5  1N
.MODEL DMOS NMOS (LEVEL=3 VTO=3.0 KP=3.8)
.MODEL D1 D (IS=.5F CJO=1P BV=100 M=.5 VJ=.6 TT=1N)
.MODEL D2 D (IS=.5F CJO=400P BV=1000 M=.4 VJ=.6 TT=400N RS=10M)
.MODEL D3 D (IS=.5F CJO=900P BV=1000 M=.3 VJ=.4 TT=400N RS=10M)
.ENDS 102N21A
.lib 4N25.sub
.tran 0 50m 0 1u
.backanno
.end
```

Appendix B Surface Breakdown Voltages vs. Pressure (Sandwiched Electrode)

Complete set of figures for every test set, the surface flashover breakdown voltages are plotted as the function of pressure for the sandwiched configuration. For one test set plot, DC and unipolar pulse signal (20 kHz, 50% duty cycle) breakdown voltages are compared.

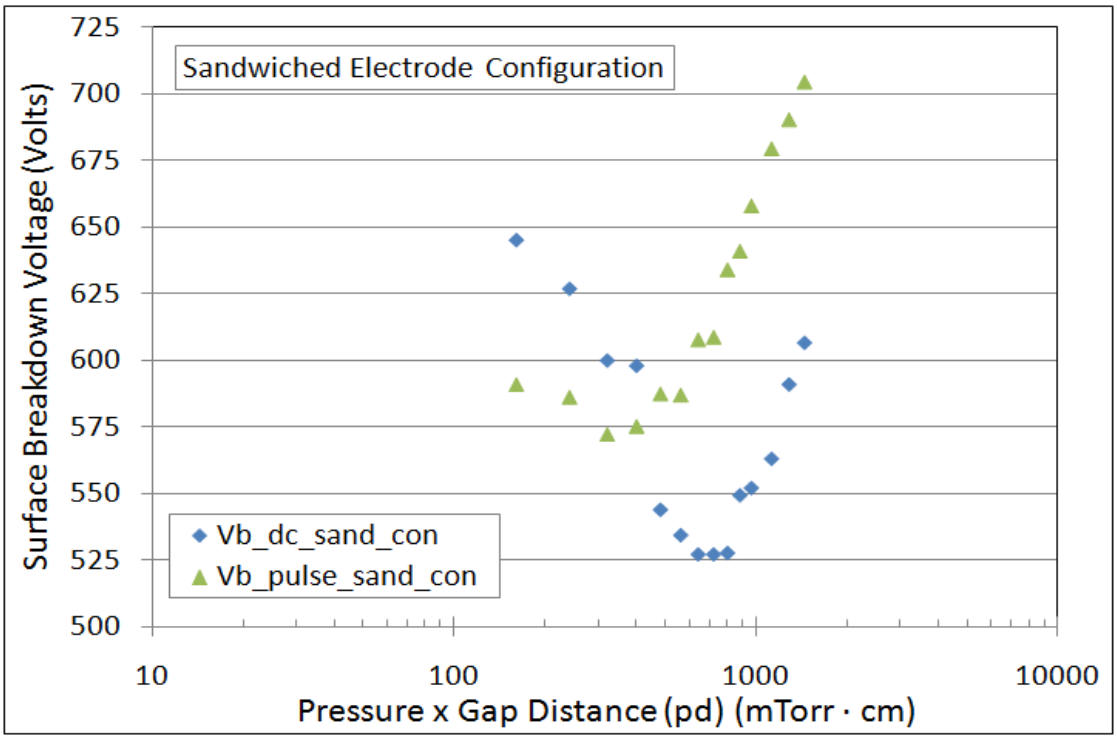

Figure B-1

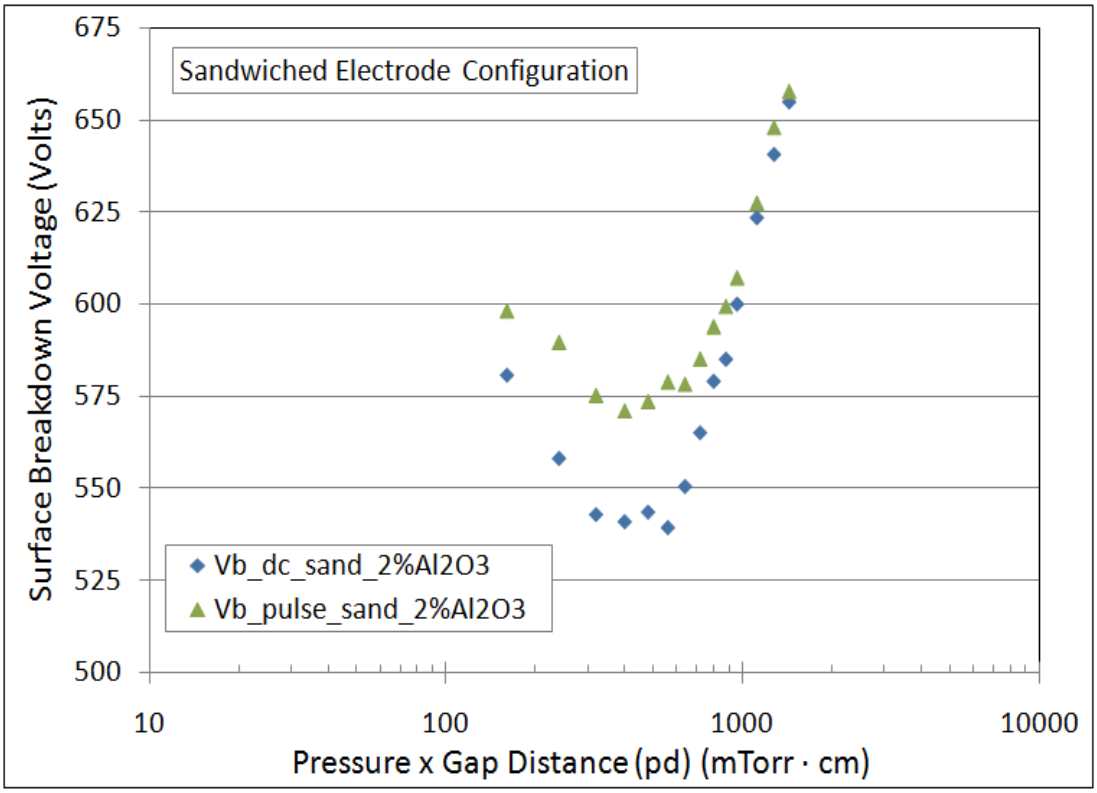

Figure B-2

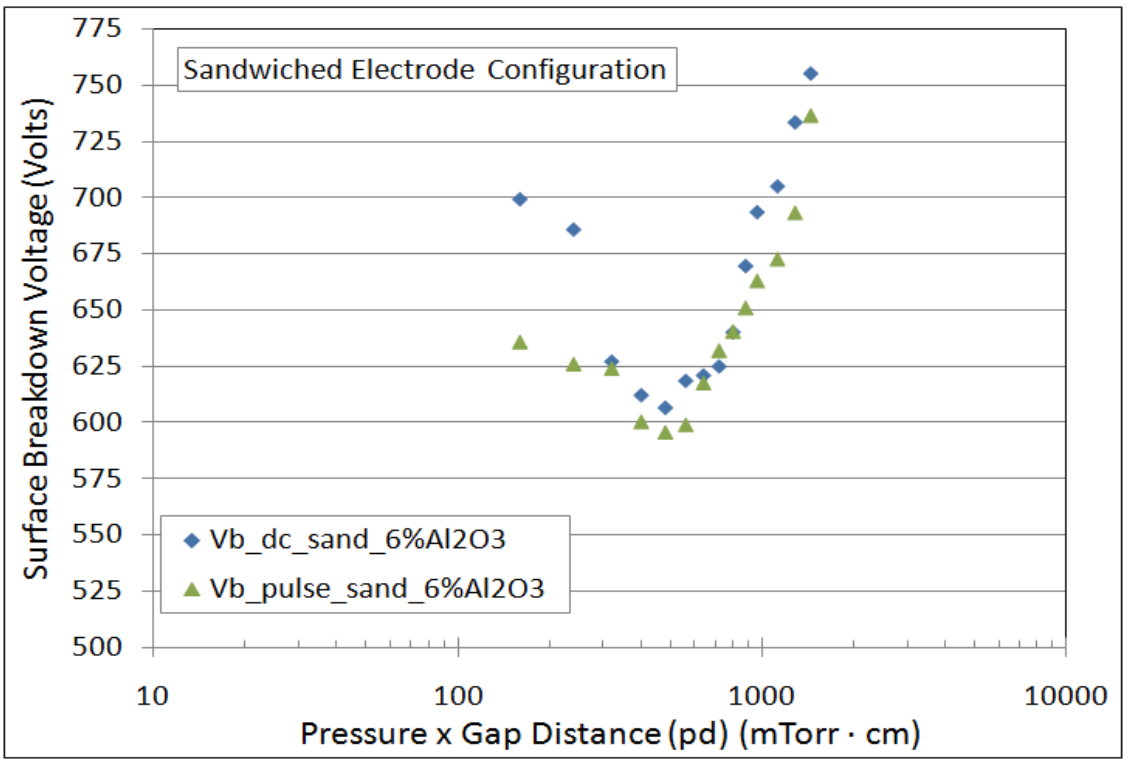

Figure B-3

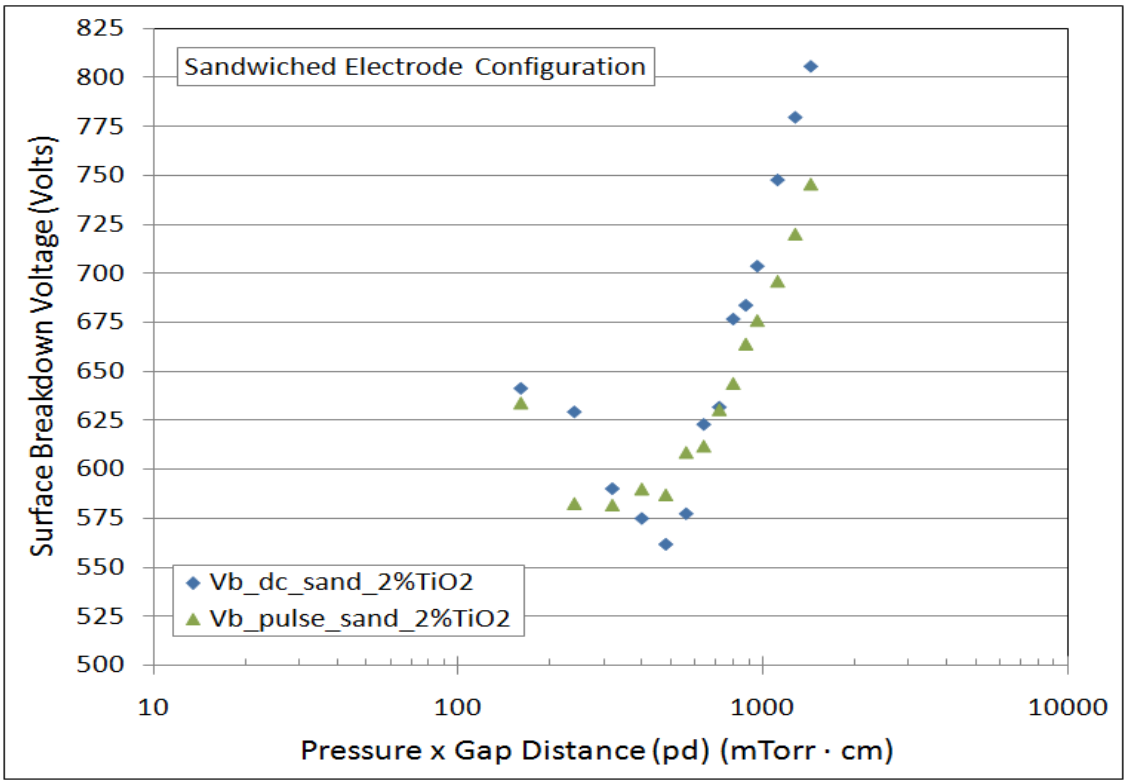

Figure B-4

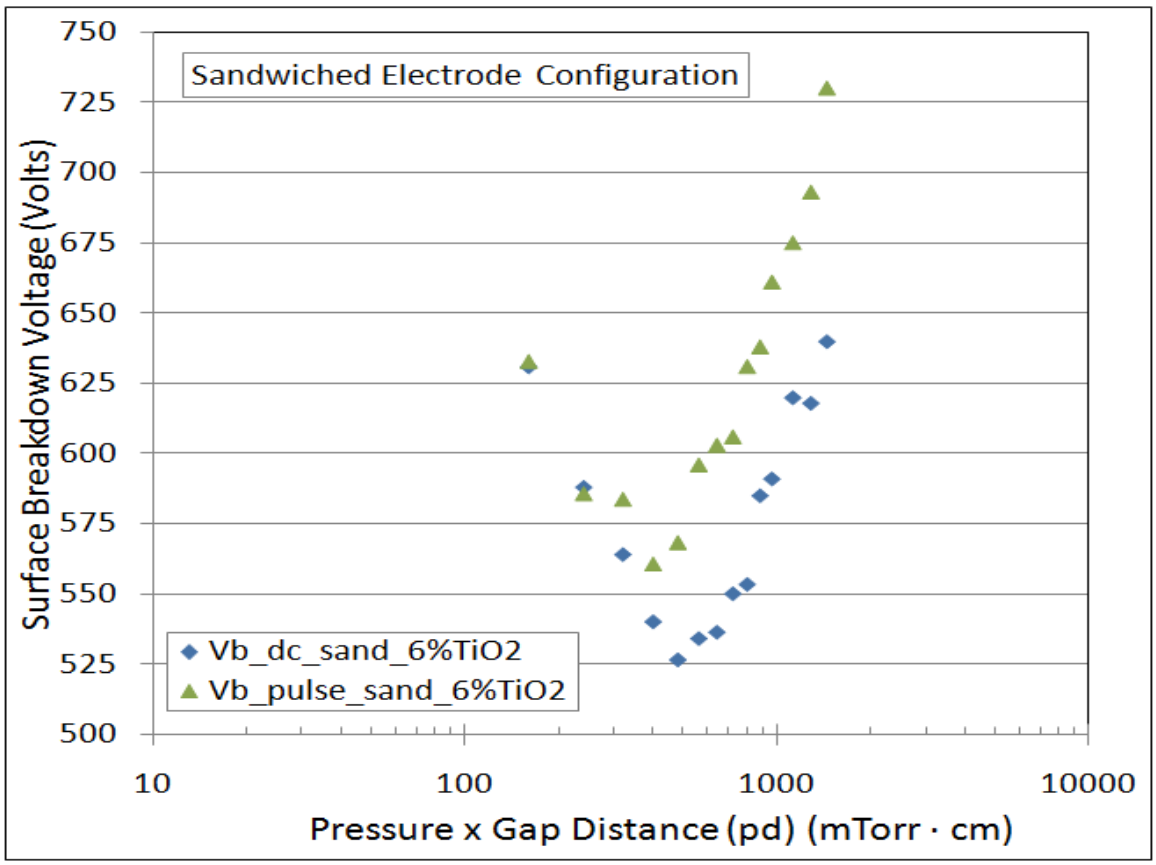
Sandwiched Electrode Configuration
Surface Breakdown Voltage (Volts)
750
725
700
675
650
625
600
575
550
525
500
10
100
1000
10000
Pressure x Gap Distance (pd) (mTorr · cm)
Vb_dc_sand_6%TiO2
Vb_pulse_sand_6%TiO2

Figure B-5

Appendix C Surface Breakdown Voltages vs. Pressure (Lateral Electrode)

Complete set of figures for every test set, the surface flashover breakdown voltages are plotted as the function of pressure for the untreated surface samples under the lateral configuration. For one test set plot, DC and unipolar pulse signal (20 kHz, 50% duty cycle) breakdown voltages are compared.

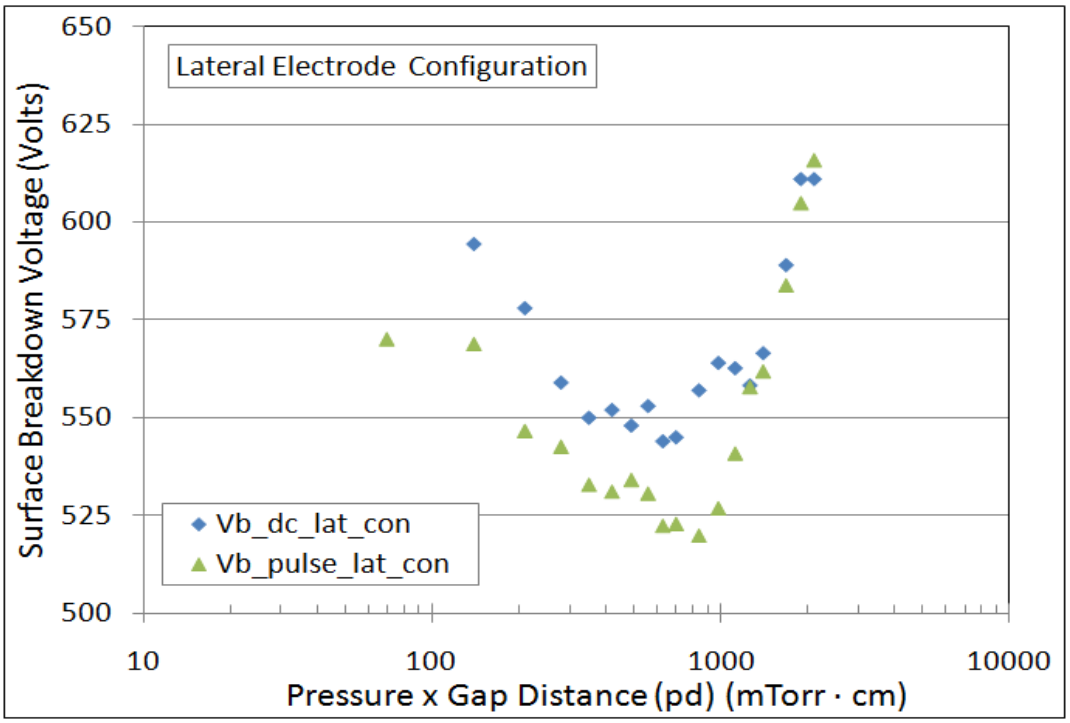

Figure C-1

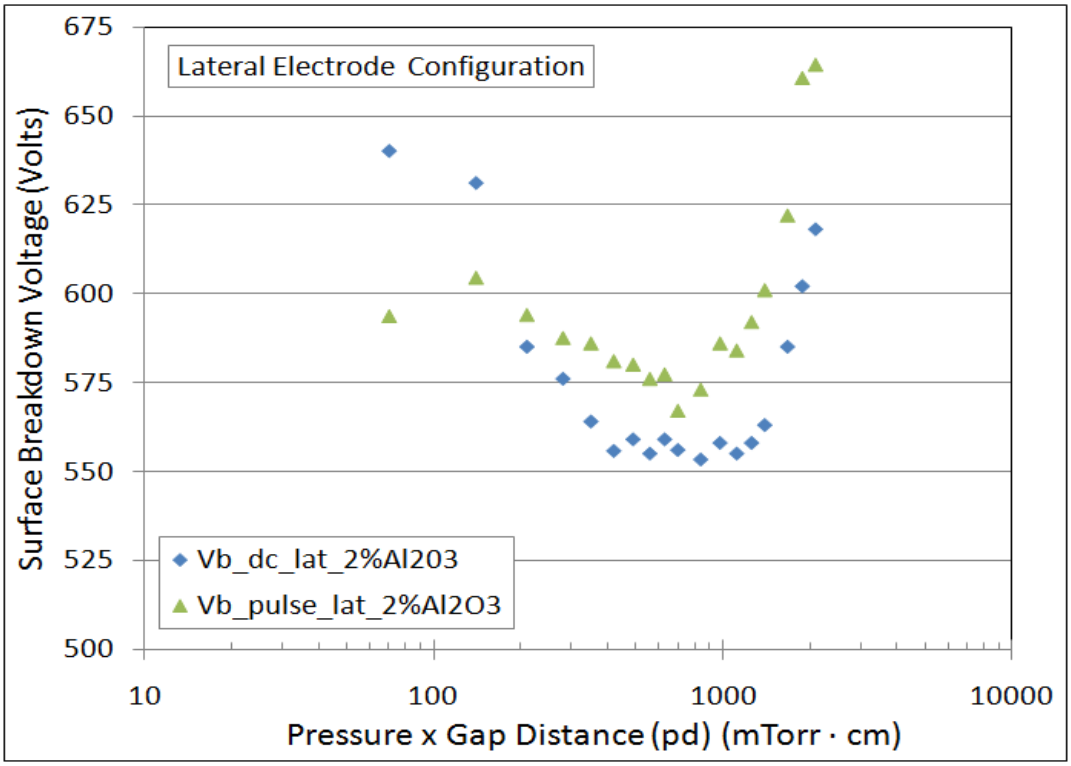

Figure C-2

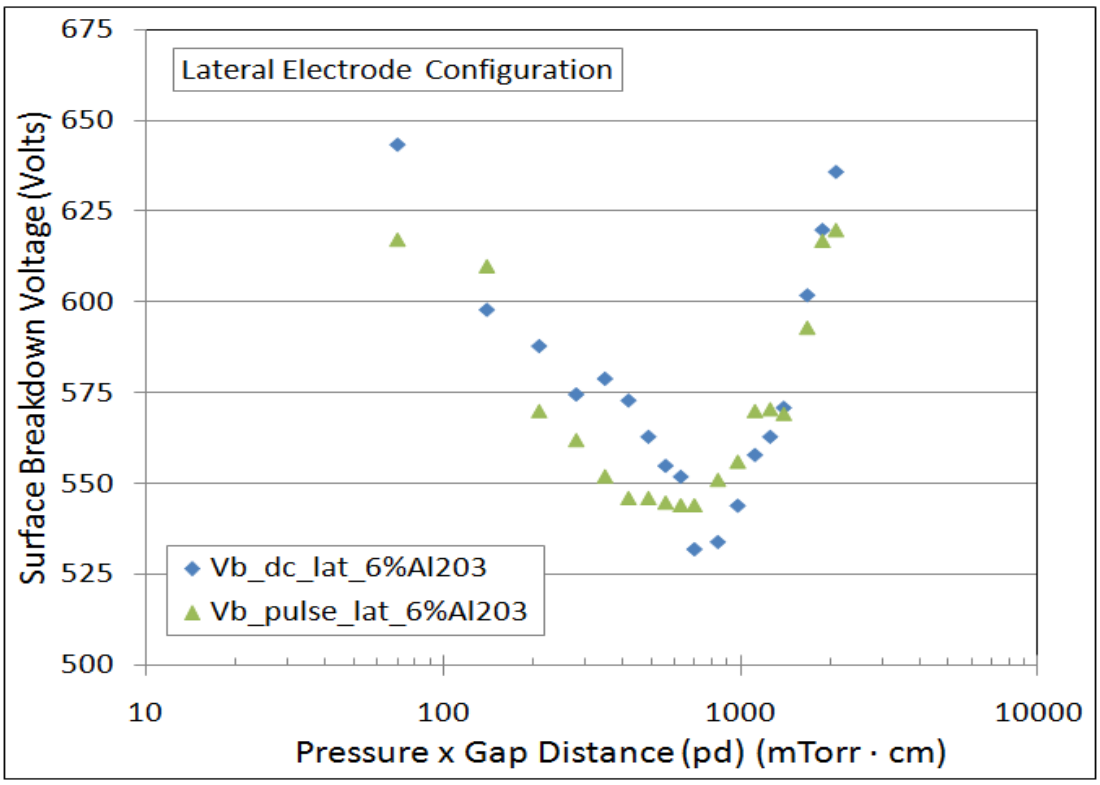

Figure C-3

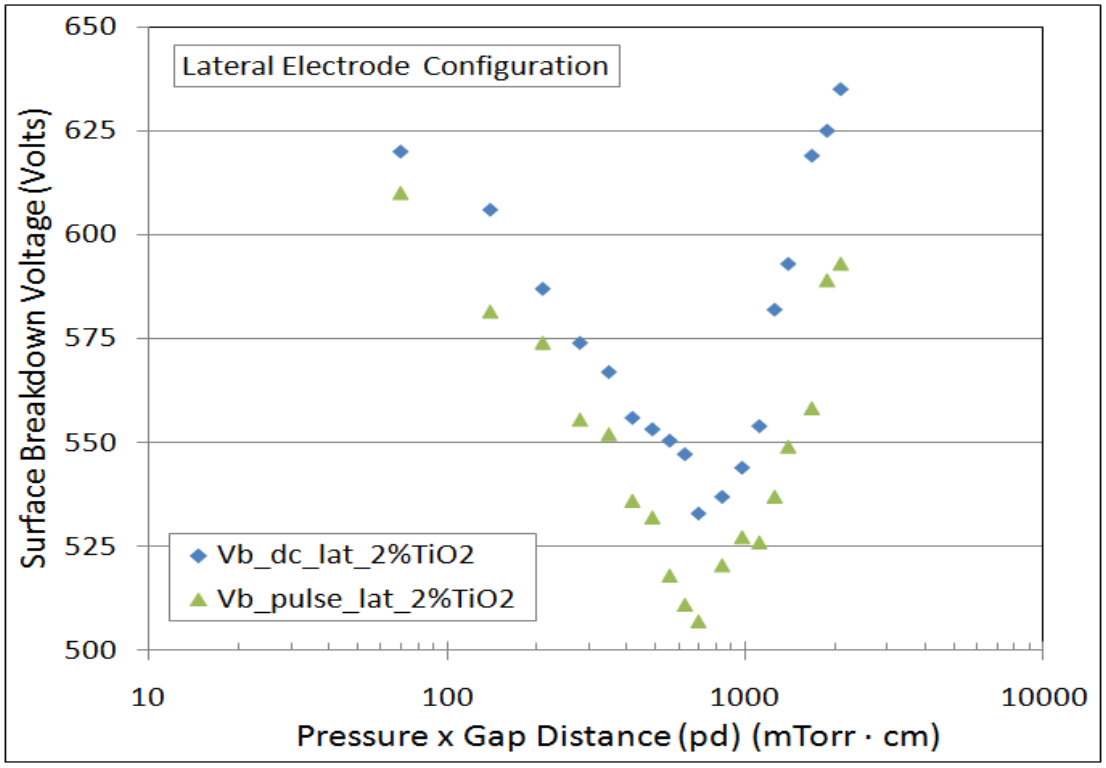

Figure C-4

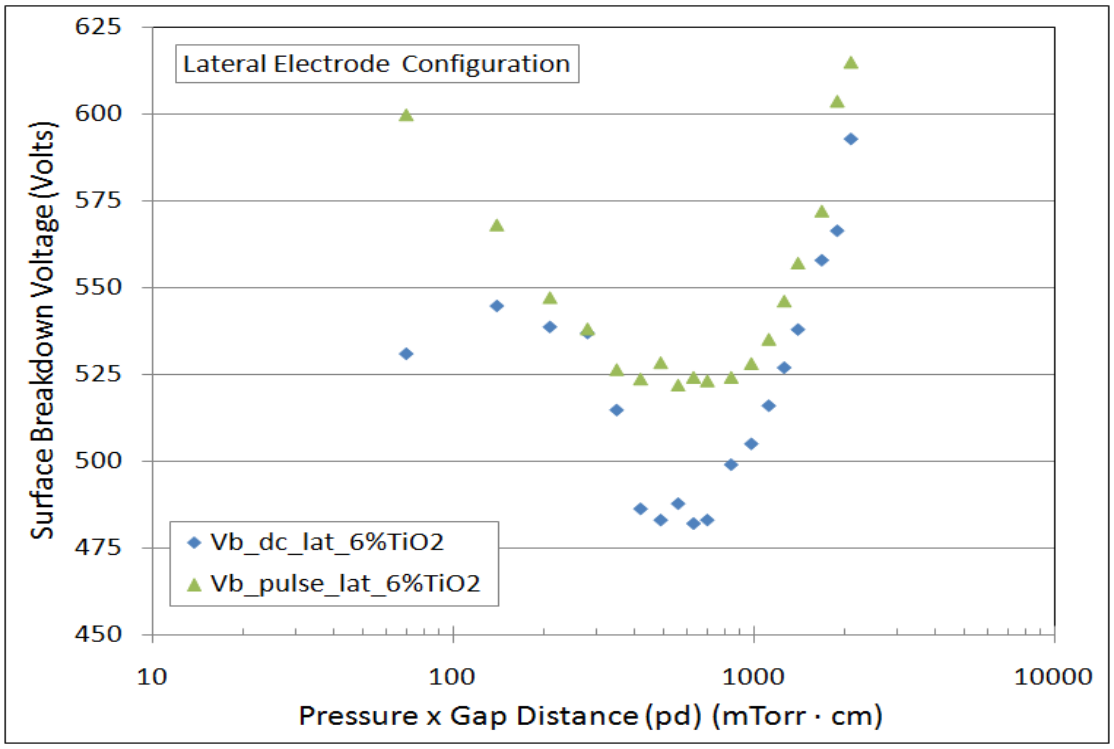
Lateral Electrode Configuration
Surface Breakdown Voltage (Volts)
625
600
575
550
525
500
475
450
Vb_dc_lat_6%TiO2
Vb_pulse_lat_6%TiO2
10
100
1000
10000
Pressure x Gap Distance (pd) (mTorr · cm)

Figure C-5

Appendix D Surface Breakdown Voltages vs. Pressure (Machined Samples)

Complete set of figures for every test set, the surface flashover breakdown voltages are plotted as the function of pressure for the machined surface samples under the lateral configuration. For one test set plot, DC and unipolar pulse signal (20 kHz, 50% duty cycle) breakdown voltages are compared.

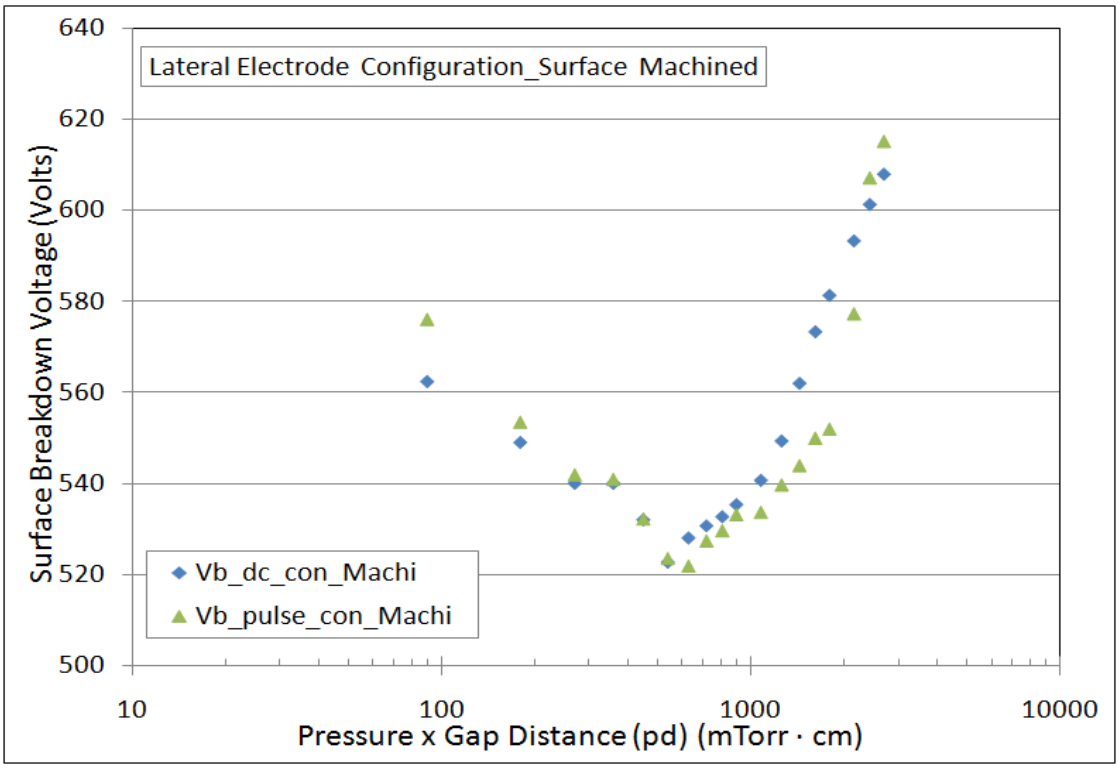

Figure D-1

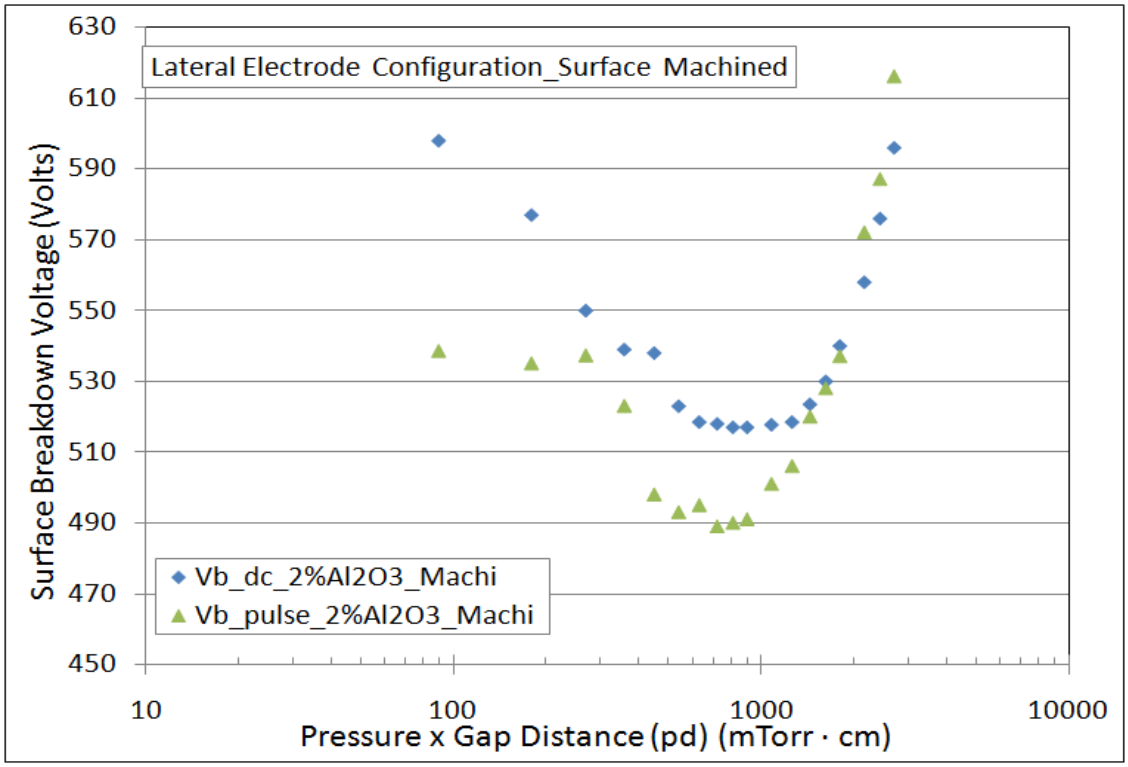

Figure D-2

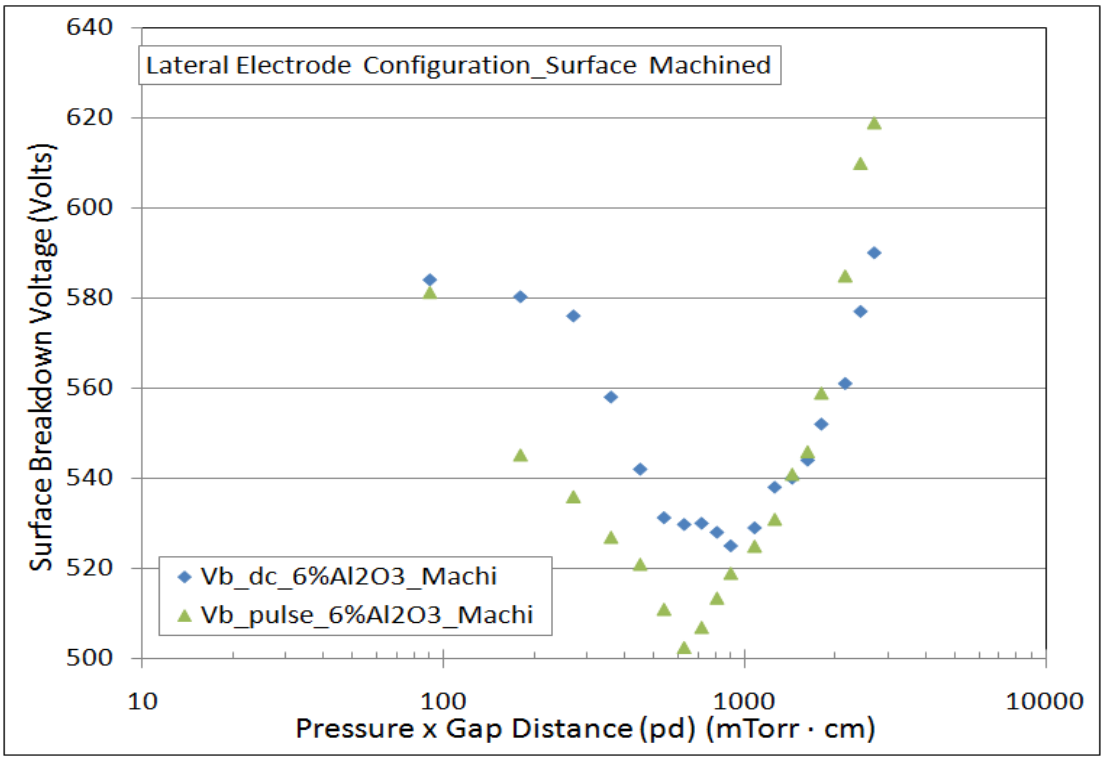

Figure D-3

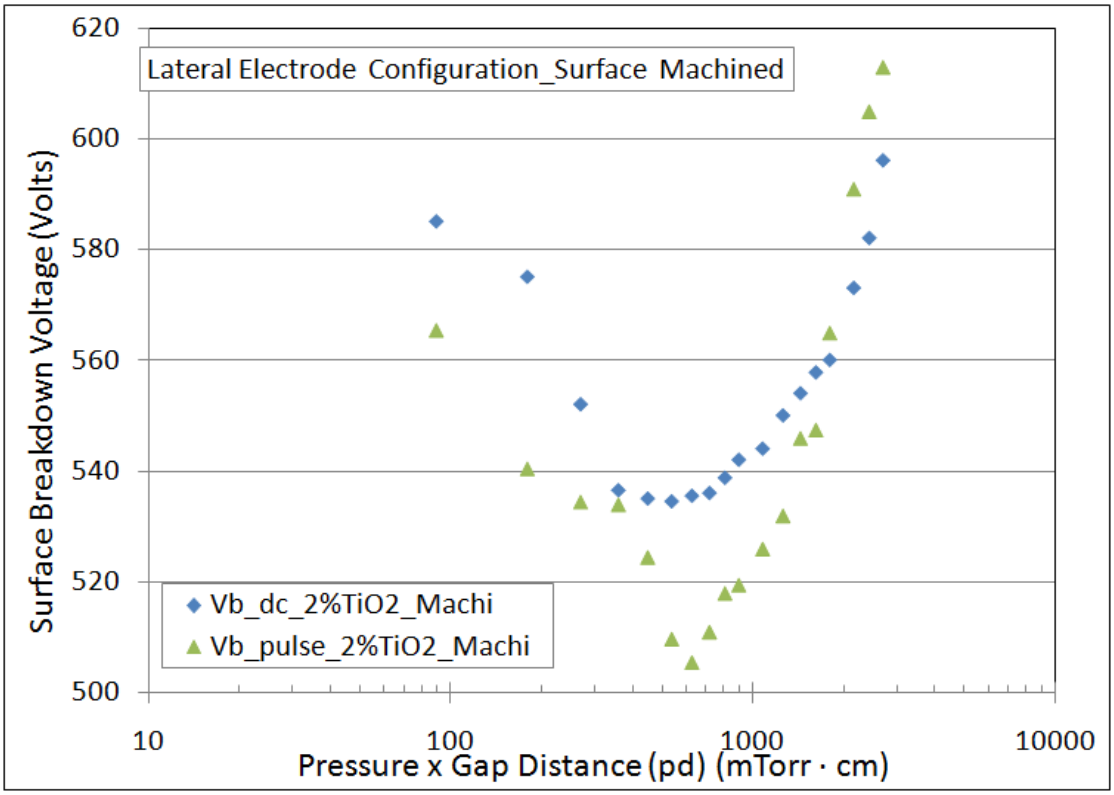

Figure D-4

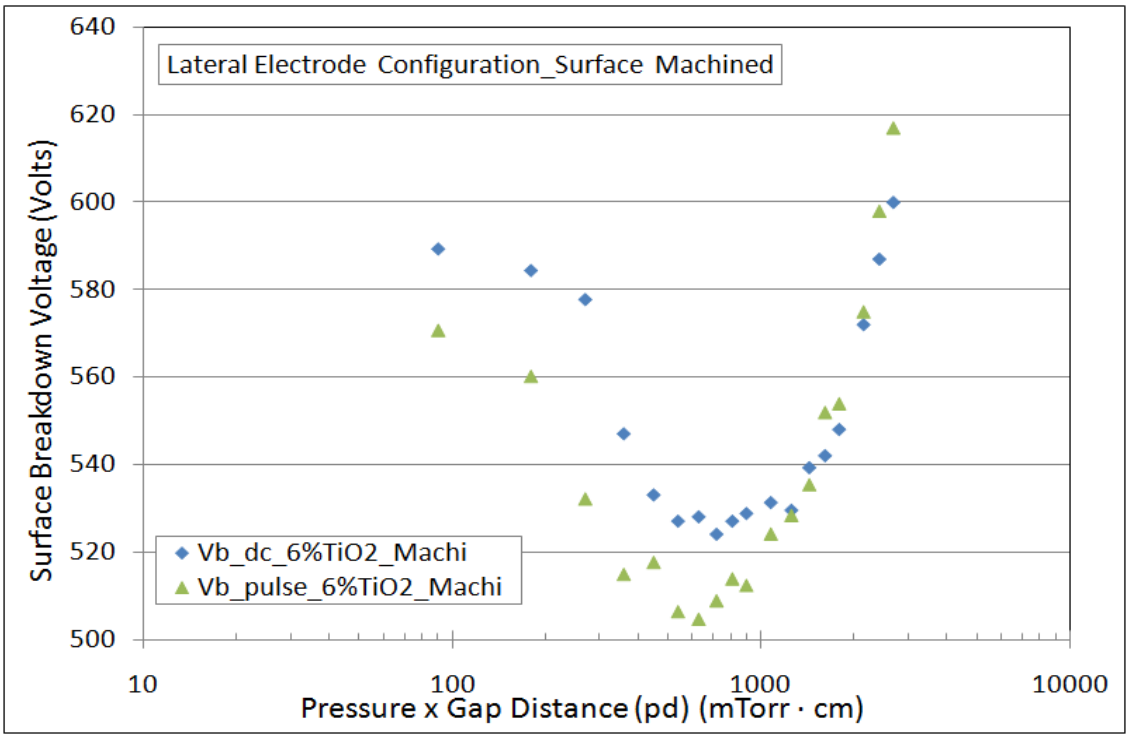
Lateral Electrode Configuration_Surface Machined
Surface Breakdown Voltage (Volts)
640
620
600
580
560
540
520
500
10
100
1000
10000
Pressure x Gap Distance (pd) (mTorr · cm)
Vb_dc_6%TiO2_Machi
Vb_pulse_6%TiO2_Machi

Figure D-5

Appendix E Surface Breakdown Voltages vs. Frequency

Complete set of figures for every test set, the surface flashover breakdown voltages are plotted as the function of frequency under different electrode configurations and surface conditions. In all of the tests, the duty cycle of the unipolar pulse signal is set at 50%. Figure E-1 is the corresponding plot under sandwiched configuration at 300 mTorr. Figure E-2 is the corresponding plot for the untreated surface samples under the lateral configuration at 900 mTorr. Figure E-3 is the corresponding plot for the machined surface samples under the lateral configuration at 800 mTorr.

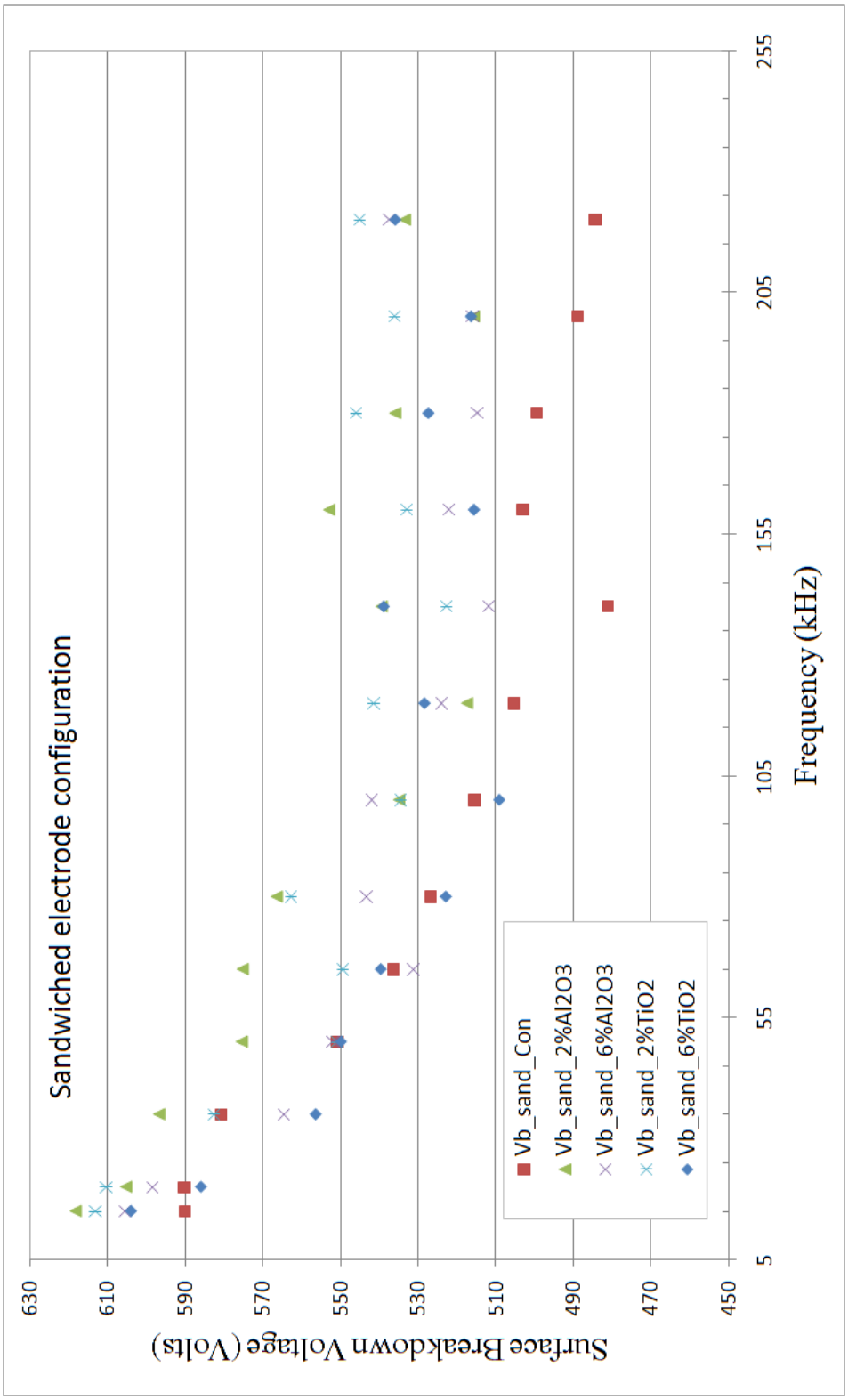
Sandwiched electrode configuration
Surface Breakdown Voltage (Volts)
Frequency (kHz)
630
610
590
570
550
530
510
490
470
450
5
55
105
155
205
255
Vb_sand_Con
Vb_sand_2%Al2O3
Vb_sand_6%Al2O3
Vb_sand_2%TiO2
Vb_sand_6%TiO2

Figure E-1

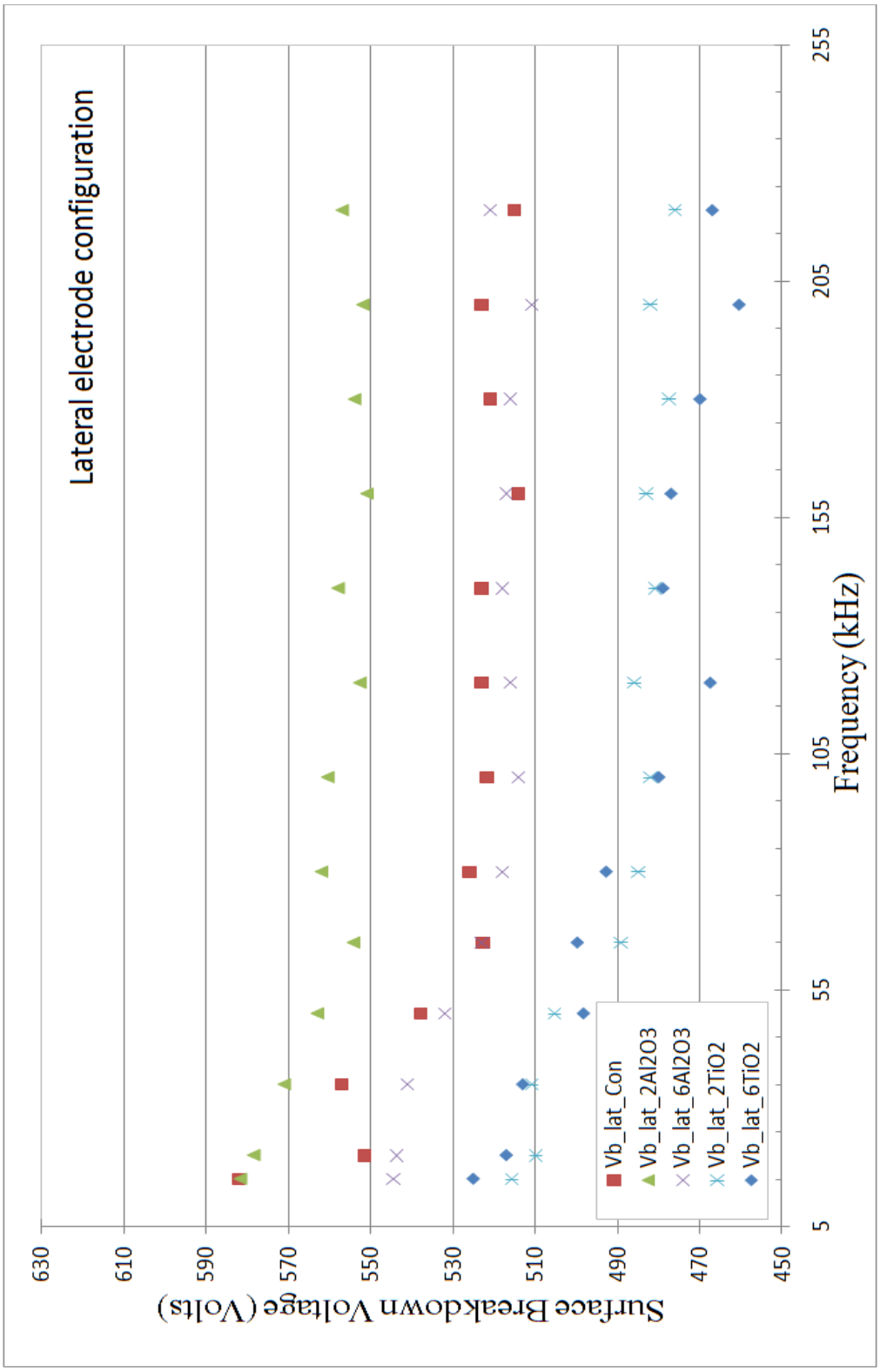
Lateral electrode configuration
Surface Breakdown Voltage (Volts)
630
610
590
570
550
530
510
490
470
450
5
55
105
155
205
255
Frequency (kHz)
Vb_lat_Con
Vb_lat_2Al2O3
Vb_lat_6Al2O3
Vb_lat_2TiO2
Vb_lat_6TiO2

Figure E-2

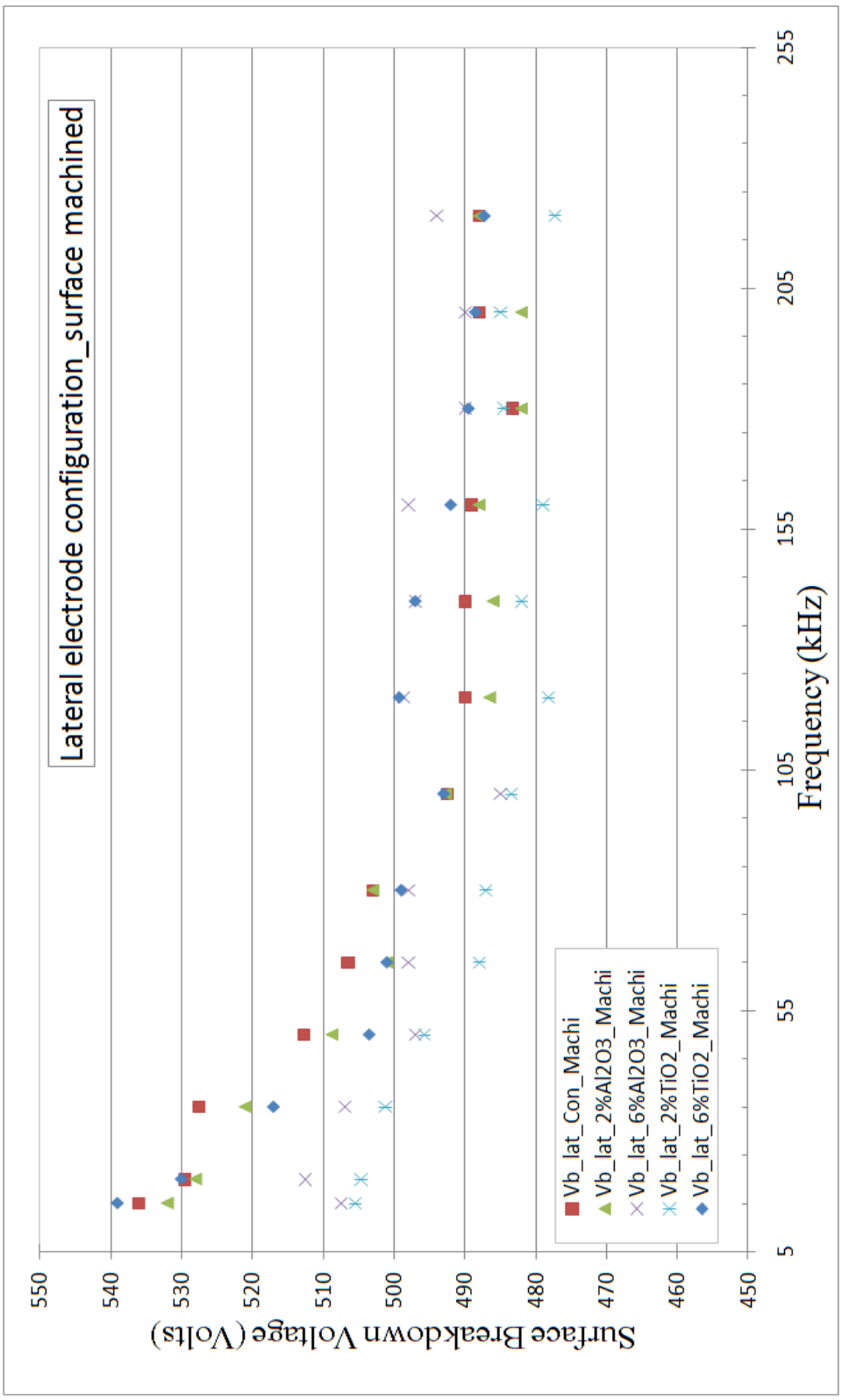
Lateral electrode configuration_surface machined
Surface Breakdown Voltage (Volts)
Frequency (kHz)
550
540
530
520
510
500
490
480
470
460
450
5
55
105
155
205
255
Vb_lat_Con_Machi
Vb_lat_2%Al2O3_Machi
Vb_lat_6%Al2O3_Machi
Vb_lat_2%TiO2_Machi
Vb_lat_6%TiO2_Machi

Figure E-3

Appendix F Surface Breakdown Voltages vs. Duty Cycle

Complete set of figures for every test set, the surface flashover breakdown voltages are plotted as the function of frequency under different electrode configurations and surface conditions. In all of the tests, the frequency of the unipolar pulse signal is 20 kHz. Figure F-1 is the corresponding plot under sandwiched configuration at 300 mTorr. Figure F-2 is the corresponding plot for the untreated surface samples under the lateral configuration at 900 mTorr. Figure F-3 is the corresponding plot for the machined surface samples under the lateral configuration at 800 mTorr.

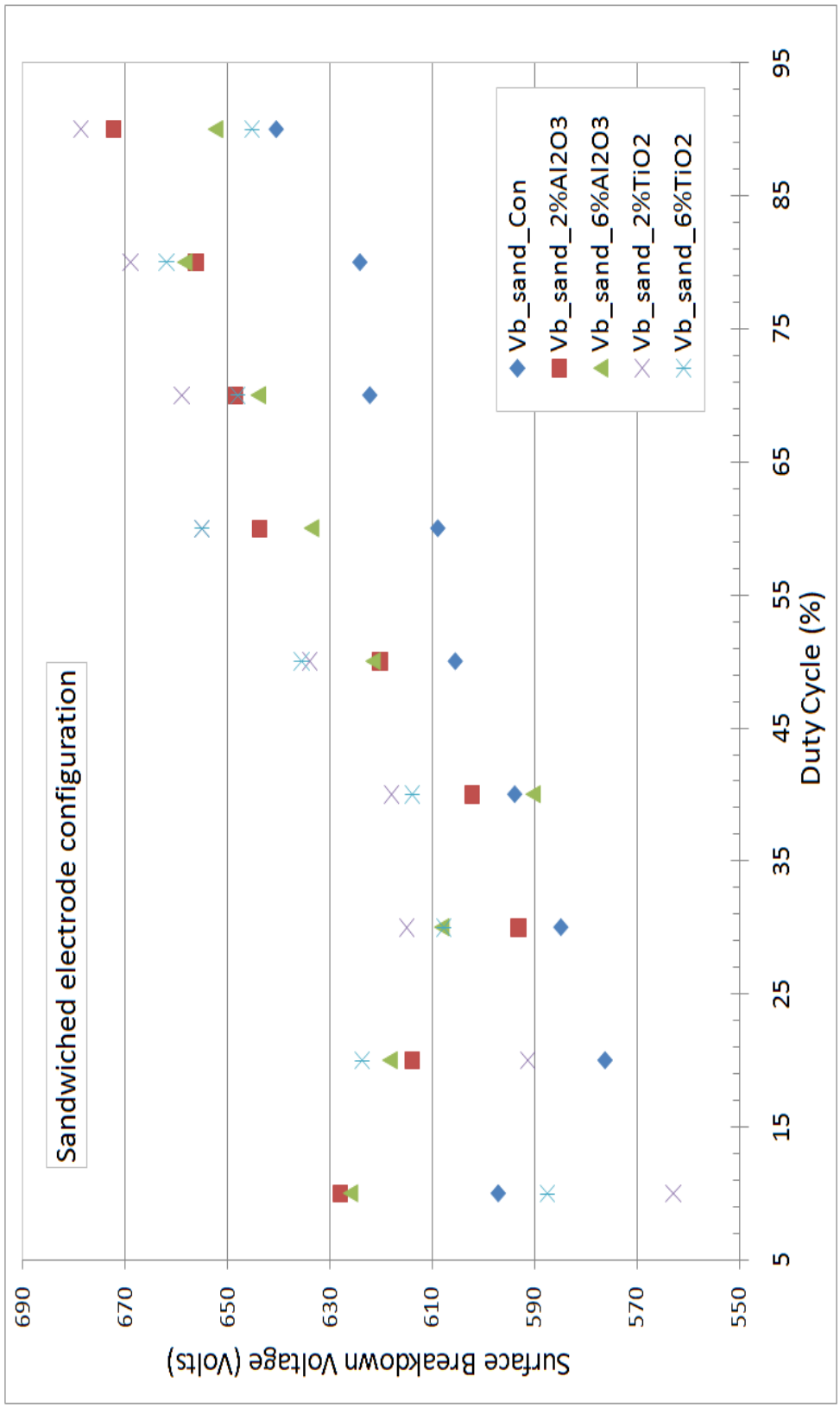
Sandwiched electrode configuration
Vb_sand_Con
Vb_sand_2%Al2O3
Vb_sand_6%Al2O3
Vb_sand_2%TiO2
Vb_sand_6%TiO2
Surface Breakdown Voltage (Volts)
690
670
650
630
610
590
570
550
5
15
25
35
45
55
65
75
85
95
Duty Cycle (%)

Figure F-1

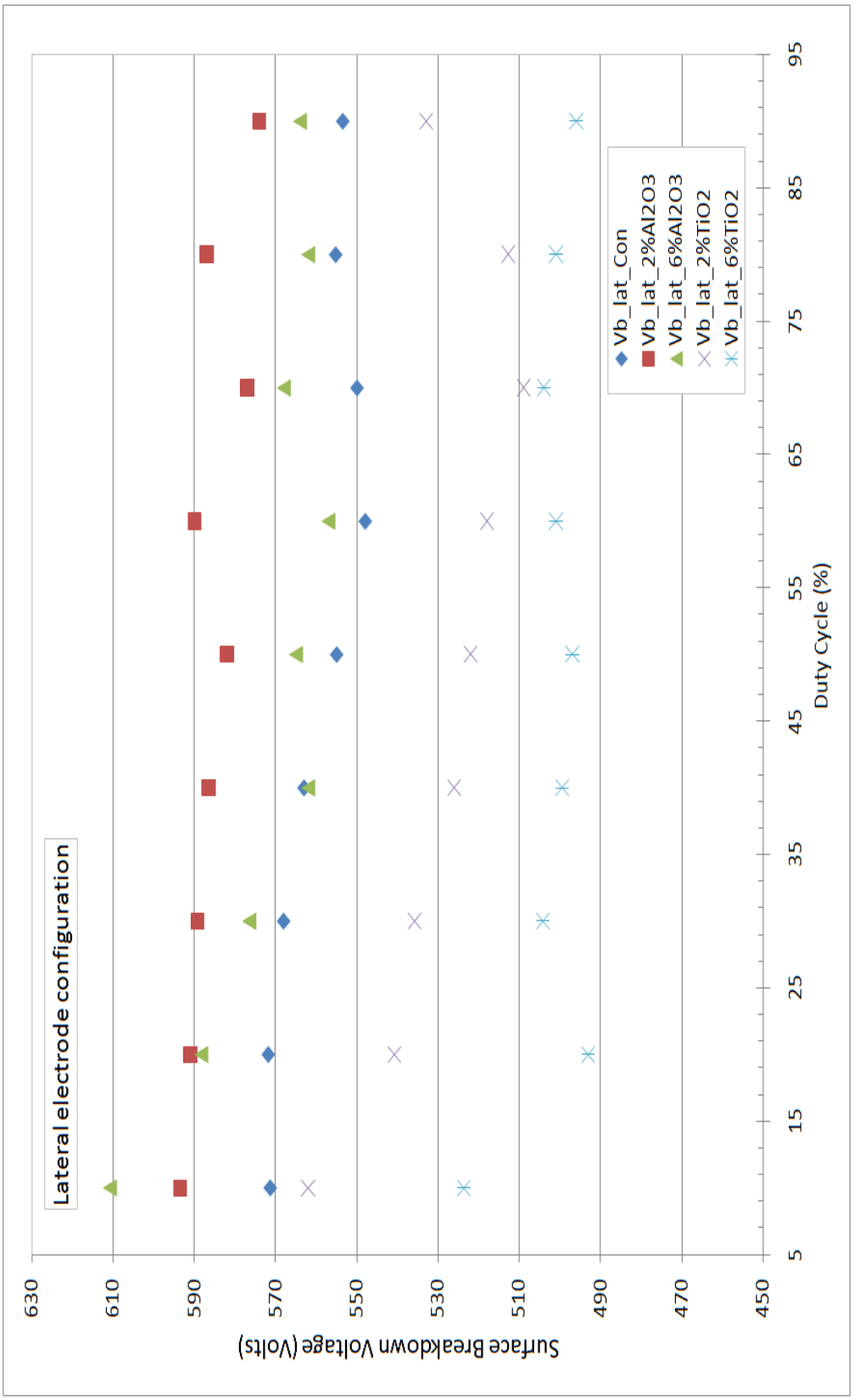
Lateral electrode configuration
Surface Breakdown Voltage (Volts)
630
610
590
570
550
530
510
490
470
450
5
15
25
35
45
55
65
75
85
95
Duty Cycle (%)
Vb_lat_Con
Vb_lat_2%Al2O3
Vb_lat_6%Al2O3
Vb_lat_2%TiO2
Vb_lat_6%TiO2

Figure F-2

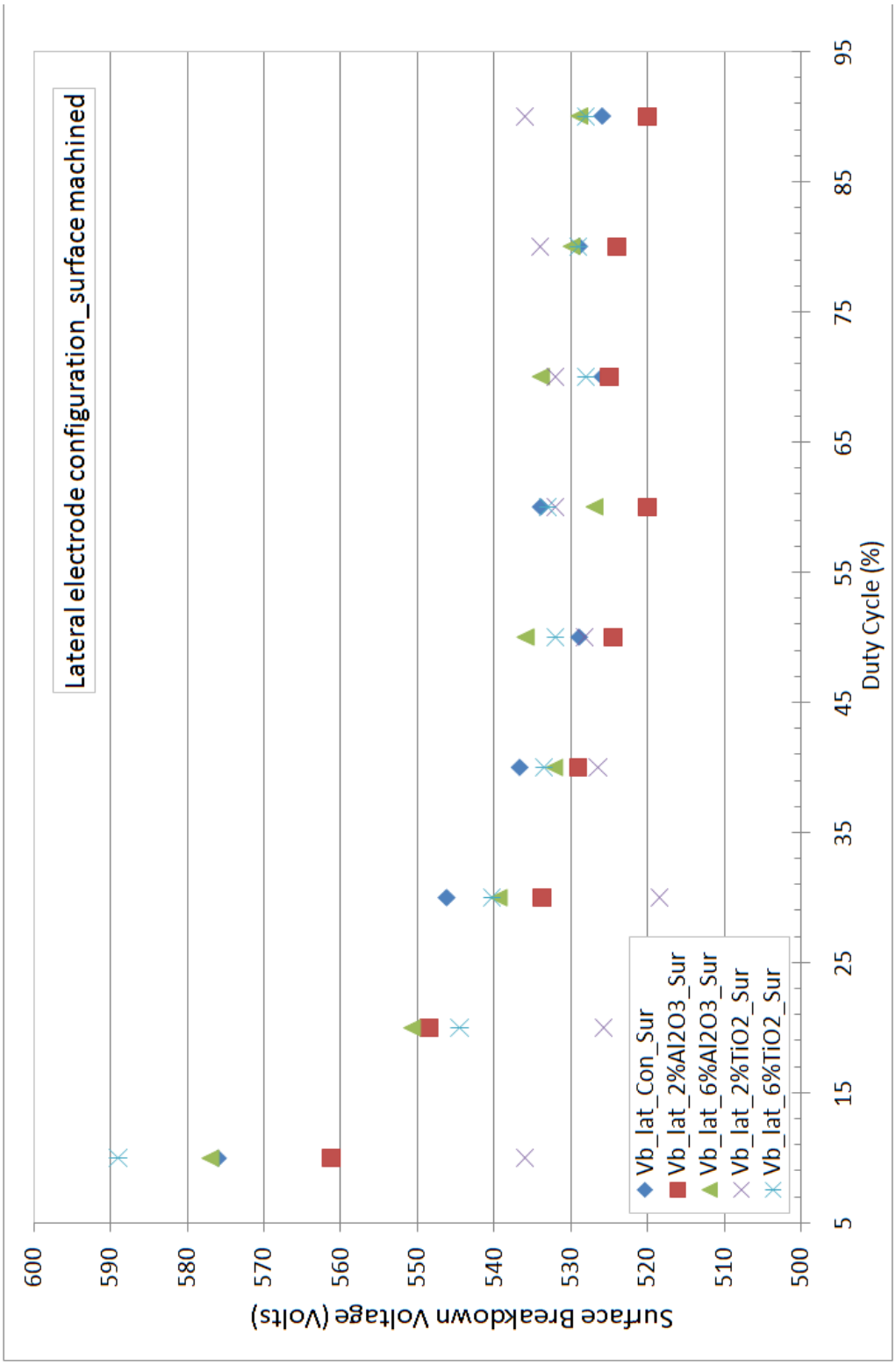
Lateral electrode configuration_surface machined
Surface Breakdown Voltage (Volts)
Duty Cycle (%)
Vb_lat_Con_Sur
Vb_lat_2%Al2O3_Sur
Vb_lat_6%Al2O3_Sur
Vb_lat_2%TiO2_Sur
Vb_lat_6%TiO2_Sur
600
590
580
570
560
550
540
530
520
510
500
5
15
25
35
45
55
65
75
85
95

Figure F-3